High Power Density Permanent Magnet Machines with Hollow Conductors

By: Hetian Chi 180320545

Supervisor: Geraint Jewell

A thesis submitted for the degree of Doctor of Philosophy

The University of Sheffield

Faculty of Engineering

Department of Electronic and Electrical Engineering

August 2025

Abstract

This thesis presents a study into the use of hollow copper conductors with an integral fluid cooling duct to achieve high power density in permanent magnet machines for aerospace. The drivers and challenges for aircraft electrification are discussed and the factors that influence the achievement of high-power density are reviewed. The thesis reviews literature on the use of hollow conductors in electrical machines and identifies that AC losses in the conductors are a major issue that needs to be taken into account.

The thesis presents the findings from two extensive design studies on concentrated and distributed winding machines of various slot-pole combinations and different winding configurations. Extensive use if made of transient finite element analysis to both predict torque capability and copper loss which include the effect of AC losses induced in the hollow copper conductors. These design studies demonstrate the key interaction between stator core geometry and AC losses. These chapter culminate in the selection of a preferred design based on a 30 slot-10 pole design which is then further optimised via a sensitivity study and analysed in terms of irreversible demagnetisation.

The results for a detailed and lengthy experimental investigation into the thermal performance of a commercial grade of hollow conductor are presented. This demonstrates both the ability of coolant flow within a conductor to provide very effective heat transfer but also the problems of dealing with coolant oil viscosity and the resulting pressure drop in very fine ducts.

The thesis concludes by drawing together the key findings and identifying topics for future research.

Acknowledgements

My PhD research was supported by my supervisor, Professor Geraint Jewell. I am thankful for my supervisor and appreciating his continuous encouragement and understanding to me, and the influence of great administrative capacity on me as well, so that making me stronger and stronger.

I would like that my fellow students and research staff in Rolls-Royce UTC office for their support and in particular Dr Stephen Forrest and Dr Jason Ede for their assistance in training me to do the experimental measurements in chapter 5.

Contents

Chapter 1 Introduction

1.1 Electrification of aerospace

Since the 1960s, air traffic has grown at ~9% per annum with many positive benefits in international travel, business and trade. However, since aircraft currently represent 2-2.5% of the man-made carbon dioxide emissions [BOG09, ADU22], there is a growing pressure to reduce carbon emissions from aircraft as otherwise this percentage will continue increase as other sectors such as road vehicles de-carbonise. For several decades, traditional gas-turbine based propulsion systems have undergone continuous improvements in efficiency and reduced emissions and are now moving towards using sustainable aviation fuel (SAF) as a medium term solution. Although these developments have been impressive, there is no clear path to net zero for aircraft. Among the many technological solutions for achieving dramatic reductions in carbon emissions from aircraft, the adoption of electric propulsion has the potential to make the biggest disruptive impact with significant opportunities for eliminating emissions, improvement in overall efficiency and cost effectiveness while meeting reliability requirements [CAO12]. There is also a potential cost savings for airlines, since as shown in Figure 1.1, jet fuel has generally been more expensive than electricity over the last 10 years on $/MJ basis, although in the more recent past the gap has been less pronounced.

Electrical machines can be used in many different ways for future aircraft propulsion as shown in Figure 1.2 [BOW18]. This shows different hybrid-electric, turbo-electric propulsion architectures, all of which include electrical machines as the propulsion machine and/or as a generator. The electrical elements of a hybrid or all-electric propulsion system comprises power electronics, electrical machines, many sensors and control systems. There are many factors which contribute to the competitiveness of this kind of system [KRI91] including reliability; weight; power density; efficiency; control features and complexity; complexity of design and fabrication; thermal robustness; volume and cost. High-power density permanent magnet (PM) machines could emerge as a vital component in these advanced propulsion architectures. The combination of high torque density and high efficiencies makes them well-suited to future aircraft. It is important to note that as shown in Figure 1.2, there are many other sub-systems in an aircraft propulsion system and each of these have challenges of weight, efficiency and reliability.

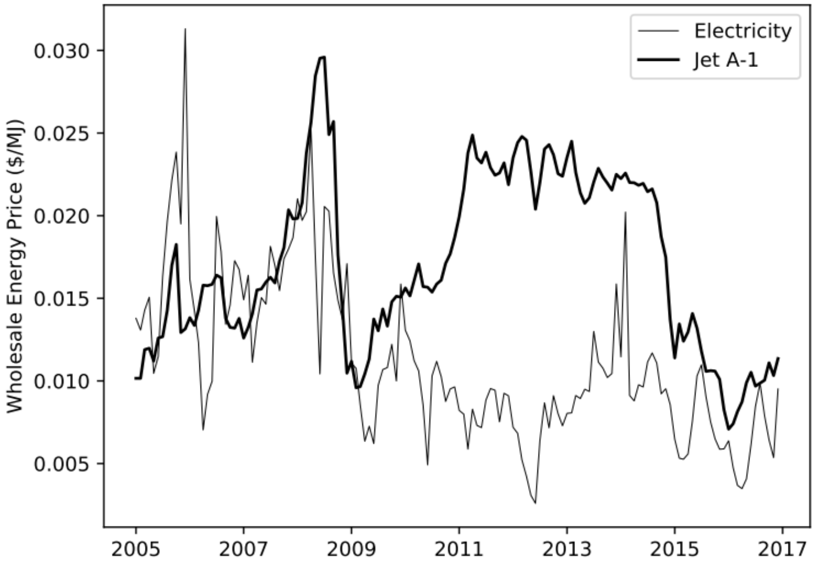

Figure 1.1 Normalized energy cost of Northwest U.S. wholesale electricity versus U.S. Jet A-1 (based on data from the U.S. Energy Information Administration [USE17a, USE17b]

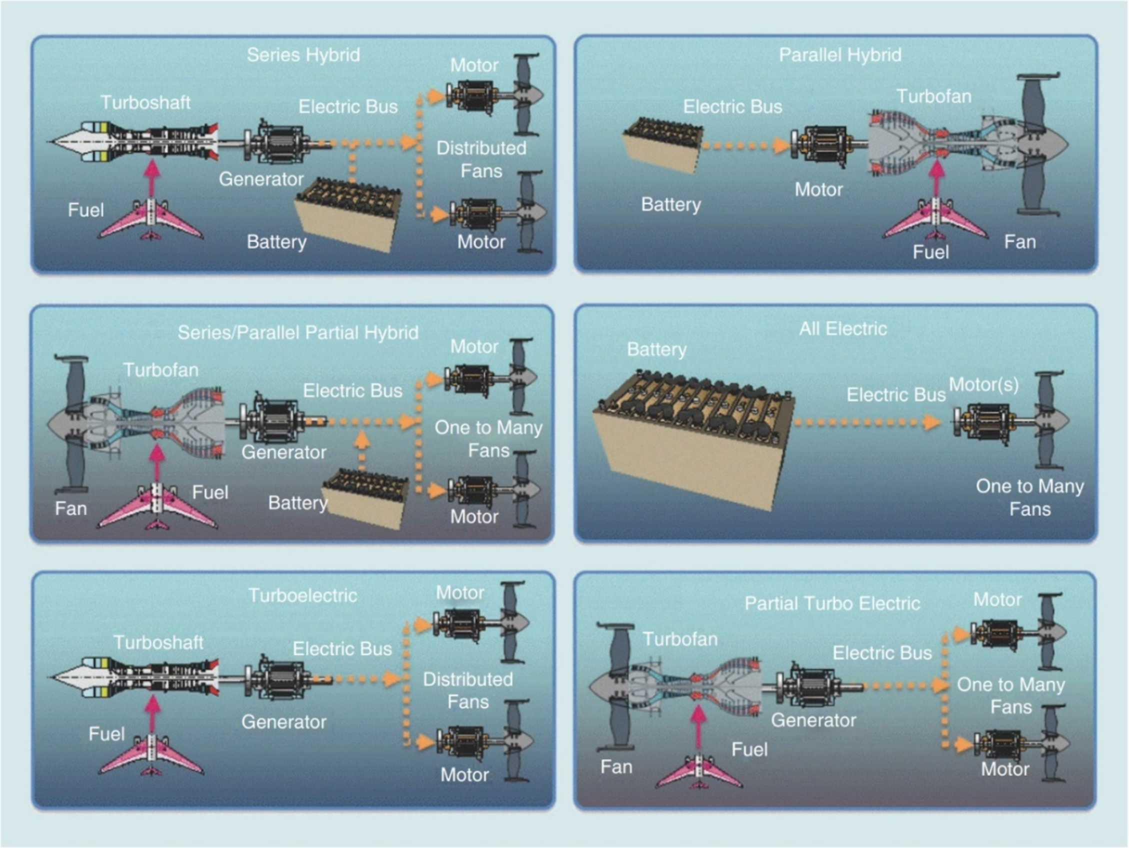

Figure 1.2 Range of different hybrid-electric, turbo-electric and all electric propulsion architectures (Source: [BOW18])

There are numerous aircraft level studies on the feasibility of all-electrical aircraft [REF13a] covering a range of aircraft sizes. Figure 1.3 shows the ratings of individual electric machines projected for future all-electric aircraft. Many of the future aircraft and propulsion concepts involve distributed propulsion in which many electrically driven fans are distributed over the airframe and provided with electrical power via a single or a pair of generators of much higher rating. As can be seen from Figure 1.3, aircraft up to 50 seaters or so have requirements for machines with ratings in the 100s of kW range even though the overall propulsion requirement may be into the MW. Hence, there is a great deal of interest in electrical machines with ratings in the 200-500kW range for driving distributed fans. These fans would typically operate at speed of 2000-6000rpm and direct-drive is often preferred over geared systems.

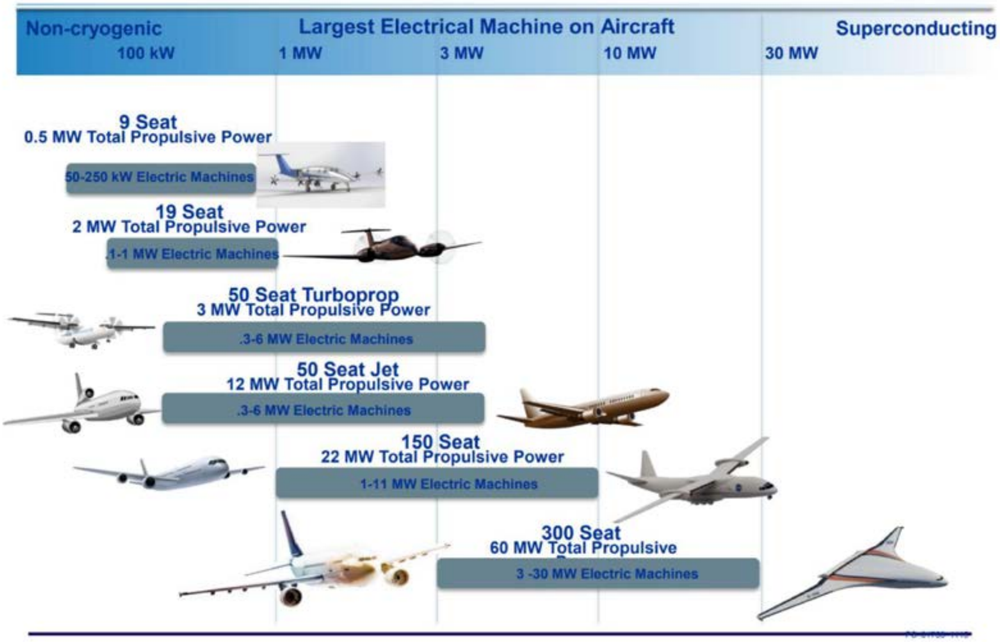

Figure 1.3 Projected power ratings of electrical machines for future all-electric aircraft [BOW16]

In aerospace, every kg of mass on board an aircraft has direct impact on fuel burn, range, and payload. Hence, power-density is a critical feature for any electrical machine type and design particularly as the power ratings of machines increase. The key power density metric is usually power to mass ratio in kW/kg. Road-mapping by the Aerospace Technology Institute [REF13b] has identified targets for improvements in power density in electric machines as shown in Figure 1.3 for a fuel-cell powered aircraft. This anticipates an increase from 13kW/kg in 2026 (noting that this roadmap was published in 2020) to 25kW/kg in 2025. This suggests that a doubling of power density is required between 2026 and 2050 although this is the lowest percentage increase of all the components listed in Figure 1.3. It is interesting that the overall power density of the propulsion system by 2050 is only 3.0-3.5kW/kg, which shows that improving power density of the electrical machine is only one of many technology challenges that must be addressed.

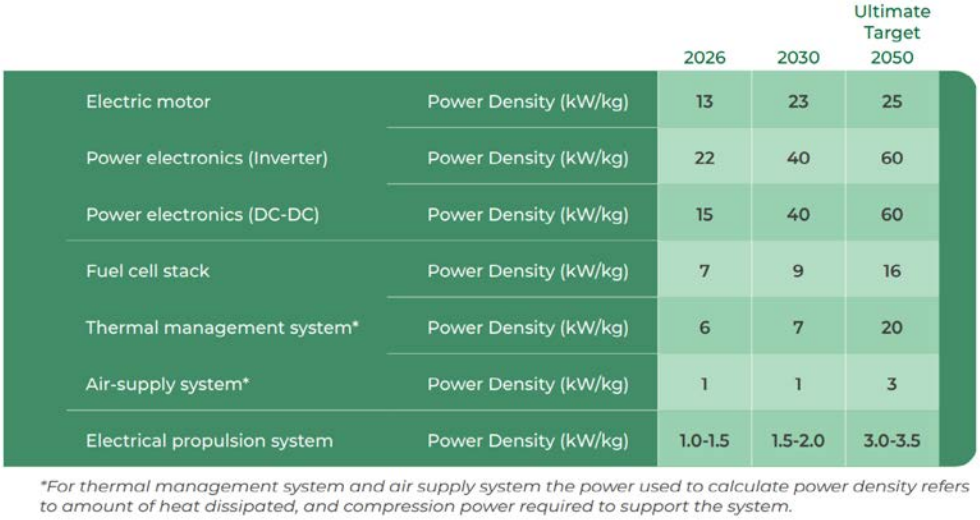

		2026	2030	Ultimate Target 2050
Electric motor	Power Density (kW/kg)	13	23	25
Power electronics (Inverter)	Power Density (kW/kg)	22	40	60
Power electronics (DC-DC)	Power Density (kW/kg)	15	40	60
Fuel cell stack	Power Density (kW/kg)	7	9	16
Thermal management system*	Power Density (kW/kg)	6	7	20
Air-supply system*	Power Density (kW/kg)	1	1	3
Electrical propulsion system	Power Density (kW/kg)	1.0-1.5	1.5-2.0	3.0-3.5

**For thermal management system and air supply system the power used to calculate power density refers to amount of heat dissipated, and compression power required to support the system.*

Figure 1.4 - Future target power densities of components of an all-electric aircraft (Source: Aerospace Technology Institute)

Another long-term technology roadmap for electrical machines in aerospace is that published by NASA for MW rated machines. This roadmap suggests a need to achieve ~20kW/kg by 2035 for non superconducting machines, as shown in Figure 1.5.

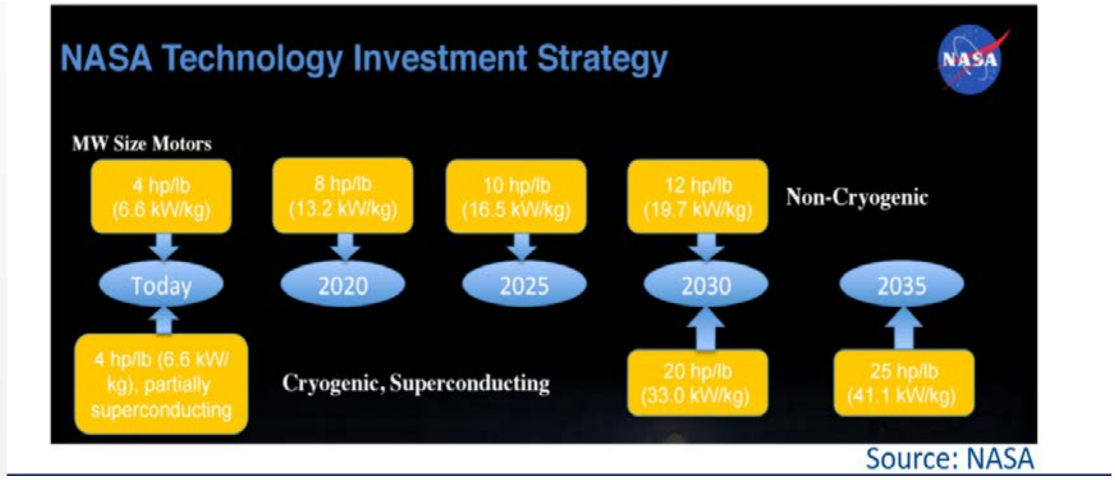

NASA Technology Investment Strategy

MW Size Motors

4 hp/lb (6.6 kW/kg) → Today

8 hp/lb (13.2 kW/kg) → 2020

10 hp/lb (16.5 kW/kg) → 2025

12 hp/lb (19.7 kW/kg) → 2030

Non-Cryogenic

Cryogenic, Superconducting

4 hp/lb (6.6 kW/kg), partially superconducting → Today

20 hp/lb (33.0 kW/kg) → 2030

25 hp/lb (41.1 kW/kg) → 2035

Source: NASA

Figure 1.5 Technology Investment Strategy on MW Size Motors (Source: NASA)

The values in the NASA roadmap differ slightly from those published by the ATI in Figure 1.4 which may in part be due to MW ratings considered. However, in both cases the roadmaps show the significant progress that must be made in reliable power density in the coming years to make all-electric aircraft a viable technology. As noted for the ATI roadmap, the improvements in electrical machine power density will need to be matched by the other technologies in the propulsion system.

1.2 High power density permanent magnet machines

As noted previously, the very challenging targets for electrical aircraft propulsion make high power density permanent magnet machines a strong competitor. For almost all electrical machine applications below a few MW, permanent magnet machines are usually regarded as the highest performing machine type.

There have been several published reviews and surveys of high-power density electrical machines [MOG14, ZHA16, CAO12,] which have collated published performance details from literature and manufacturer product information across a wide range of power ratings and application areas. As an example, Figure 1.6 shows a published plot drawn from a survey of power density in several different types of electrical machines up to 300kW, in which covers radial flux permanent-magnet machines (RFPM), axial flux permanent-magnet machines (AFPM), induction machines (IM), switched reluctance machines (SRM), wound-field synchronous machines (WFSM) and also superconducting machines (SCM) [ZHA16]. As can be seen from Figure 1.6, the highest power density from this survey was approximately 8.3kW/kg for a radial flux permanent-magnet machine (RFPM).

Figure 1.7 shows another plot drawn from the same survey but for machines in the MW power range which again covers a range of different machine types [ZHA16]. In this case, the maximum power density is ~9.5kW/kg achieved with a wound-field synchronous machine (WFSM). In general, it is would be expected that power density increases with machine size.

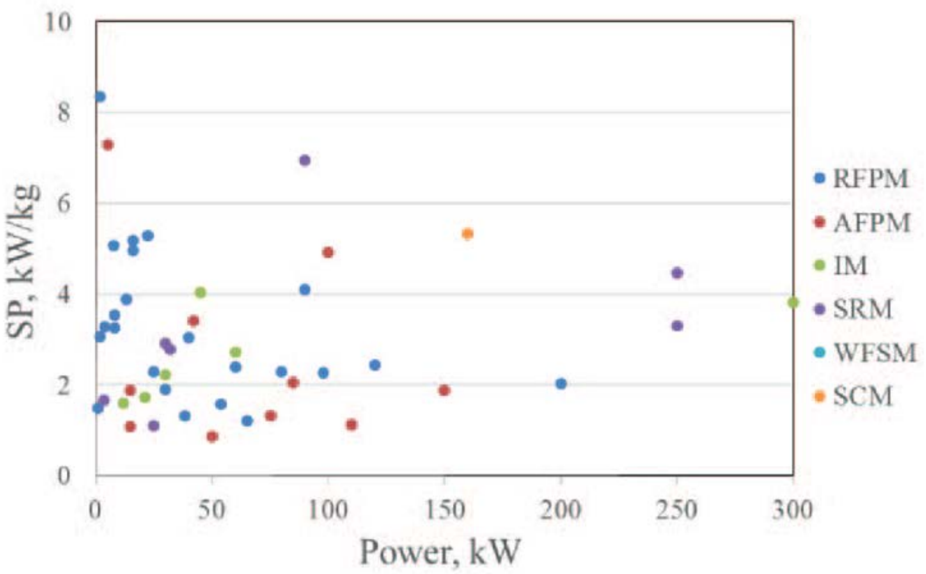

Figure 1.6 Published survey of power density in a range of different machine types up to 300kW [ZHA16]

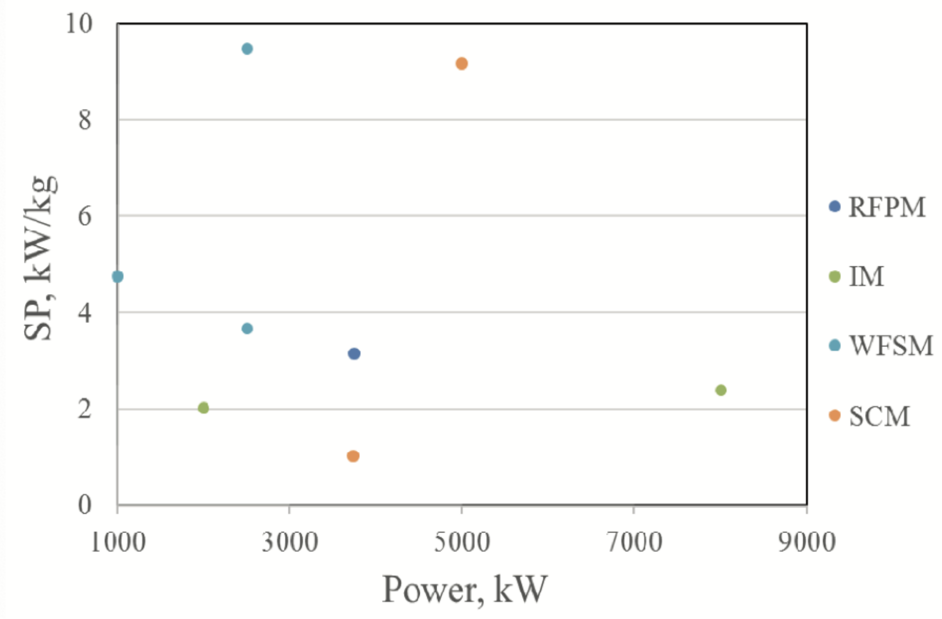

Figure 1.7: Published survey of power density in a range of different machine types - MW Rating range (Source: [ZHA16])

Surveys of power density are useful to provide some general guidance but there are several problems in relying on published power densities. There is often inconsistency in the machine components which are included in the mass for the calculation of power density, e.g. some papers focus on active mass only and others provide detailed breakdowns of the mass including all the structural mass [BAL19]. There is no consistency between the operating conditions at which power densities are quoted, e.g. peak, continuous etc. There is an IEC standard (IEC 60034-1) [IEC19] for specifying operating duty cycles, but many published research papers and manufacturer data sheets do not reference these standards. It is also important to note that machines are generally sized on the basis of torque and not power and hence comparing power densities for machines with very different operating speeds is often not a useful means of comparing the effectiveness of their electromagnetic design.

An example of high-performance machine for specialist automotive application is shown in Figure 1.8. This is a high-power density permanent magnet machine manufactured by Equipmake. This has a maximum speed of 10,000rpm and a base-speed of ~4500rpm depending on the voltage supply. The power versus speed curve shows the short-term power rating is ~250kW at 4,500rpm on the higher 750V supply but the continuous rating with water cooling is 130kW. The mass of this machine including the casing is 42kg which gives a peak power density of 5.95kW/kg and a continuous power density of 3.09kW/kg.

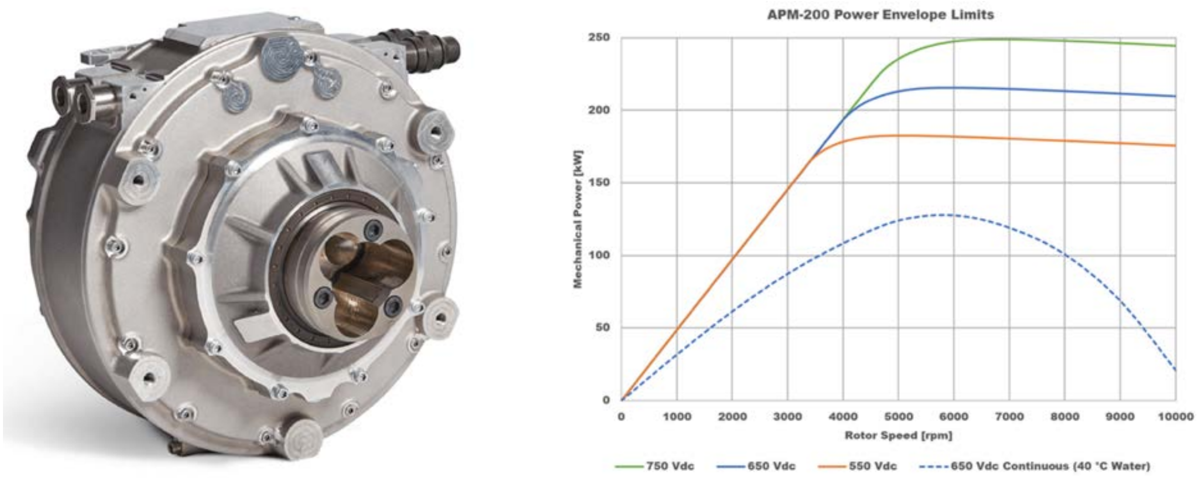

Figure 1.8 Equipmake APM-200 high speed permanent magnet machine (Source: Equipmake)

Whereas electrical machines from the automotive sector, particularly small volume manufactured machines for high performance vehicles provide some useful benchmarks, for aerospace airworthiness regulations require that very rigorous standards are met on mechanical and electrical integrity, electromagnetic compatibility, thermal robustness, flame tests, fail-safe functionality etc.

Ensuring compliance of machines with these numerous standards often involves some compromise in terms of mass and the materials that can be used compared to other sectors and hence some of the technologies and ratings of automotive machines cannot be directly compared on a like-for-like basis.

There are some published studies on demonstrator machines for aerospace applications which provide some indication of power density capability though these have not necessarily been designed to the full aerospace standards. One example for which there is extensive mass data is presented is a high-speed starter-generator for aerospace applications [BAL19]. This oil-cooled machine had a total mass, including all the casing, of 22.75kg and produced a continuous power of 100kW at 14,677rpm with a 150kW short-term rating, giving continuous power density of 4.4kW/kg and a peak power density of 6.6kW/kg.

Siemens developed a liquid cooled permanent magnet machine for propulsion of light aircraft and achieved an impressive 5kW/kg at a low speed of 2700rpm [SIE16]. Another example of machines for aerospace include the Evolito 1x3 D250 axial field machine which has a continuous power rating of 207kW and a peak power rating of 230kW (30s) both at 9,500rpm. This has a mass of 13kg giving a continuous power density 15.9kW/kg and a peak power density of 17.7kW/kg.

A much lower speed machine for primary aerospace propulsion has been proposed by H3X. Their HPDM-350 machine which is still under development and only has preliminary data sheet is a 50kg machine with a continuous power rating of 350kW giving a continuous power density of 7kW/kg. This is a low speed machine with peak power at 2700rpm and is therefore well-suited to direct-drive. Its torque density of 24.8 Nm/kg is impressive.

The design of electrical machines, for both motoring and generation application, requires a careful balance between trade-offs, e.g. efficiency versus power density [GOL19]. Achieving the highest levels of performance in terms of high torque / power density requires consideration of electromagnetics, thermal management, materials engineering and mechanical design.

Several different machine topologies have been proposed for high power density with the main categories being radial flux machines with cylindrical rotors and axial flux machines with disk type rotors. Exploded views of these two machine topologies are shown in Figure 1.9. Radial field machines tend to be able to achieve the highest power density, in part because they are able to operate at much higher speeds than most axial field machines. The nature of the scaling of torque with diameter tends to favour axial field machine in high torque, low-speed applications particularly if multiple units are stacked up.

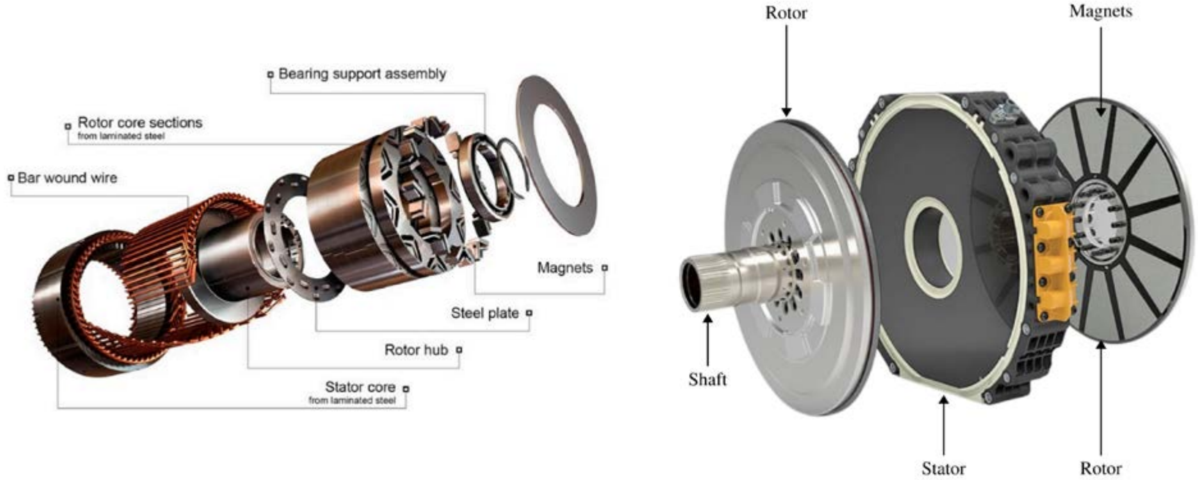

Radial field IPM machine (Source: [PAT24]) Axial field machine (Source: [DEE23])

Figure 1.9 Radial and axial field permanent magnet machines

1.3 Summary

The chapter has introduced the drivers and challenges for electrification of aerospace propulsion and reviewed developments in high-performance permanent magnet machines. It has established ~20 kW/kg power density is a reasonable and challenging target for the research reported in this thesis.

1.4 Thesis Structure

This thesis is structured into 6 chapters as follows:

Chapter 1 discusses the background on the applications and some of the technical challenges of high power density machines and reviews some literature on the state-of-the-art in high power density machines.

Chapter 2 reviews the technical aspects of achieving high power density in electrical machines with a particular focus on thermal management, including hollow conductors and AC losses.

Chapter 3 presents a design study on a series of concentrated winding machines and establishes their performance in terms of torque density and losses and demonstrates the significant effect of AC losses induced in hollow conductors.

Chapter 4 presents a further design study on distributed winding machines, again exploring in depth the effect of AC losses and factors that impact on power density such as the influence of pole number.

Chapter 5 reports on an experimental programme concerned with measuring the thermal performance of a hollow conductor.

Chapter 6 provides some conclusions on the work, identifies some key novelties in the research and makes suggestions for future research.

Chapter 2 - A review of losses thermal management in high power density machines

2.1 Introduction

As discussed in chapter 1, this thesis is focused on the design and analysis of high power density permanent magnet machines and in particular the use of hollow conductors as a method for removing losses from the stator windings. Permanent magnet machines operating as motors can operate for short periods (say a few 10s of seconds or minutes) at several times their continuous rating providing the power converter can supply the current and the magnet is not irreversibly demagnetised. During this period, the heat capacity of the winding can be used to balance the mismatch between the losses generated and the heat extracted by the cooling mechanism. However, for steady-state operation the heat generated and the heat removed by cooling must balance and so the capability of the cooling system sets the limit on the losses and in turn the maximum continuous power capability of machine. This chapter reviews some of the key aspect of thermal management with a focus on copper loss and some of the loss mechanisms that must be managed.

2.2 Thermal management and modelling of electrical machines

The torque produced by an electrical machine with a rotor of diameter D and axial length L can be estimated using:

$$T = \frac{\pi}{2} D^2 LBQ \qquad 2.1$$

The two factors which determine the rotor volume and so the machine size required to produce the rated torque are the magnetic loading (B) and the electric loading (Q). The magnetic loading is the average airgap flux density. In permanent magnet machines it is usually limited to 0.8-1.0T depending on the rotor geometry, permanent magnet grade and the magnet temperature. The electric loading is not constrained to any particular fundamental maximum but is normally limited by thermal factors such as the maximum operating temperature of the winding insulation. There may also be cases where irreversible demagnetisation of the rotor magnets is a limit. There may also be a need to consider efficiency and limit the electric loading to a level below the thermal limit to achieve an acceptable system efficiency. Removing copper loss from the winding is almost always the limiting factor on power density in machines, except for very large multi-MW machines when iron loss can become the critical factor. In some small specialist high-speed machines the iron loss can be similar or even greater than the copper loss in high speed machines [DIN12]. The iron loss also tends to be easier to extract from the machine as the stator core is usually in good thermal contact with the casing and the coolant

In most machines, copper loss generated in the conductor usually passes through a series of layers of materials with low thermal conductivity, such as the conductor insulation, winding varnish or encapsulant and slot linear, before reaching the casing and/or the coolant. This means that in almost all machines, the worst-case hot-spot is the centre of the coil in each slot. As an example, Figure 2.1 shows the predicted temperature distribution in a coil in which a significant proportion of the slot is occupied by low thermal conductivity materials [VEG21]. In the example shown, there is a ~45°C temperature difference between the center of the coil and the stator core. The wider thermal behaviour of this machine was not discussed in [VEG21] as it was focused on modelling of heat transfer within the slot, but it does illustrate that heat transfer across a slot is a major pinch-point in the thermal performance of electrical machines.

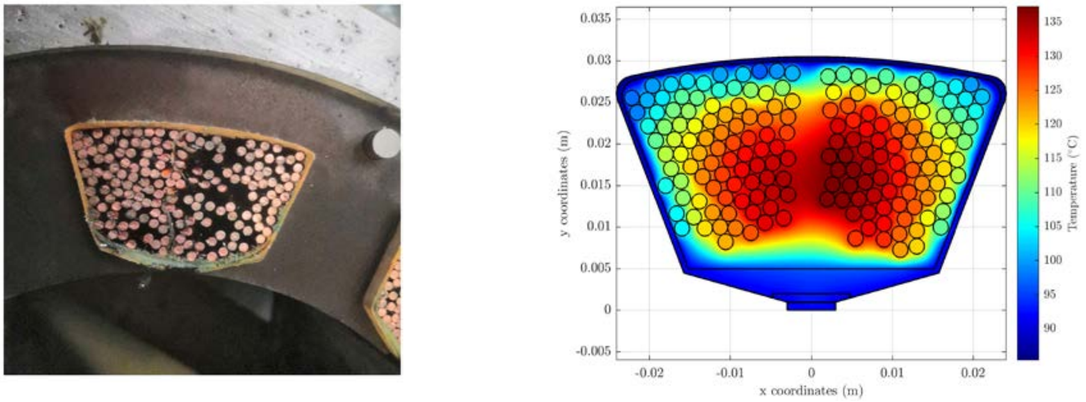

(a) Slot cross-section

(b) Example of predicted hot-spot in coil

Figure 2.1 Typical conductor layout and temperature distribution in a slot of a low to medium performance permanent magnet machine (Source: [VEG21])

Bar conductors of the type shown in Figure 2.2 can be used to improve the heat transfer across the slot as the heat can flow through copper towards the slot edge of the slot and only pass though one conductor. This type of winding is being used increasingly electrical machines with the adoption of hairpin coil technology in electrical vehicles [ZHA19].

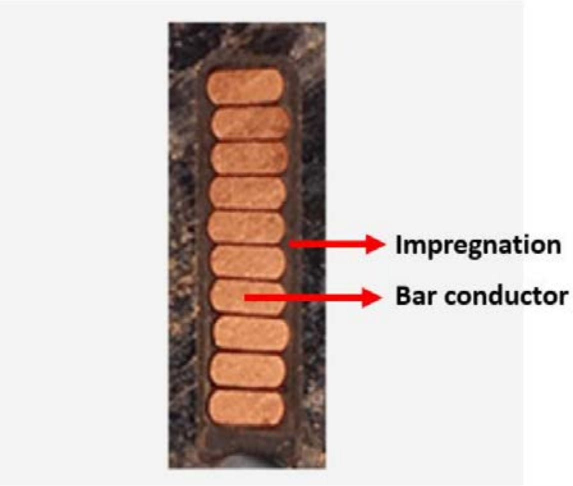

Figure 2.2 Bar wound machine winding from a Mitsubishi Generation 8 traction motor (Source: Mitsubishi)

The benefit of solid bar conductors over stranded wire was shown in [SUN24] in which a simplified single slot was modelled with thermal finite element analysis for both solid bars and stranded wire. The resulting temperature distribution (note the scale is in degrees Kelvin) for the same power dissipation is shown in Figure 2.3. As will be apparent not only is the temperature lower in the bar winding but there is also much less of a temperature gradient within the slot.

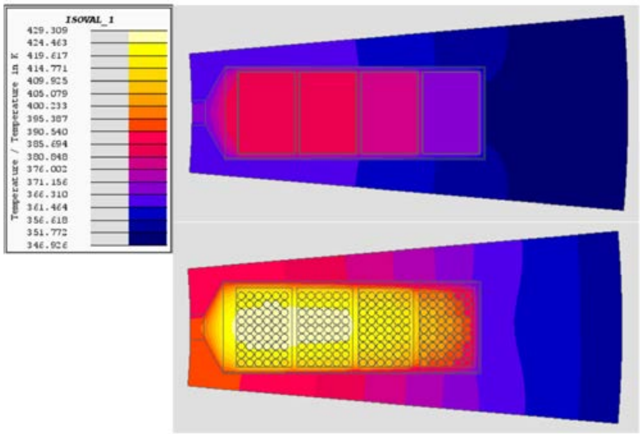

Figure 2.3 Finite element predicted temperature distribution in a single slot (Source: [SUN24])

Indirect cooling of the electrical machines using a water-cooling jacket is widely used in many permanent magnet machines, particularly in electric vehicle traction machines. These rely on thermal conduction from the winding to the casing to allow an increased operating current density, thereby increasing the torque and power density. However, the heat produced in the conductors has to pass through stator internal parts which includes conductors, slot insulation, any interface air gap within slots, the stator core and the interface to the cooling jacket. Hence, the current densities which can be achieved with water-jacket or oil-jacket cooling are often limited [CHE20, NAK90, CAM16, LIN17, LIN16, WAN07, WEN06]. An alternative indirect cooling method which brings the coolant in closer proximity to the conductors is to locate a cooling pipe in the end-windings [MAD19] as shown in Figure 2.4. Although this method can improve heat transfer, the selection of pipe material and wall thickness is important in terms of minimising the induced electromagnetic loss in the pipe [MAD19].

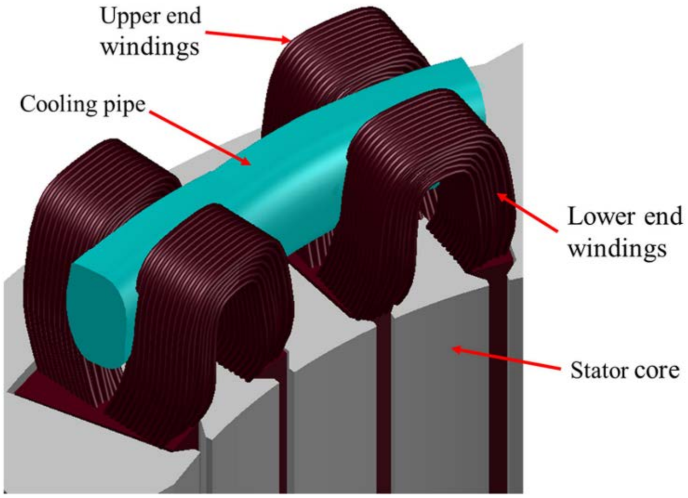

Figure 2.4: Split end-windings with cooling pipe passing through (Source: [MAD19])

In kV rated machines, the secondary insulation around the coil is much thicker and a poor thermal conductor and so some machines integrated separate cooling ducts within the coil. As an example, Figure 2.5 shows a cross-section through a winding from a large commercial machine with a repeating sequence of 4 rectangular copper conductors and 1 hollow tube which is made of stainless steel. In this case, the hollow conductor can remove the heat from within the main coil secondary insulation, which is often very thick in large high voltage machines. The reason for using stainless steel is that the cooling water which is inside the hollow conductor is usually not pure water so that a chemical oxidation reaction can occur with the interior side of the hollow conductor, and the stainless steel material can such avoid problems [WAN07].

Figure 2.5 Bar-wound coil with stainless steel water cooling ducts (Source: [WAN07])

In order to further reduce the thermal resistance from the conductors to the cooling fluid, direct cooling of the conductor can be used. This can involve flooding the entire stator with a flowing volume of oil [BAL19], spraying the winding with an oil mist [SHA23] or passing coolant through hollow conductors [CHE20, GEE24]. However, some of these direct methods introduce a lot of complexity in handling the fluids, sealing and compatibility of the coolant with insulation materials.

2.3 Hollow conductors

2.3.1 Introduction

Hollow conductors or separate cooling ducts within slots have been used for many years in large electrical machines [OST01,VOL18,UDD12]. Hollow conductors incorporate a continuous duct along the length of the conductor through which a liquid or gas coolant can be pumped to directly remove heat from within the conductor. By extracting the heat directly from the inside of the conductor there is no need for the heat to pass through any of the normal electrical insulation layers in the slot, which tend to be poor thermal conductors. Direct heat extraction from within the conductor offers a promising route to achieve very high power densities but raises many technical challenges.

The ducts in most commercial hollow conductors are circular but there are a few conductors available with ellipitical, oval or rectangular shaped ducts. Examples of smaller insulated hollow copper conductors of the type that could be used in small and medium electrical machines are shown in Figure 2.6. Including a cooling duct within a conductor reduces the amount of copper in the conductor which inevitably gives an increased DC resistance compared to a solid conductor of the same overall dimensions.

Figure 2.6 Examples of commercial hollow copper conductors (Source: Luvata)

A study reported in [GEE24] demonstrated the potential advantages of employing hollow conductors for direct liquid cooling in coreless linear motors. Figure 2.7 shows the two-dimensional schematic cross-section through the linear motor with hollow conductors. In this particular machine, the hollow conductor is rectangular with overall dimensions of 3.91mm × 5.69mm in the orientation shown with an inner duct which is 1.37mm ×3.14mm [GEE24]. This means that the duct takes away ~19% of the copper cross-sectional area which will give a corresponding increase in the DC resistance. The aim of the study was to provide very effective thermal management for a high-precision positioning system which is operating at a high force density in order to miminise the moving mass and so improve dynamic performance. Full design dimensional details were provided in [GEE24]. The proposed coolant was water which is a very effective and low viscosity coolant and may well be suitable for a factory or laboratory type application. Figure 2.8 (a,b) shows two different types of coils (Concept 1,2) made from copper hollow conductors based on their inlet and outlet configurations for the coolant [GEE24]. Concept 1 involves a single conductor winding with one inlet and one outlet, Concept 2 uses parallel-wound coils, each with its own inlet and outlet. The total length of the concept 1 with the single path was 860.8mm while the combined length of the two parallel coils is shorter at 825mm. The study systematically analysed these two concepts using magnetic and thermal modelling. Two motor topologies were a moving coil topology (MCT) and a moving magnet topology (MMT). For the moving coil approach, the analysis employed harmonic modelling techniques suitable for periodic structures, but for the moving magnet topology, a 3-D surface charge model was adopted because of finite length. [GEE24].

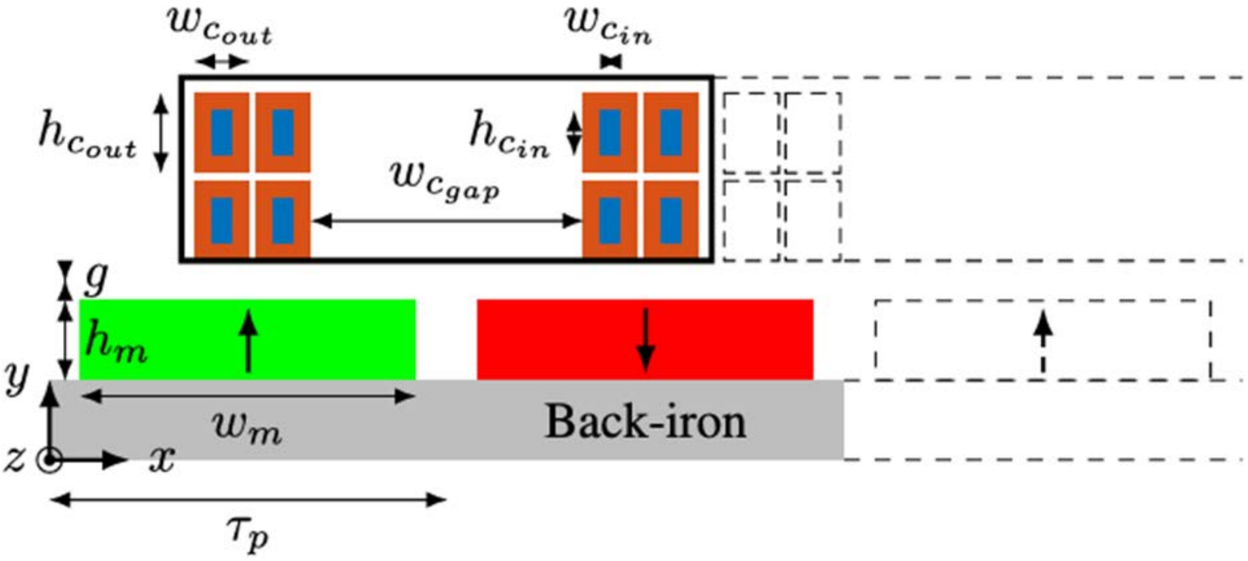

Figure 2.7 Two-dimensional cross-sectional view of the linear motor with coils manufactured from hollow conductors. (Source: [GEE24])

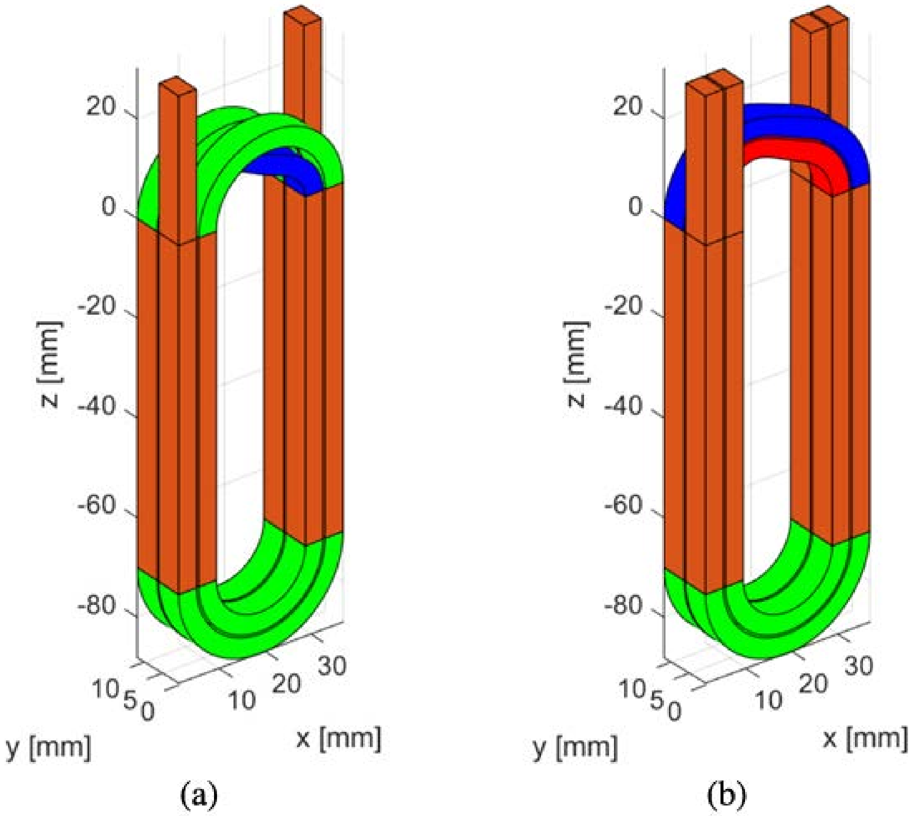

Figure 2.8 Alternative hollow coil arrangements: (a) Concept 1 with 4 turns of a single conductor per coil; (b) Concept 2 with 2 turns of 2 parallel conductors (different colours are for visualization purposes (Source: [GEE24])

It was claimed in this study that direct internal cooling through hollow conductors substantially reduces average copper temperatures compared to traditional cooling methods and even compared to state-of-the-art direct liquid-cooled linear motors using conventional conductors. However, the study identified some trade-offs notably the relatively low copper fill factor achieved with hollow conductors (29%) in comparison with conventional conductors (52%) and hence the torque constant of the proposed hollow conductor motor is was significantly lower. Of the two winding concepts, the design using two inlets and outlets (Concept 2) was more effective due to improved cooling performance, shorter individual winding lengths, and reduced pressure drop within the cooling system. [GEE24].

A study of hollow conductors in a 62.7kW permanent magnet machine was reported in [LIN17]. In this case holes were introduced in the end-winding regions of the hollow coils and oil flowed from the end of a flooded stator void through the ducts in the conductors in many parallel paths. A practical demonstration of this method of cooling was reported in [LIN17] in which the machine was able to operate at a current density of 20.8A/mm^2. This arrangement is different to the approach in this thesis which is based on an entirely sealed system in which the oil is forced through a continuous series path through the conductors which make up a phase winding.

The rectangular hollow conductor considered in this thesis is shown in the close up of Figure 2.9. It has an overall cross-section of 3mm x 2.3mm with a 1.3mm diameter circular duct at its center and four 0.5mm radiused corners which results in a net copper cross-section of 5.36mm^2. The radiused corners and the circular duct already reduce the conducting cross-section to ~78% of an equivalent 3mm x 2.3mm rectangular conductor. Of the 22% loss in conducting cross-sectional area, 19% is lost by incorporating the central duct and only 3% from the radiused corners. This is comparable with the 19% loss from a larger rectangular conductor with a rectangular duct in the study reported in [GEE24]. Hence, for the conductor used in this thesis, there is already a significant reduction in the eventual slot-fill factor that can be achieved compared to a solid strip conductor. The conductor is insulated with a PEEK coating.

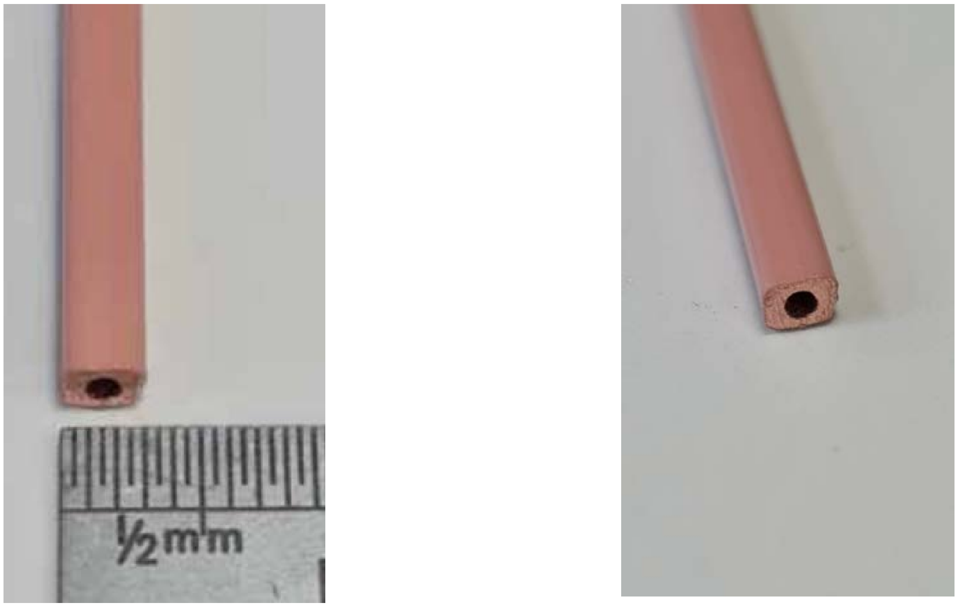

Figure 2.9 Rectangular hollow conductor used in this study.

2.3.2 Coil forming with hollow conductors

One of the difficulties of winding a coil with hollow conductors is that the minimum bend radius is greater than a solid conductor of the same overall cross-section. This larger bend radius is needed to avoid distorting the duct too much which could in the worst case pinch the duct closed. For example, Figure 2.10 shows the effect on the duct from bending a 4mm x 4mm square conductor with a circular 2mm duct at different bend radiuses [FOR23]

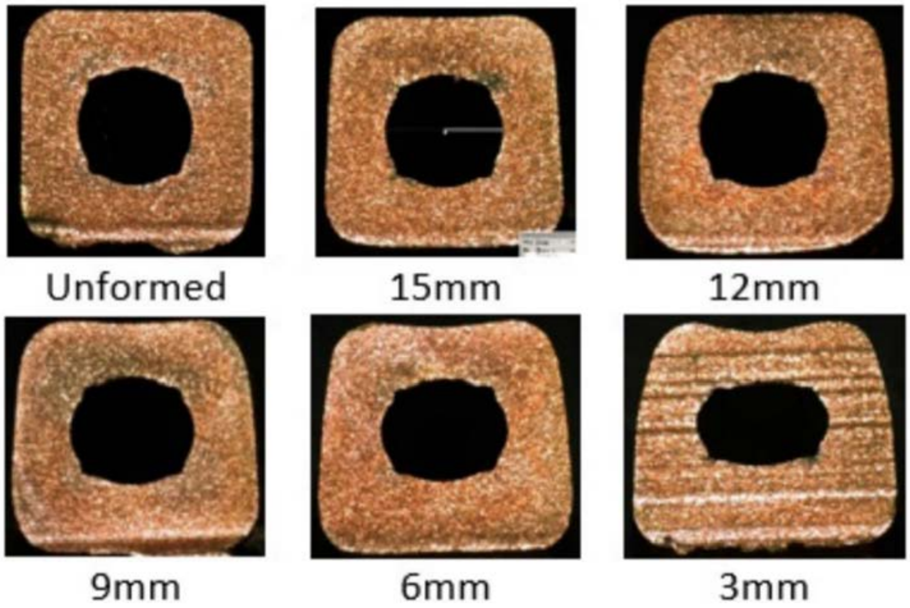

Figure 2.10 Effect of bend radius on the cross-section of a 4mm × 4mm hollow copper conductor (Source: [FOR23])

Manufacturer guidance recommends that a minimum bend radius of three times the width of the conductor is necessary to avoid problems of distorting the duct cross-section. For example, a 4mm × 4mm square conductor would have a minimum bend radius of 12mm and hence a simple semi-circular end-winding would have a minimum diameter of 24mm. In some cases, this may mean that the end-windings need to be modified to ensure that the bends in the end-windings meet this criterion. Figure 2.11 shows a CAD drawing of a stator wound with this 24mm bend radius rule applied to the end-windings [FOR20]. The end winding geometry to satisfy the minimum bend radius leads to a large winding which extends radially beyond the back of the stator core:

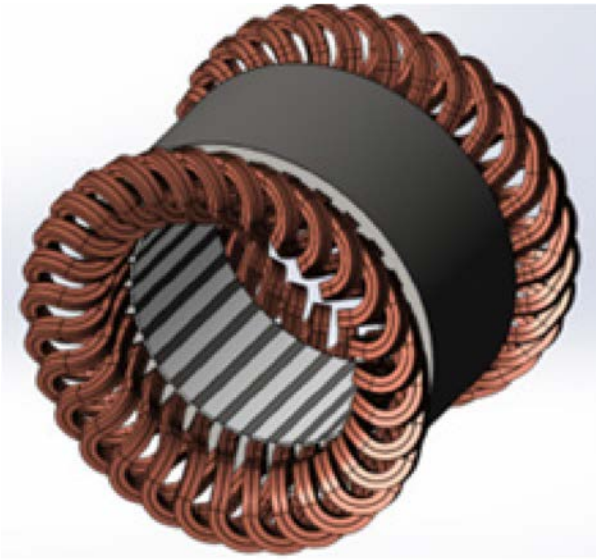

Figure 2.11 Proposed end-winding arrangement for a machine with a stator diameter of 180mm and 4x4mm conductor with a minimum bend radius of 12mm [FOR20]

The ideal coolant fluid which flows through the duct needs to satisfy several requirements:

Electrically insulating - In order to electrically insulate the windings and the converter from the rest of the system such as pumps, and coolant reservoir it is necessary to have an electrically insulating coolant. Insulating oil of the same type as used in transformers is ideal in terms of electrical properties but may not be the best in terms of thermal properties.

Low viscosity - The small duct sizes in many conductors means that a high viscosity coolant would be difficult to pump through without a high pressure drop. There will be a limit on the pressure that can be used and this discussed in more detail in the experimental studies in chapter 5.

High thermal conductivity - Although the coolant is directly in contact with the duct wall within the conductors, heat transfer into the bulk of the coolant requires a high thermal conductivity within the coolant, particularly if the flow in not turbulent.

High specific heat capacity - To minimise the flow rate and the temperature rise in the fluid, it is desirable for the fluid to have a high thermal capacity.

2.4 Induced eddy currents and AC resistance in hollow conductors

One important issue when using solid or hollow conductors in electrical machines is the problem of AC losses which are caused by eddy currents induced in the conductor [SUN23,SUN24]. A schematic representation of the source of eddy currents in square section conductor is shown in Figure 2.12 [JEW22]. The externally driven current produces a magnetic field which links the conductor itself which according to Faraday's law and Lenz's law results in an induced eddy current which flows the general current path shown in Figure 2.12. As can be seen, the induced current flows in a direction which opposes the external driven current in the centre of the conductor and adds to the current at the outer regions of the conductor. The overall effect is that the net current tends to flow at outer regions of the conductor which is known as skin effect. The magnitude of the eddy currents is related to the frequency of the external current and so the degree of skin effect depends on the frequency of the external driven current. The redistribution of current increases the loss in the conductor even though the same net current flows in the conductor and which means that the apparent resistance of the conductor is also increased which results in the concept of AC resistance. Many papers have been published on the calculation of AC losses in both stranded wires [BAR22,THO09,POP13] and bar or form-wound conductors [PAD22, SUN23,SUN24]. Time-stepped finite element is usually the preferred simulation method for calculating AC losses in machines.

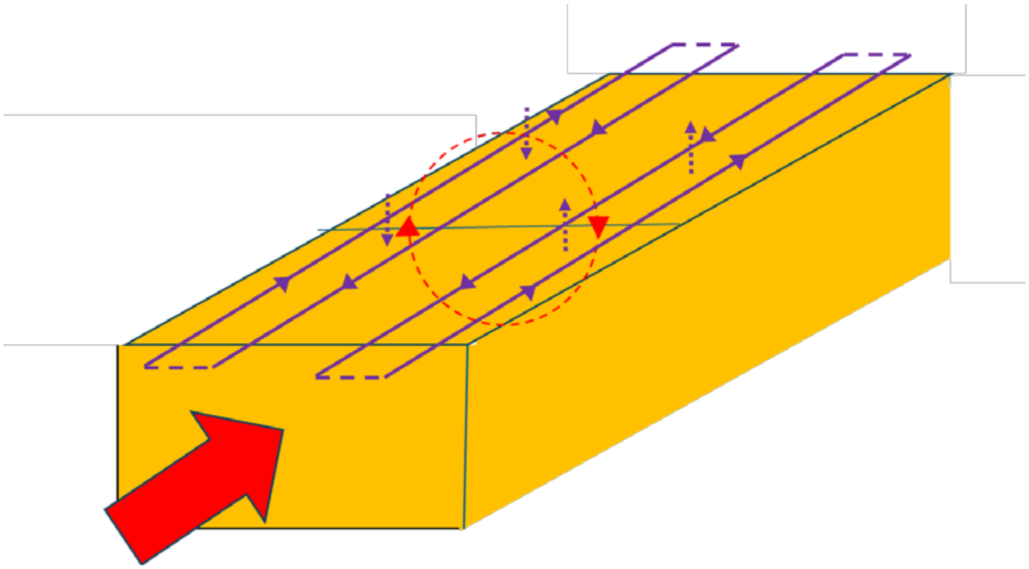

Figure 2.12 Schematic representation of induced eddy currents in a rectangular conductor (adapted from [JEW22])

2.5 Skin and proximity effect in conductors surrounded by air

One rule which is often used to determine if AC losses will be a problem in an electrical machine design is based on the skin-depth of the conductor material at the operating electrical frequency. This general rule states if the skin depth is greater than half the dimension of the conductor then it is likely that AC loss will not be too significant [GEE24]. The classical expression for skin-depth in a circular conductor is given by:

$$\delta = \sqrt{\frac{2}{\omega\mu\sigma}} = \sqrt{\frac{1}{\pi f \mu\sigma}} \qquad 2.2$$

where δ is the skin depth, f is the frequency of the current, μ is the magnetic permeability of the conductor ($= \mu_0$ in copper) and σ is the electrical conductivity.

Applying this to a copper with an electrical conductivity of 5.62x10^7 Sm^{-1} gives the variation in skin depth with frequency shown in Figure 2.13. At 1kHz the skin depth is 2.2mm, which suggests that the AC losses in conductor up to 4mm in diameter or 4mm wide would be not too significant.

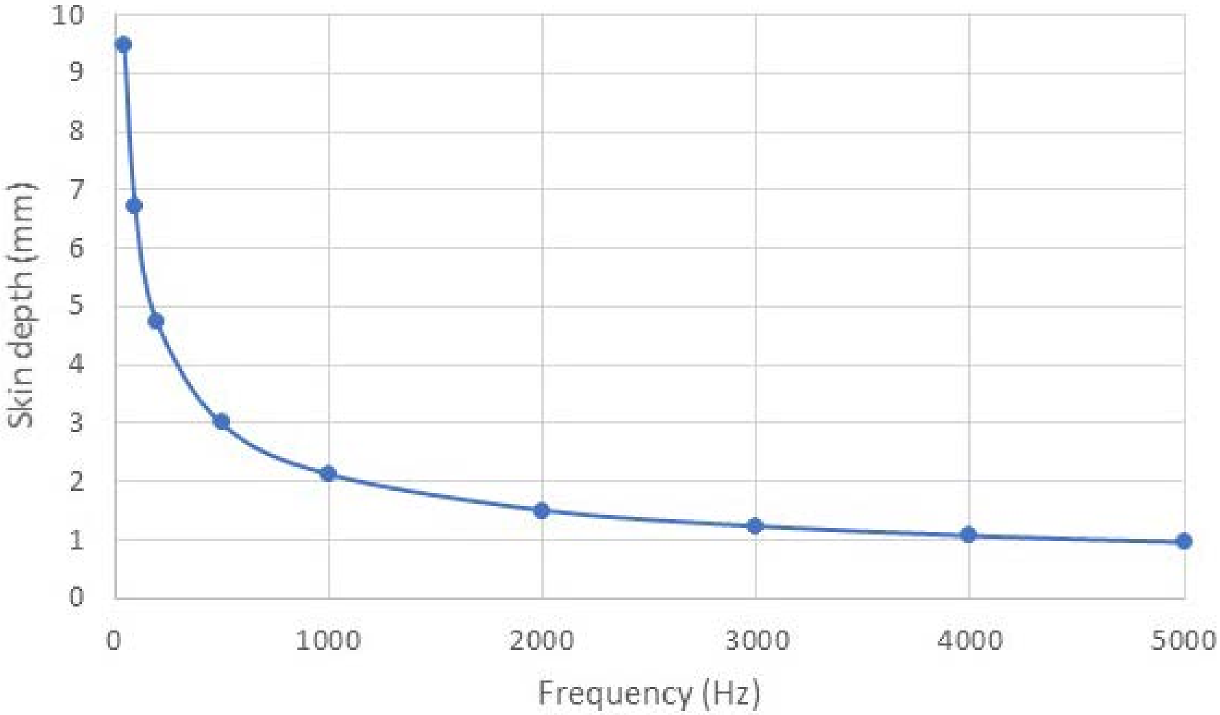

Figure 2.13 Variation in classical skin-depth in copper as a function of frequency

For the machine design investigated in chapters 3 and 4, the rotational speed is 6,000rpm, which corresponds to fundamental electrical frequencies ranging from 200 Hz for 4 poles to 500 Hz for 10 poles. On the basis of the simple classical skin depth calculation of equation 2.2 for an isolated conductor, it might be expected that AC losses would not be a problem in a 3mm x 2.3mm conductor. However, this expression for classical skin effect is based on a single conductor surrounded by air which is not representative of conductors in an electrical machine in terms of the presence of other conductors and the surrounding stator core. There are also published formulas for calculating the AC resistance of rectangular conductors such as equation 2.3 which is from [LEV30]:

$$\frac{R_{AC}}{R_{Dc}} = \sqrt[6]{0.178 + \left(\frac{h_{bar} w_{bar}}{2(h_{bar} + w_{bar)}} \sqrt{\sigma \mu \pi f}\right)^{6}} + 0.25 \tag*{2.3}$$

where h_{bar} and w_{bar} are the cross-sectional height and width of the rectangular bar and the other quantities are the same as those for equation 2.2.

In order to demonstrate the effect of other conductors and a surrounding magnetic core as well as the influence of duct on AC resistance, a series of steady-state AC simulations based on a complex representation of the sinusoidal current were undertaken for several different conductor arrangements.

2.6 Finite element modelling of skin and proximity effects in conductors

The eddy current behaviour of both hollow and solid rectangular conductors was simulated using the FLUX2D two-dimensional finite element simulation package. The simulation was set up using the steady state AC solution option in which a single solution is performed for a complex representation of the current variation, i.e. a $j\omega$ representation of the time derivative. This solution is based on a linear solution in which a single fixed value of magnetic permeability is specified for any soft magnetic components in the model. In the cases where multiple conductors are simulated, the conductors are series connected in a finite-element coupled electrical circuit driven by a steady-stator sinusoidal current source.

To model eddy currents using either a steady-state complex solution or a time-stepped solution, it is important that the individual conductors are meshed with a fine discretisation in order to represent the skin effect. The finite element mesh used to represent each conductor in this initial study is shown in Figure 2.14. It has 1152 second-order, rectangular, mapped mesh elements which is a good practical compromise between solution time, particularly in the machine level simulations in chapters 3 and 4, and capturing the detailed skin effect.

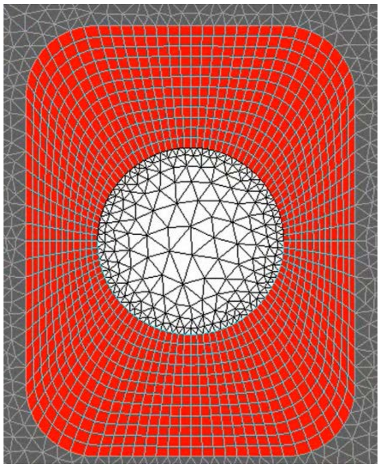

Figure 2.14 Mesh discretisation for a single hollow conductor

2.6.1 Single conductor in air

A series of simulations were performed for both solid and hollow (1.3mm diameter duct) rectangular copper conductors with overall dimensions of 2.3mm x 3mm with 0.5mm radii on each corner. The model consisted of a single conductor surrounded by air. The conductors were supplied by a current of 1A rms and the frequency was increased from 0.01Hz (which represents near DC conditions) to 5kHz. The current density distributions, effective resistance per unit length are summarised in Figure 2.15 (a) for the solid conductor and in Figure 2.15 (b) for the hollow conductor.

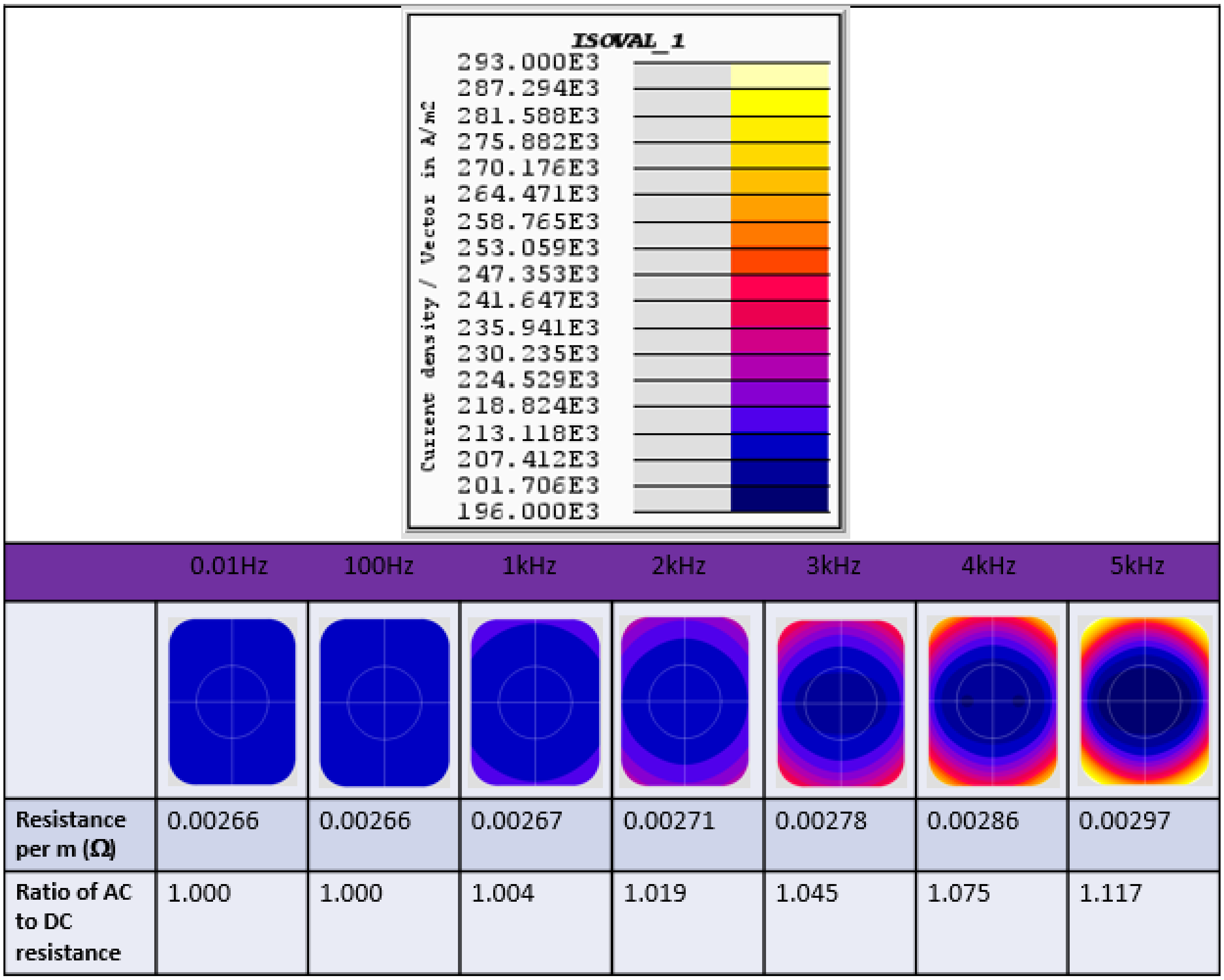

	0.01Hz	100Hz	1kHz	2kHz	3kHz	4kHz	5kHz
Resistance per m (Ω)	0.00266	0.00266	0.00267	0.00271	0.00278	0.00286	0.00297
Ratio of AC to DC resistance	1.000	1.000	1.004	1.019	1.045	1.075	1.117

(a) Solid conductor

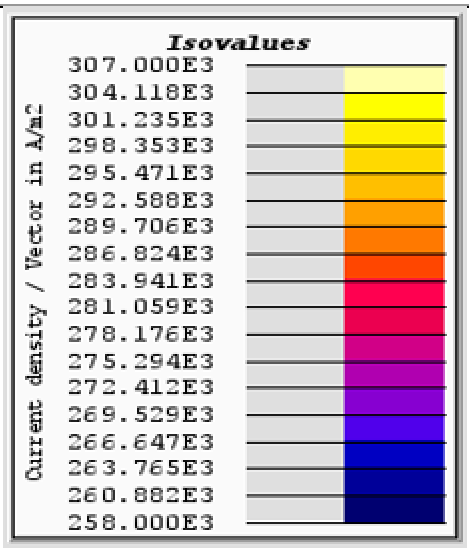

	0.01Hz	100Hz	1kHz	2kHz	3kHz	4kHz	5kHz
	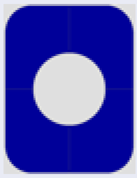	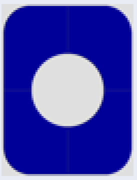	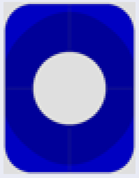	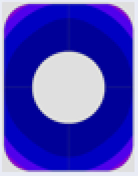	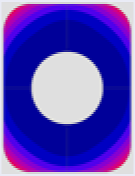	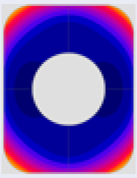	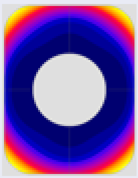
Resistance per m (Ω)	0.00332	0.00332	0.00332	0.00334	0.00336	0.00339	0.00343
Ratio of AC to DC resistance	1.000	1.000	1.000	1.006	1.012	1.021	1.033

(b) Hollow conductor

Figure 2.15 Summary of steady-state finite element modelling of a single conductor in air

As can be seen from Figure 2.15, the increase in resistance of these single conductors when surrounded by air is small, even up to 5kHz. The presence of a duct in the conductor means that the DC resistance (3.32mΩ per m) is higher than a corresponding solid conductor (2.66 mΩ per m). The percentage increase in resistance due to frequency effects relative to the DC value and hence the increase in loss (assuming the same temperature) is 11.7% for the solid conductor and 3.3% for the hollow conductor at 5kHz. There is some skin effect showing in the current distribution with current starting to concentrate at the outer edges as the frequency increases. It is worth noting that the peak current density range covered by the colour scale is only 196-293A/mm^2 and 258-357A/mm^2 for the solid and hollow conductors respectively. Hence, for the case of this single conductor surrounded by air, the current redistribution due to eddy current is not very significant, particularly for the fundamental frequencies of the machines in chapter 3 and 4 (200Hz for 4 pole and 500Hz for 10 pole). As expected, the AC loss effects are less significant in the hollow conductors due to the absence of conducting material in the center of the conductor.

2.6.2 Pair of conductors surrounded by air

The same process was repeated for the case of two conductors placed close to each and surrounded by air. These conductors were fed with the same current magnitude and phase and since the arrangement is symmetrical, the individual behaviour of the conductors can be expressed by the same values of effective resistance. Figure 2.16 (a) and 2.16 (b) shows the current density distributions and calculated effective resistance for the solid and hollow conductors respectively.

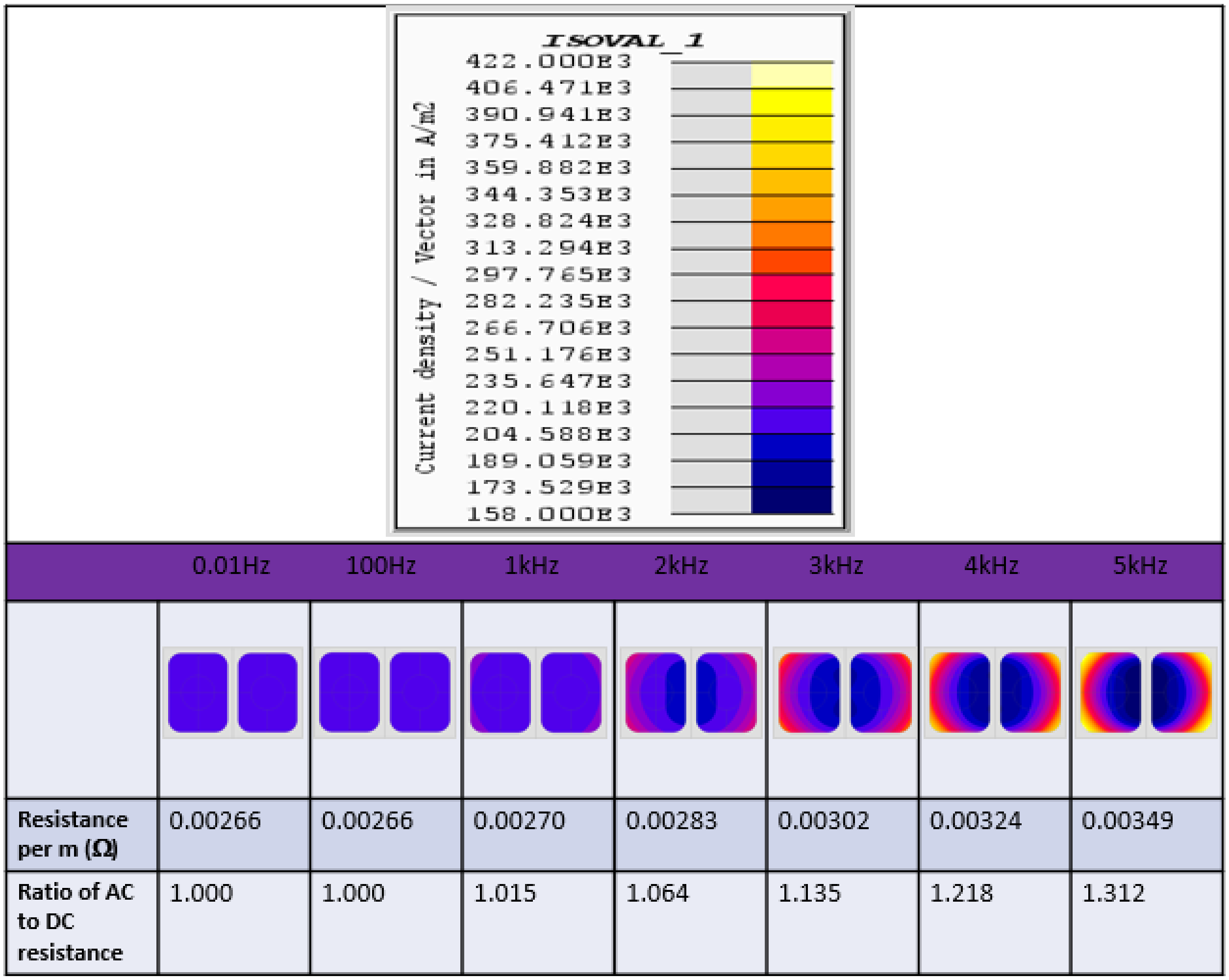

	0.01Hz	100Hz	1kHz	2kHz	3kHz	4kHz	5kHz
Resistance per m (Ω)	0.00266	0.00266	0.00270	0.00283	0.00302	0.00324	0.00349
Ratio of AC to DC resistance	1.000	1.000	1.015	1.064	1.135	1.218	1.312

(a) Solid conductors

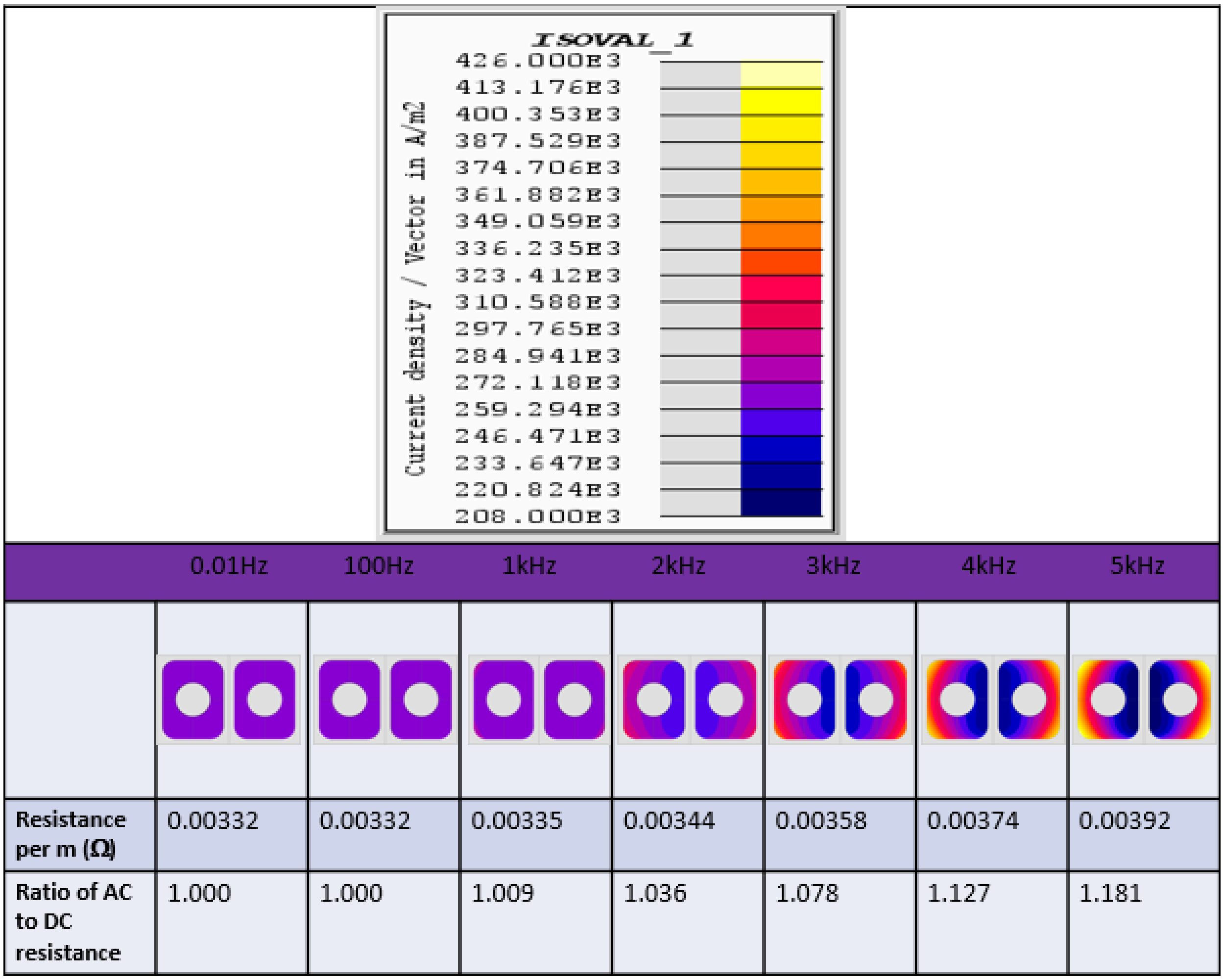

	0.01Hz	100Hz	1kHz	2kHz	3kHz	4kHz	5kHz
Resistance per m (Ω)	0.00332	0.00332	0.00335	0.00344	0.00358	0.00374	0.00392
Ratio of AC to DC resistance	1.000	1.000	1.009	1.036	1.078	1.127	1.181

(b) Hollow conductors

Figure 2.16 Summary of steady-state finite element modelling of a pair of conductors in air

As can be seen from Figure 2.16, there is more current redistribution in this pair of conductors compared to the single conductor arrangement and hence a greater increase in resistance as the frequency increases. As an example, at 1kHz there is a 3.6% increase in resistance of each of the two hollow conductors compared to a 1.9% increase in a single isolated hollow conductor in air.

2.6.3 Array of four conductors surrounded by air

The same procedure was repeated for 4 of the same conductors surrounded by air. Figure 2.17 (a) and 2.17 (b) shows the resulting current density distributions and calculated effective resistance for the solid and hollow conductors respectively.

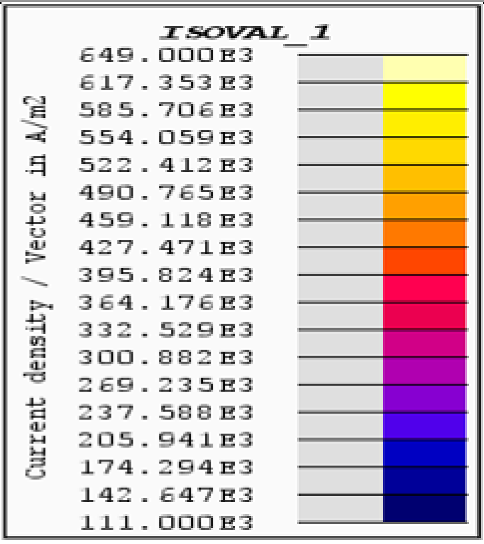

	0.01Hz	100Hz	1kHz	2kHz	3kHz	4kHz	5kHz
	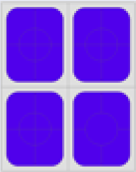	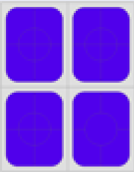	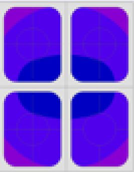	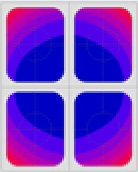	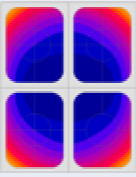	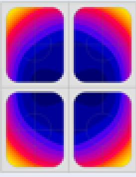	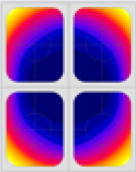
Resistance per m (Ω)	0.00266	0.00266	0.00282	0.00323	0.00372	0.00420	0.00465
Ratio of AC to DC resistance	1.000	1.000	1.060	1.214	1.398	1.579	1.748

(a) Solid conductors

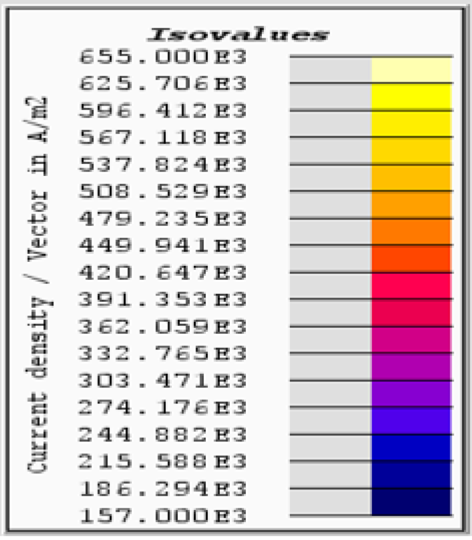

	0.01Hz	100Hz	1kHz	2kHz	3kHz	4kHz	5kHz
	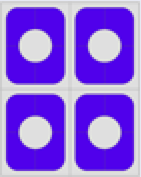	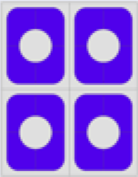	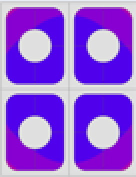	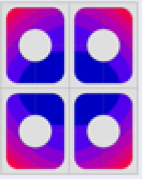	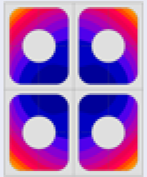	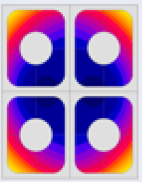	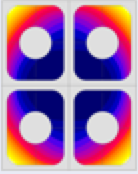
Resistance per m (Ω)	0.00332	0.00332	0.00347	0.00384	0.00429	0.00474	0.00513
Ratio of AC to DC resistance	1.000	1.000	1.045	1.157	1.292	1.428	1.545

(b) Hollow conductors

Figure 2.17 Summary of steady-state finite element modelling of four conductors in air

It can be seen that again the arrangement is symmetrical and hence each of the 4 conductors behaves exactly the same. As would be expected, since each conductor is subjected to greater proximity effects, there is a further increase in the AC resistance. Again, looking at the hollow conductors at 1kHz, the resistance is increased by 4.5% compared to the 3.6% for the two conductors.

2.6.4 Array of eight conductors surrounded by air

The same procedure was repeated for 8 of the same conductors surrounded by air. Figure 2.18 (a) and 2.18 (b) shows the current density distributions and calculated effective resistance for the solid and hollow conductors respectively. It can be seen that this arrangement has two resistance values since the middle 4 conductors of the array are exposed to different fields compared to the pairs on conductors at the end of the winding. As shown the eddy current effects in the centre of the array are far more significant than those in the conductors at the ends.

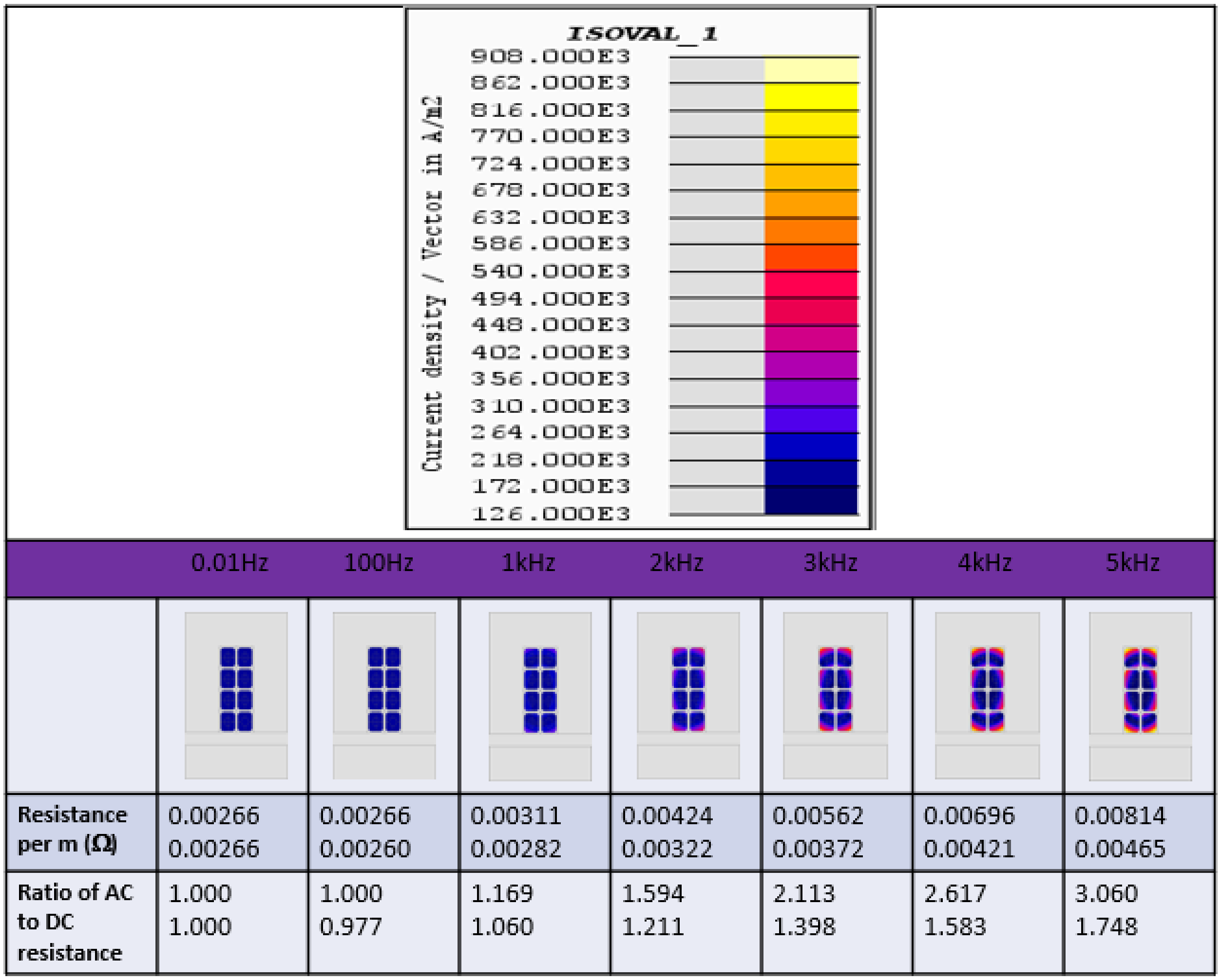

	0.01Hz	100Hz	1kHz	2kHz	3kHz	4kHz	5kHz
Resistance per m (Ω)	0.00266 0.00266	0.00266 0.00260	0.00311 0.00282	0.00424 0.00322	0.00562 0.00372	0.00696 0.00421	0.00814 0.00465
Ratio of AC to DC resistance	1.000 1.000	1.000 0.977	1.169 1.060	1.594 1.211	2.113 1.398	2.617 1.583	3.060 1.748

(a) Solid

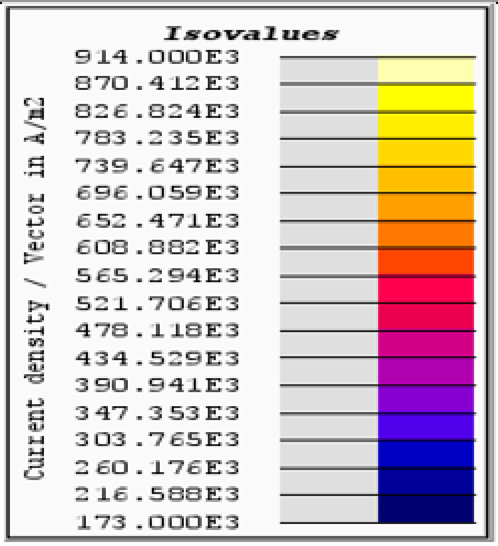

	0.01Hz	100Hz	1kHz	2kHz	3kHz	4kHz	5kHz
	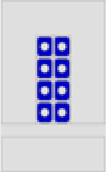	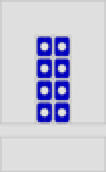	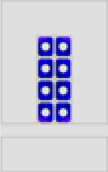	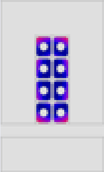	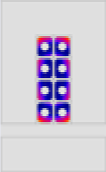	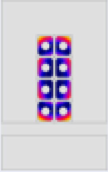	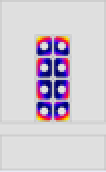
Resistance per m (Ω)	0.00332 0.00332	0.00332 0.00332	0.00375 0.00346	0.00484 0.00383	0.00620 0.00430	0.00753 0.00476	0.00871 0.00517
Ratio of AC to DC resistance	1.000 1.000	1.000 1.000	1.130 1.042	1.458 1.154	1.867 1.295	2.268 1.434	2.623 1.557

(b) Hollow

Figure 2.18 Summary of steady-state finite element modelling of 8 conductors in air

2.6.5 Summary of different conductor arrangements in air

Figure 2.19 shows a summary of the resistance as function of frequency for the different conductor arrays. There are two values for the 8 conductor arrays as the middle 4 conductors of the array are exposed to different fields compared to the pairs on conductors at the end of the arrangement. Over this of frequencies, there is a significant increase in loss due to AC losses and even at 1kHz, the increase is up to 13% in the 8 conductor array.

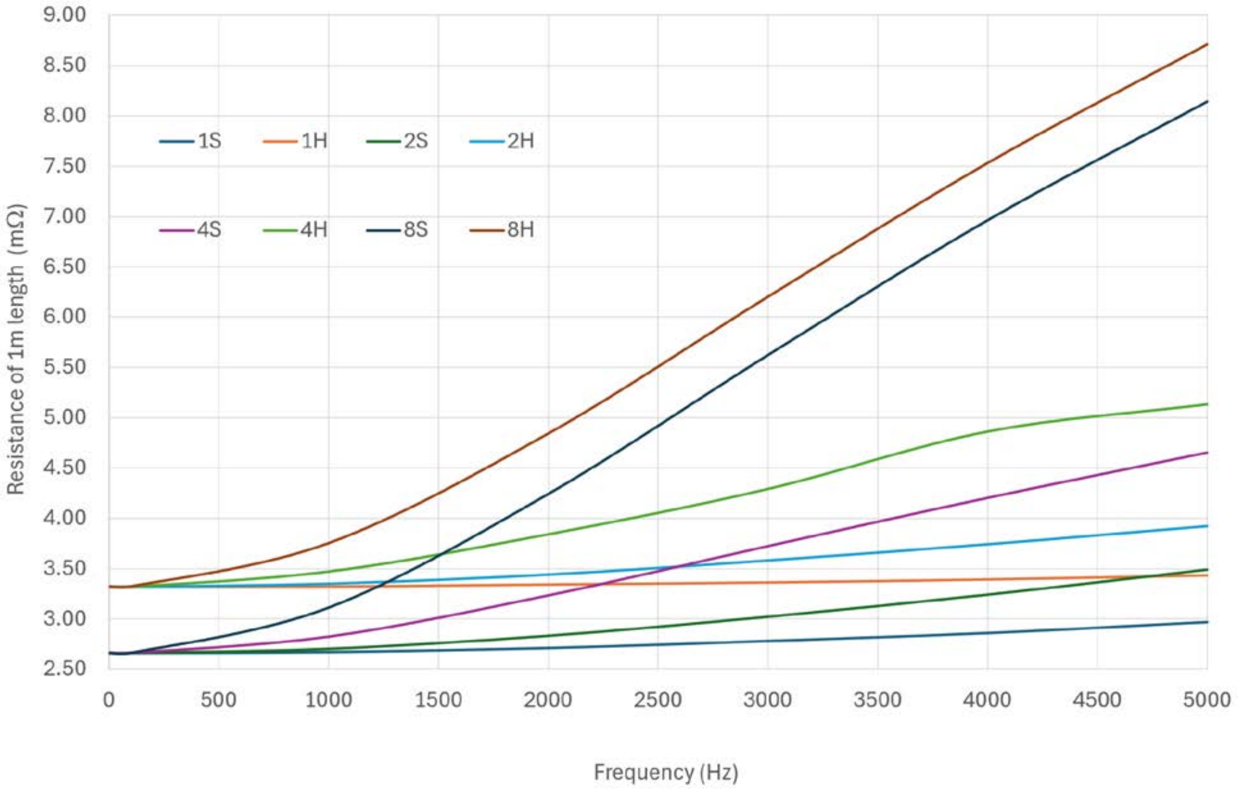

Figure 2.19 Summary of steady-state finite element modelling of conductors in air

2.6.6 Skin and proximity effects of conductors in a stator slot

The calculated AC resistance effects in air in section 2.4 showed that gradually increasing the number of conductors increased the AC loss due to proximity effects. The analysis above was for conductors in air but in almost all practical machines the conductors are placed in slots in a stator core. The same process was therefore repeated with an array of 8 conductors but they were surrounded by a single slot representation of a stator and rotor core. Since this is a steady state complex representation of sinusoidal excitation, it is necessary to specify a fixed linear permeability. In this case, a fixed relative permeability of 5000 was used. The airgap between the rotor and stator was set at 2mm. The results of these simulations are shown in Figure 2.20. In this case, there are 4 values of resistance (listed in order from the front of the slot) since the airgap introduces some asymmetry into the domain and so each layer of the winding has a different resistance. As shown, including the core in the model significantly increases the AC resistance particularly for the conductors near the slot opening when an increase of 10 in resistance is present at 1kHz.

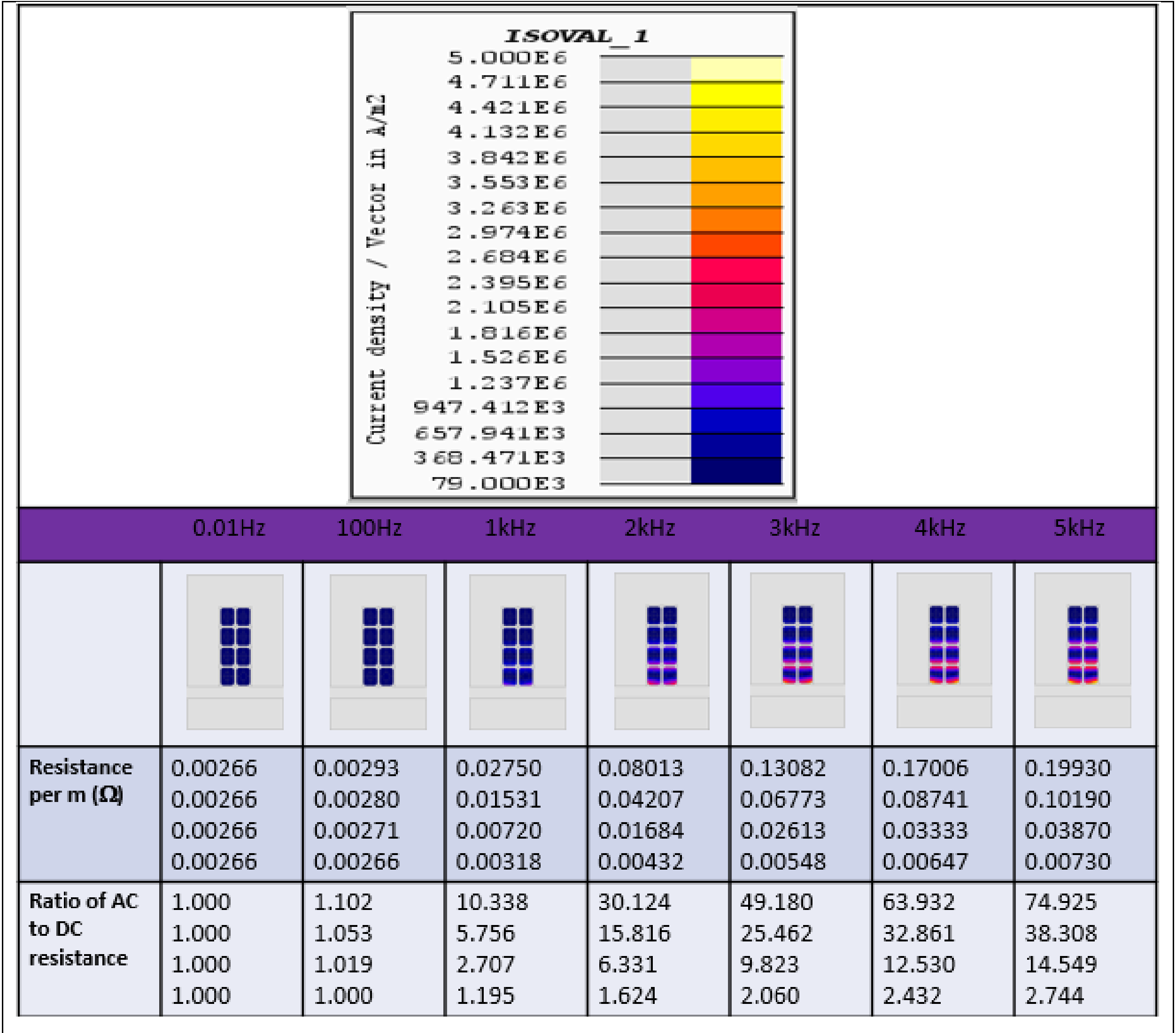

	0.01Hz	100Hz	1kHz	2kHz	3kHz	4kHz	5kHz
Resistance per m (Ω)	0.00266 0.00266 0.00266 0.00266	0.00293 0.00280 0.00271 0.00266	0.02750 0.01531 0.00720 0.00318	0.08013 0.04207 0.01684 0.00432	0.13082 0.06773 0.02613 0.00548	0.17006 0.08741 0.03333 0.00647	0.19930 0.10190 0.03870 0.00730
Ratio of AC to DC resistance	1.000 1.000 1.000 1.000	1.102 1.053 1.019 1.000	10.338 5.756 2.707 1.195	30.124 15.816 6.331 1.624	49.180 25.462 9.823 2.060	63.932 32.861 12.530 2.432	74.925 38.308 14.549 2.744

(a) Solid conductors

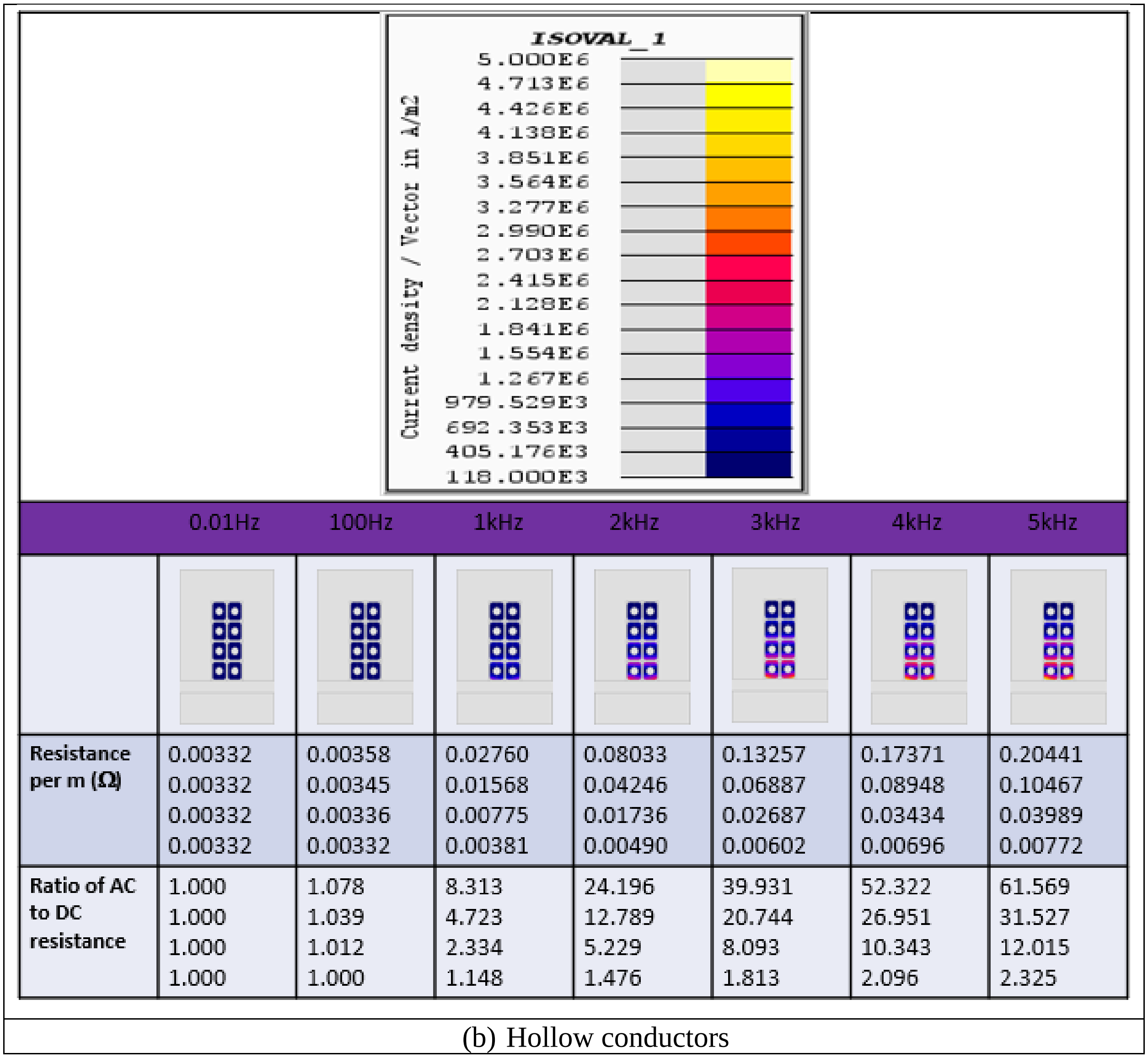

	0.01Hz	100Hz	1kHz	2kHz	3kHz	4kHz	5kHz
Resistance per m (Ω)	0.00332 0.00332 0.00332 0.00332	0.00358 0.00345 0.00336 0.00332	0.02760 0.01568 0.00775 0.00381	0.08033 0.04246 0.01736 0.00490	0.13257 0.06887 0.02687 0.00602	0.17371 0.08948 0.03434 0.00696	0.20441 0.10467 0.03989 0.00772
Ratio of AC to DC resistance	1.000 1.000 1.000 1.000	1.078 1.039 1.012 1.000	8.313 4.723 2.334 1.148	24.196 12.789 5.229 1.476	39.931 20.744 8.093 1.813	52.322 26.951 10.343 2.096	61.569 31.527 12.015 2.325

(b) Hollow conductors

Figure 2.20 Summary of steady-state finite element modelling of 8 conductors in air

This demonstrates that for the winding and as a whole and for the conductors near the slot opening in particular, the AC loss effect is much bigger than suggested by the simple skin effect formula which was suggested in [GEE24] as useful indicator.

2.7 Magnetic slot wedges

The slot opening in electrical machine stators is a necessary feature in a stator core. In most machines, non-magnetic slot wedges made from glass fibre composites or plastic extrusions are used to keep the winding in place and protect the conductors. Examples of conventional slot wedges are shown in Figure 2.21(a) and (b). However, these glass fibre or composite wedges allows time-varying magnetic flux from the rotor permanent magnet to directly pass into the slot and hence generate eddy current loss in the stator winding. One way of reducing the flux which crosses the stator winding from the airgap is to use magnetic slot wedges to screen the stator winding. In some machines, magnetic slot wedges are used to both provide the mechanical function of conventional slot wedges and some degree of magnetic shielding. These wedges are made by mixing ferromagnetic powder with a flexible polymer to produce a structural component. In order to retain sufficient mechanical properties the magnet powder is limited to 60-70% of the overall volume.

(a) Rigid glass-fibre composite wedges (Source: [LIN13])

(b) Flexible polymer slot wedges

(c) Magnetic slot wedges

Figure 2.21 Different types of slot wedges used in electrical machines

2.8 Irreversible demagnetisation

One factor that must be checked during the design of any permanent magnet machine is the need to avoid irreversible demagnetisation of the permanent magnets. This is particularly important in machines with high stator current densities or operating at high temperature. Irreversible demagnetisation occurs in a permanent magnet machine when the field applied drives the working point beyond the ‘knee’ of the normal demagnetisation characteristic. When the field is removed the magnet operating point recoils back up a parallel line with a permanent loss of magnet flux. This loss flux can only be recovered by remagnetising the magnet using magnetiser, a process that will usually need some disassembly of the machine and possibly removal of the magnet pieces for re-magnetisation.

The process of irreversible demagnetisation is shown in the simplified second quadrant demagnetisation characteristic in Figure 2.22 [JEW21]. The magnet operates at its normal operating point in the second quadrant of the demagnetisation characteristic with no external field applied to it. The slope of the load line which determines this operating point depends on the magnet and airgap dimensions. When an external demagnetising field is applied to the magnet, e.g. by the stator winding of an electrical machine, the operating point is driven down the demagnetisation characteristics. Providing it is not driven beyond the linear region, the operating point recovers back up to the normal operating point when the external field is removed with no loss of flux. However, if the operating point is driven beyond the knee of the characteristic, then the magnet recovers back up a parallel and lower demagnetisation characteristic leading to a permanent loss of flux.

The key factor which determines whether a magnet is demagnetised depends on the position of the knee. It is important to the note that the distance that the operating point moves along the H axis for a particular applied mmf is inversely proportional to the magnet length. Hence, increasing the thickness of the magnet in the direction of magnetisaion helps avoid irreversible demagnetisation. However, the process shown in Figure 2.22 is very simplified and based on a single operating but in a real magnet, areas such as the corners are more sensitive to demagnetisation.

Temperature also has an effect on the possibility of irreversible demagnetisation as the knee-point tends to move further up the demagnetisation with temperature as shown in the example shown in Figure 2.23 for Vacodym 688AP which is a grade of NdFeB suitable for high temperature motor applications [VAC25]. As can be seen, for temperature up to 200°C, the knee point is in the 3rd quadrant of the demagnetisation characteristic. This does not mean that the magnets cannot be demagnetised but it does need the direction of flux in the magnet to be fully reversed and beyond. As well as checking for irreversible demagnetisation at rated current, it is common to check under fault current conditions. An assessment of demagnetisation in the preferred machine design is described in more detail in chapter 4.

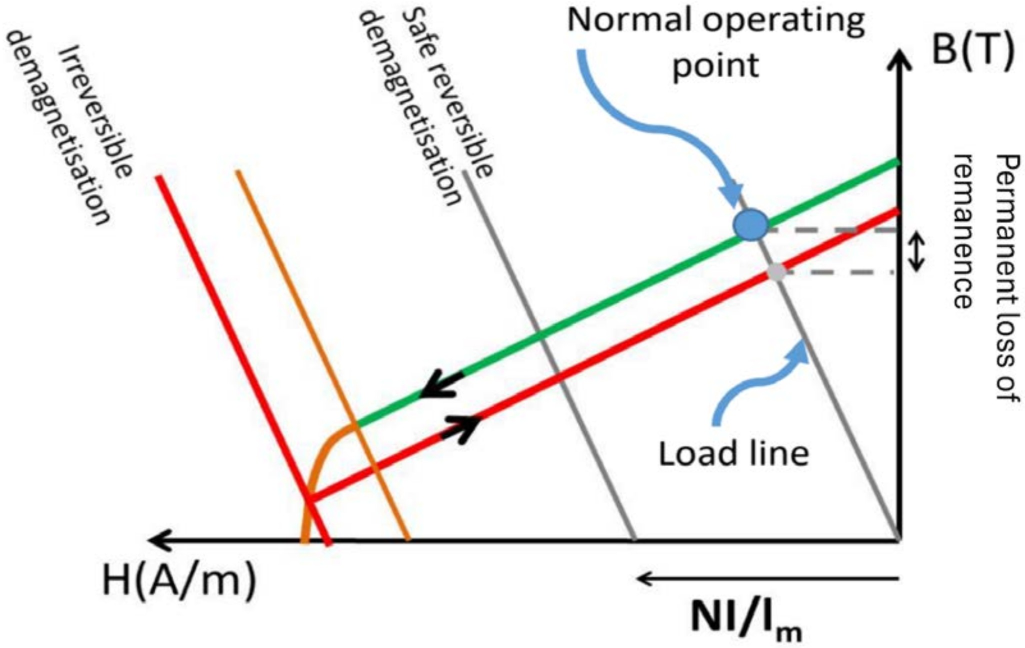

Figure 2.22 Schematic of irreversible demagnetisation in a permanent magnet

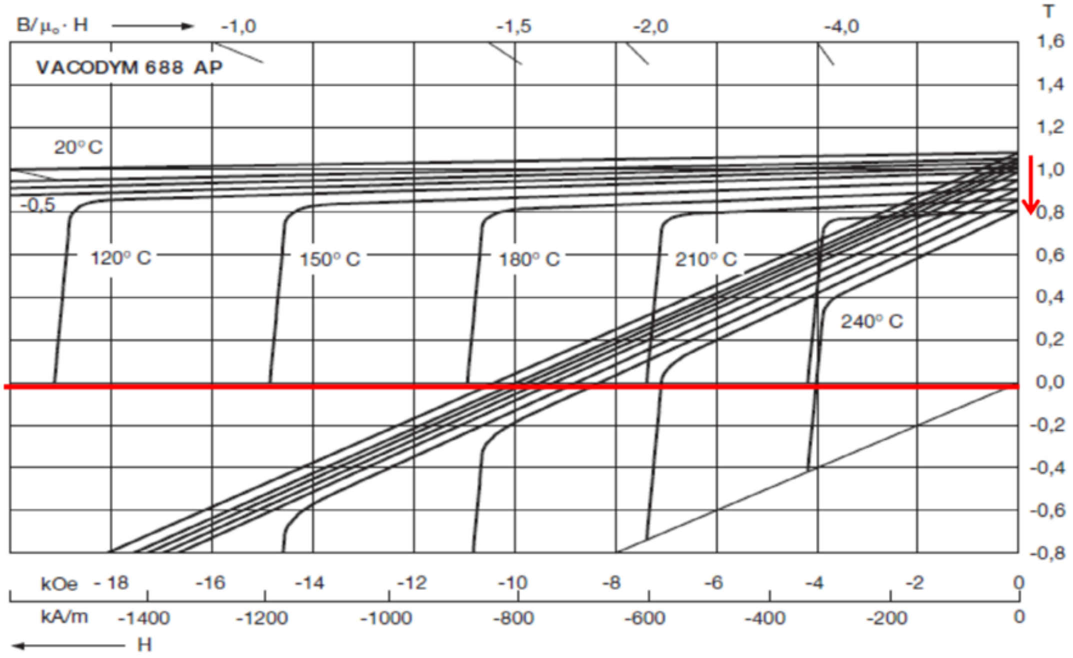

Figure 2.23 Demagnetisation characteristics of Vacodym 688 AP NdfeB at different temperatures (Source: [VAC25])

2.9 Summary

This chapter has described on some of the key technical issues around thermal management of electrical machines and in particular the use of hollow conductors for providing direct cooling. It has also that even in the smallest hollow conductors, care needs to be taken of AC loss effects.

Chapter 3 - Concentrated winding machine design study

3.1. Introduction

This chapter describes a design study to establish concentrated winding machine designs which are able to exploit the high current densities that can be used with hollow conductors to meet a typical aerospace propulsion specification. The design study uses a combination of MOTORCAD for initial sizing followed by finite element analysis with particular emphasis on saturation in the magnetic circuit and AC losses in the conductor.

3.2 Performance specification

3.2.1 Machine performance specification

The performance specification for the baseline machine is based on a typical propulsion motor specification for a hybrid propulsion aircraft with a series array of distributed fans and is shown in Table 3.1. The aim was to design a machine with a rated power of 250kW at 6,000rpm and to achieve this at a power density of up to 20kW/kg with an rms current density of approximately 40A/mm^2. This design study did not consider matching the winding to a particular voltage.

Table 3.1 Performance specification for machine design study

Rated power	250kW
Rated speed	6,000rpm
Rated torque	398Nm

3.2.2 Conductor details

The design was based on the smallest available hollow conductor manufactured commercially at the start of this research project. This is a 3mm × 2.3mm rectangular conductor manufactured by Luvata with a circular duct of 1.3mm diameter and a PEEK insulation coating. The conductor is shown in Figure 3.1. The corners of the conductor have a radius of 0.5mm. Allowing for the duct and the radiused corners the cross-sectional area of copper in each conductor is 5.36mm^2. The initial sizing of the machine was based on a conductor without radiused corners with a cross-sectional area of 5.57mm^2. It was only when a sample of the conductor was delivered that the small 0.5mm radius on the corners was noticed. For the original at 37A/mm2 rms this gives an rms current of 206.1 Arms and so a peak of 291.4 Apk. The actual peak used as the basis of the design study is 292.7A peak which is 38.6A/mm^2 rms with radius corners taken into account.

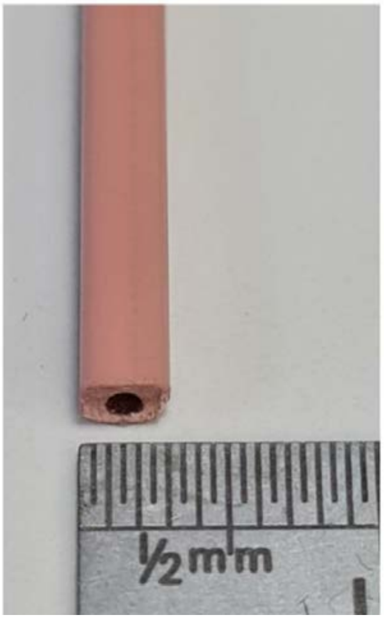

Figure 3.1 Commercially produced conductor used as the basis of the design studies

3.3 Machine design methodology and tools

3.3.1 Design tools

The sizing and design of the machines was initially done using MOTOR-CAD which is a commercial software used to guide designers in the design process by performing numerous calculations on a set of design parameters by the user. The software does not design machines itself as any changes to dimensions, winding parameters etc. are made by the user in response to predicted performance. This means that the user must have a good understanding of electrical machines and how parameter changes are likely to affect. MOTORCAD includes some in-built finite element analysis to perform some calculations but the mesh generation etc. is done automatically with no user involvement and the user cannot view the results and extract different aspects of electromagnetic behaviour as they would in a normal general purpose finite element package.

MOTORCAD allows the user to select different types of conductors, e.g. round wire and rectangular strip conductor but does not include an option to use hollow conductors. In order to use MOTORCAD for machines that use hollow conductors, it is necessary to use rectangular conductors and adjust the effective current density to account for the cooling duct. MOTORCAD was used to establish a machine design by trying various combinations of slots and pole numbers, dimensions etc.

3.3.2 Detailed finite element modelling of hollow conductors

Although MOTORCAD is a useful analysis tool to help a designer quickly try out many designs and has a finite element solver within the tool, it cannot represent the geometry of hollow conductors or model the eddy currents induced in the conductors. Therefore, after some preliminary design was done with MOTORCAD, more detailed finite element simulations were done with FLUX2D. This is a commercial finite element package which offers a lot of flexibility and contains many built-in post-processor features. The simple analysis of conductors in chapter 2 used a steady state-sinusoidal model, but for full machine analysis it is necessary to use a non-linear, time-stepped electric circuit coupled with motion of the rotor.

In order to capture skin effect in individual conductors it is necessary to have a finely discretised mesh in the individual conductors. However, there is also a need to model many separate conductors and surrounding machine structure and so the fine discretisation must be balanced with the overall mesh size and hence simulation time. Although most of the model is meshed with triangular elements, the conductor regions use a mapped mesh of rectangular elements which is better suited to modelling eddy currents. Figure 3.2 shows a close-up of the mesh in the slot.

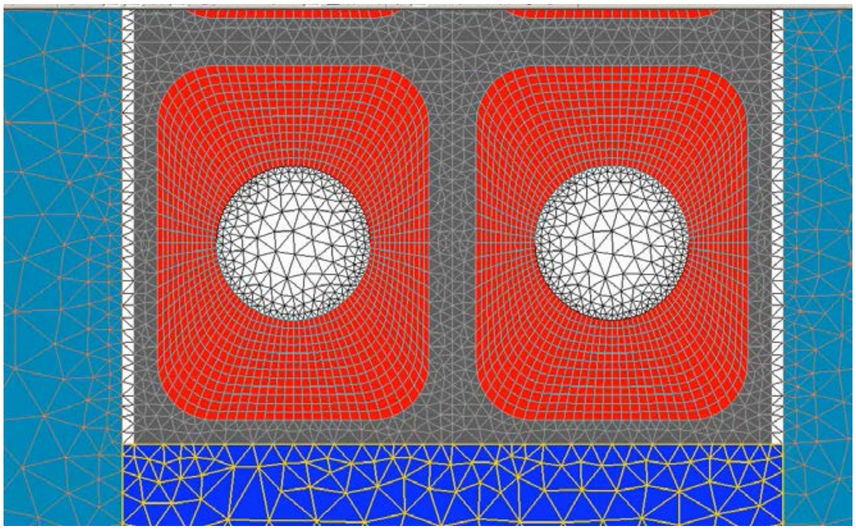

Figure 3.2 Finite element mesh in the slot

Wherever possible, electromagnetic symmetry was used to reduce the problem domain to the minimum periodic segment of the machine in order to decrease the computational time. For example, Figure 3.3 shows the 60° segment of the model for a 36 slot - 6 pole machine in which odd periodic boundary conditions are used to represent the full model.

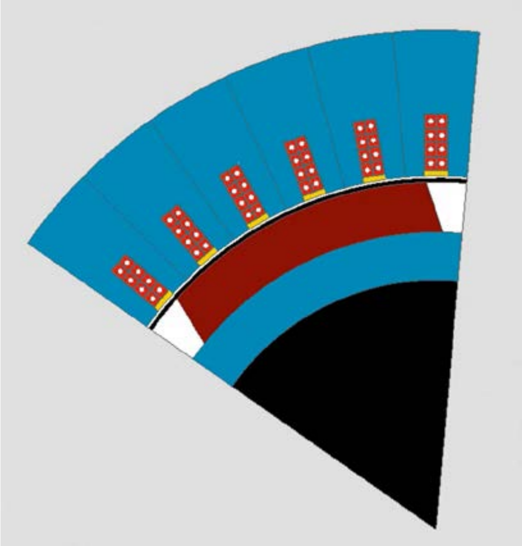

Figure 3.3 Problem domain for a 36 slot - 6 pole machine

Some of the geometries considered in this thesis such as the 12-10 machines do not have the symmetry to reduce the problem domain and so the full machine needs to be modelled. Model 6 slots. Table 3.2 shows some key information on the finite element models used in the analysis presented in this thesis. As would be expected with such a fine mesh and circuit coupling, the solution time for these models was very long, up to 2 days for the 12-10 models.

Every individual conductor in the finite element model was coupled to a solid conductor in the electrical circuit coupled to the finite element model. This allows both the induced eddy currents and the externally driven currents to flow in the conductors with all the necessary connections and conductor orientations. This resulted in very large circuits as shown in the example in Figure 3.4. Although the connections are straightforward with a simple three-phase star-connected, a great deal of careful implementation and checking was required to make sure that each conductor in the finite element model and the orientation of the solid conductor regions in the circuit were correct, particularly in the multi-layer concentrated windings.

Table 3.2 Details of the different finite element models used in this thesis

Slot - pole combinati on	Conductor arrangement with slot (wxh)	Number of slots modelled	Number of individual conductors modelled	Angle subtended by model	Number of elements
12-10	6x4	12 slots	288	360°	209,482
12-10	8x4	12 slots	384	360°	265,976
12-10	10x4	12 slots	480	360°	307,196
30-10	4x4	3 slots	48	36°	111,373
36-6	2x4	6 slots	48	60°	119,296
36-6	2x7	6 slots	84	60°	204,450
36-4	2x4	9 slots	72	90°	178810
36-4	3x4	9 slots	108	90°	256004

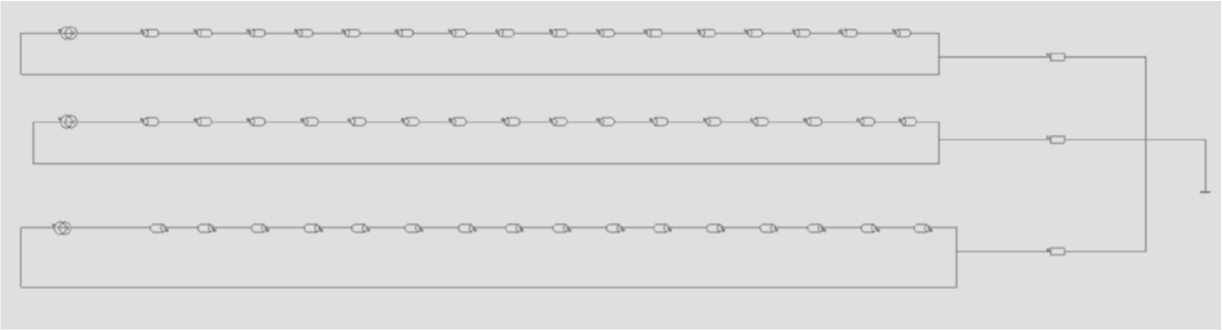

Figure 3.4 Typical electric-circuit which is coupled to the finite element region - example shown is a 30-10 machine with 4 x 4 array of conductors in a 3-layer winding

It is worth noting that the design studies in this chapter are based on simulations of performance in motoring mode. Some initial simulation results in generating mode showed a small difference (usually a few percent) between the torque produced in motoring mode and generating mode when the current waveform was simply shifted by 180° electrical. After careful investigation and checking of the model it was found that because the model is based on solid conductors in the stator winding with eddy currents being generated, the power loss in the winding was adding to the calculated electromagnetic generating torque. In all case the axial length of each machine was based on the requirement for a motoring torque of 398 Nm.

It is important to note that unlike magnetostatic simulations in which the copper loss can simply be scaled for temperature during post-processing, operation at different coil temperatures require separate solutions for the model used since the eddy currents in the conductors and hence the AC loss are a function of electrical resistivity and hence temperature. In this thesis, only two temperatures are considered which are 20°C and 150°C to show the effect of temperature on loss. It is also worth noting that the magnet temperature was not changed during the simulations and since the current is specified in the conductors, the torque produced is not a function of temperature.

3.4 Machine design studies

The initial sizing of the machine was started with the well-known sizing equation:

$$T = \frac{\pi}{2} D^2 L B Q \qquad 3.1$$

In order to calculate a rotor volume (D^2L) it is necessary to provide an initial estimate of the average airgap flux density (B) and the electric loading (Q). For a high performance machine with rare-earth magnets the average airgap flux density is typically 0.7-0.9T depending on the thickness of any rotor sleeve and the mechanical airgap. The electric loading varies with machine size but it would be expected that the electric loading will be high with hollow conductors and so a value 100-120kA/m provides a useful starting point noting. It is important to note that these starting estimates only provide a means of getting a starting point for MOTORCAD design and do not fix any of the dimensions but simply avoid too much iteration. Using $B = 0.75T$ and $Q = 120{,}000\mathrm{A/m}$, the rotor volume needs to be ~0.00442m^3. Setting the nominal axial length to 100mm gives a rotor diameter of ~170mm. These values were used as the starting point to iterate the designs in MOTORCAD.

Different combinations of winding type, slot number and pole number were selected as the starting point for designs to meet the performance specification of Table 3.1. There are several factors to be taken into account when selecting slot and pole combinations for electrical machines. A high pole number allows the back-iron thickness to be reduced but increases the electrical frequency. A higher electrical frequency results in higher iron loss and the potential for high AC resistance losses in the conductors. For the 6,000rpm performance specification, the electrical frequency ranges from 100Hz for 2 poles to 500Hz for 10 poles. The stator windings can be arranged as concentrated or distributed windings. In a concentrated machine, the end-windings are very compact compared to distributed windings but in most cases have a lower torque per amp. An important factor in determining the torque of a machine is the fundamental winding factor. Table 3.3 lists some of the fundamental winding factors for some common slot pole combinations up to 10 poles.

Table 3.3 Fundamental winding factors for different slot-pole combinations

Slot - pole	**Winding type**	**Fundamental winding factor**	**Comments**
3-2	Single tooth wound concentrated	0.866	Standard 1.5 slots per pole per machine concentrated machine
6-4	Single tooth wound concentrated	0.866	Standard 1.5 slots per pole per machine concentrated machine
36-4	Distributed single or two layer	0.96 - single layer	Other short-pitched windings

		0.945 - two layer	possible
9-6	Single tooth wound concentrated	0.866	Standard 1.5 slots per pole per machine concentrated machine
18-6	Distributed single-layer	1.000 - 1 layer full pitched	0.833 - 2 layer short-pitched
36-6	Distributed single-layer	0.966 - single layer 0.933 - two layer	Other short-pitched windings possible
12-8	Single tooth wound concentrated	0.866	Standard 1.5 slots per pole per machine concentrated machine
24-8	Distributed single or 2 layer	1.000 - 1 layer full pitched	0.833 - two layer short-pitched
15-10	Single tooth wound concentrated	0.866	Standard 1.5 slots per pole per machine concentrated machine
12-10	Single tooth wound concentrate - single or two layer	0.966 - single layer 0.933 - two layer	Non-standard ‘modular’ winding
30-10	Distributed single or two layer	1.000 - single layer full pitched	0.833 - two layer short-pitched

3.5 Concentrated winding machines

3.5.1 Introduction

As noted in chapter 2 concentrated winding machines have several advantages over distributed winding machines with more compact end-windings being the most important. For a machine with hollow conductors, the simpler form of the coil is also an important feature because of manufacturing challenges. A disadvantage of concentrated coils is the lower fundamental winding factor and hence torque per amp compared to a distributed winding machine. For concentrated 12 slot machines, the most common configuration would be the standard 1.5 slots per pole winding which gives a 12 slot-8 pole design. This has a winding factor of 0.866 and so there is a 13.4% reduction in torque capability compared to a 12 slot-4 pole fully-pitched distributed winding machine. Some of this can be recovered by moving to a 12 slot-10 pole design. This can have the same single or double layer winding arrangement as a 12 slot-8 pole machine, but the substitution of a 10 pole rotor for the 8 pole rotor increases the winding factor to 0.966 for the single layer winding which is only 3.4% lower than a distributed 12 slot design. A double layer 12-10 has a slightly lower fundamental winding factor of 0.933, which is still quite a bit higher than the 12-8 machine.

Therefore, a 12 slot, 10 pole machine could be a good compromise for power density with both a high fundamental winding factor and compact concentrated stator coils. It is also worth noting that a 10 pole machine will have a slightly thinner stator back-iron than the 8 pole machine which will give a weight reduction but a higher iron loss.

Three different winding types were considered for 12-10 designs. The first is a simple single-layer winding in which each slot contains a single coil-side as shown in Figure 3.5(a). For a 10 pole rotor this has a winding factor of 0.966. The two-layer winding in which two coils share a slot is shown in Figure 3.5(b). In this case, for a 10 pole rotor the winding factor is slightly lower at 0.933. It is worth mentioning that although the winding in Figure 3.4(b) contains concentrated coils which are wound around a single tooth and sit alongside the other coil sharing the slot, the terminology for this type of winding is a two-layer or double-layer winding even though the arrangement in the slot is usually not wound as two layers. This accepted terminology is used throughout this thesis.

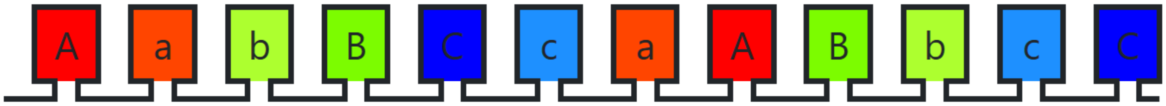

(a) 12 slot, single-layer winding for an 8 or 10 pole rotor

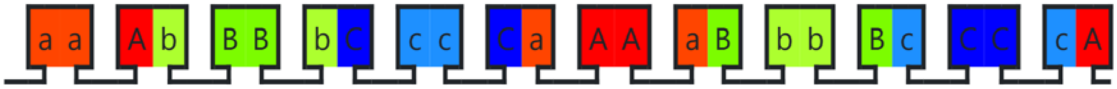

(b) 12 slot, two-layer winding for an 8 or 10 pole rotor

Figure 3.5 Alternative winding layouts for a 12 slot stator

One major disadvantage of both these winding arrangements is that they generate significant harmonics fields in the airgap that can cause high levels of rotor magnet loss. Unless these rotor magnet losses are managed through segmentation of the magnet they can lead to heating of the magnets and loss of performance and or permanent damage.

The third type of 12-10 winding considered is a multi-layer winding of the type described in [CIS10a, CHEN17]. An example of this type of winding for a 12 slot, 10 pole machine is shown in Figure 3.6. Although this machine has a complex winding arrangement, each individual coil is in fact a concentrated coil which is wound around a single tooth with various combinations of coils in each slot. This type of winding is useful for still having the compact and manufacturing advantages of concentrated coils, but allows some reduction in the harmonic fields generated in the airgap. However, this type of winding contains more interconnection between individual coils than a standard winding which could be a problem for hollow conductors in which any coil-to-coil connections must have electrical and coolant connections.

One interesting feature of this type of winding is that since the currents in the different coils are out of phase with each other, the net slot mmf at any instant will be lower than a single-layer winding for a particular slot size and peak phase current. This could reduce the proximity effect of AC losses in the conductors compared to a more conventional winding in which all the currents in the slot are in phase.

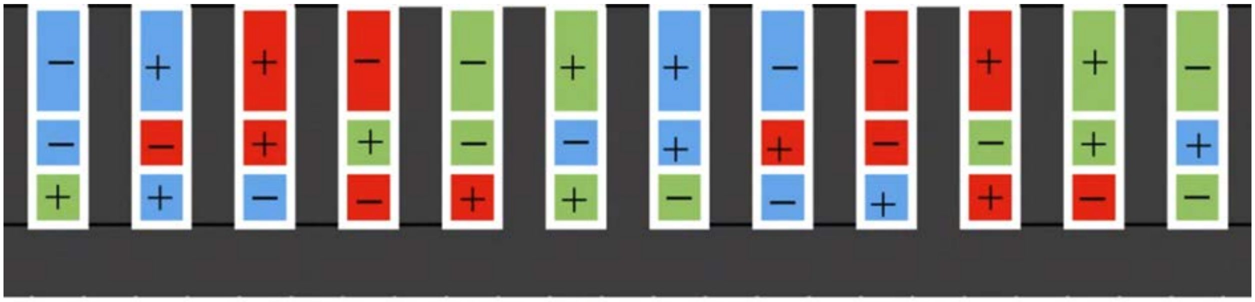

(a) 12-slot 10-pole triple layer windings

Figure 3.6 Example of a multi-later 12 slot 10 pole winding (Source: [CHEN17])

For a 12 slot and 10 pole combination, several different conductor arrangements per slot were considered as shown in Figure 3.7. These are all parallel slot designs with fully open slots. A total of 8 designs of 12 slot - 10 pole machines were initially considered and the dimensions of these designs are summarised in Table 3.4. They are all very similar in design except for the different winding layers and different number of conductors per slot. In some cases, the different winding arrangement resulted in some changes to the core dimensions. The wider slot of the 10×4 arrangements means that the flux captured by the narrower stator tooth is lower than for the 8×4 and 6×4 and so the back iron thickness was reduced in this design to give a smaller overall outer diameter.

It is worth noting that the number of turns per slot will proportionally affect the magnitude of the induced voltage and hence the matching of the winding to the supply voltage. The focus of this thesis is on torque density and losses and all the models are based on current sources. It is recognised that matching the winding voltage to a specific supply voltage in an aerospace application is an important practical consideration that could affect the selection of a particular winding and/or might require using combinations of parallel and series of wound conductors and coils or some compromise in the utilisation of the converter VA, but this is not a factor addressed in this thesis.

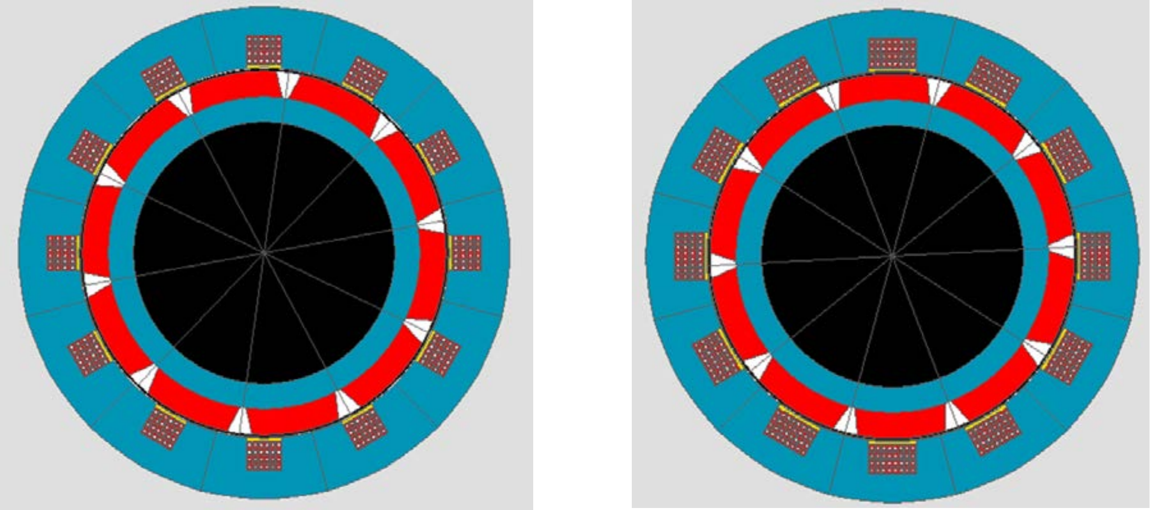

6×4 conductors per slot

8×4 conductors per slot

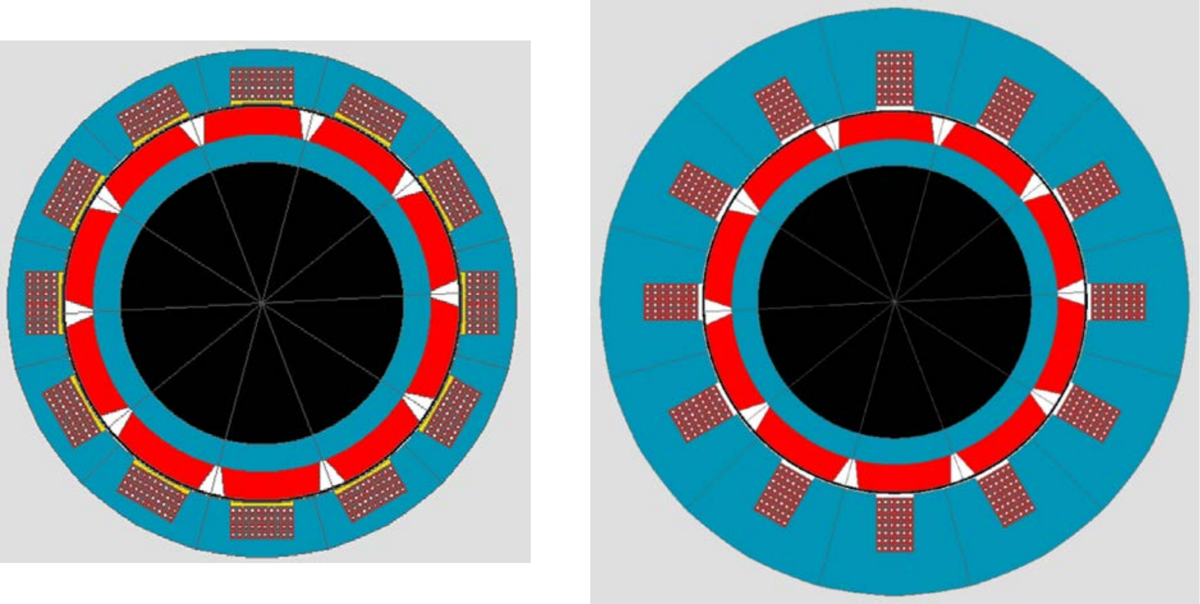

10×4 conductors per slot

6×7 conductors per slot

Figure 3.7 Cross-section through various 12 slot, 10 pole designs simulated in this chapter

Table 3.4 12-10 designs dimensions and winding arrangements

Design number	**1**	**2**	**3**	**4**	**5**	**6**	**7**	**8**
Slot number	12							
Pole number	10							
Winding layers	3	3	3	1	1	1	2	1
Conductors per slot (w×h)	24 (6x4)	32 (8x4)	40 (10x4)	24 (6x4)	32 (8x4)	40 (10x4)	40 (10x4)	42 (6x7)
Slot width (mm)	16.4	21.8	27.2	16.4	21.8	27.2	27.2	16.4
Slot depth (mm)	15.0	15.0	15.0	15.0	15.0	15.0	15.0	25.2
Tooth width (mm)	28.0	22.6	17.2	28.0	22.6	17.2	17.2	28
Stator outer diameter (mm)	226	226	216	226	226	216	216	258.4
Stator bore diameter (mm)	170							
Rotor outer diameter (mm)	169							
Rotor magnet sleeve thickness (mm)	1.0							
Rotor core thickness (mm)	11.5							
Magnet thickness (mm)	12							
Shaft diameter (mm)	120							
Air gap length (mm)	0.5							

Conductor width (mm)	2.3							
Conductor height (mm)	3.0							
Conductor bore diameter (mm)	1.3							
Conductor insulation thickness (mm)	0.2							
Axial length required to produce torque of 398Nm (mm)	113.4	90.0	90.1	122.4	88.6	86.7	91.7	64.6

Each design in Table 3.4 was simulated using a two-dimensional, transient time-stepped, circuit-coupled finite element model with solid conductor representation of each individual conductor at the rated current density of 38.6 A/mm^2 rms and at 6,000rpm. This representation of the individual conductors allows induced eddy currents to flow in the winding generating additional AC conductor losses. Simulations were performed for copper resistivities at 20°C and 150°C. These are not necessarily the expected operating conditions but are useful in demonstrating the effect of temperature over this range. The axial length of each design required to meet the torque specification of 398Nm was calculated from the finite element simulations from the torque per unit length calculated in the 2D finite element simulations. A summary of the predicted performance for the 8 designs at these two conductor temperatures are shown in Table 3.5.

Table 3.5 Predicted performance for the series of 12-10 designs

	1	**2**	**3**	**4**	**5**	**6**	**7**	**8**
Axial length required to produce rated torque of 398Nm (mm)	113.4	90.0	90.1	122.4	88.6	86.7	91.7	64.6
Total active region mass (excl. end-winding) (kg)	22.27	17.40	14.73	24.03	17.13	14.18	15.00	18.34
Power density (kW/kg) - based on active region mass only	11.23	14.37	16.97	10.40	14.59	17.63	16.67	13.63
Torque density (Nm/kg) - based on active region mass only	17.87	22.87	27.01	16.56	23.22	28.07	26.54	21.70
Copper loss at 20°C	10441	11955	15500	13229	12655	16920	16881	17116
Copper loss at 150°C	11043	12304	15797	13207	12604	16464	16689	15426
DC copper loss at 20°C	4645	4914	6143	5012	4840	5919	6260	4627
DC copper loss at 150°C	7017	7426	9283	7571	7314	8944	9459	6991
Inferred AC copper loss at 20°C*	5796	7041	9357	8217	7815	11001	10621	12490
Inferred AC copper loss at 150°C*	4026	4878	6514	5636	5290	7520	7230	8436

*Inferred AC copper loss - Calculated by subtracting analytically calculated DC loss from the finite element predicted conductor loss

The highest torque and power density are achieved with design 6 which has a single layer winding with a 10×4 conductors. This is marginally ahead of design 3 with a multi-layer winding. The three 10x4 configurations all have similar power densities which are significantly higher than the corresponding designs with 8x4 arrangements despite having narrower teeth and slightly thinner back iron to better match the flux captured by the narrower teeth. Figure 3.8 compares the predicted flux density throughout the machine for a 6x4 and 10x4 single layer arrangement i which both sets of contours are scaled the same to a maximum of 3.4T.

There are large differences in the AC losses between the designs. In order to make this a reasonable comparison, the designs with 10×4 conductors in each slot were compared. Taking the loss values at 150°C, the highest loss is achieved with a single layer winding (design 6 - 7520W) followed by the two-layer winding (design 7 - 7230W) and the lowest with the 3 layer winding (design 3 – 6514W). This is the order that would be expected given the net slot mmf is lower in the 2 and 3 layers winding due to the presence of conductors with an out of phase current in the same slot. It is also interesting that the copper loss at 20°C and 150°C is very similar for the full set of designs. This shows that the increase in the quasi-static losses due to the increased electrical resistivity is more or less balanced out by the lower AC losses due to the increased electrical resistivity for this series of designs at this electrical frequency.

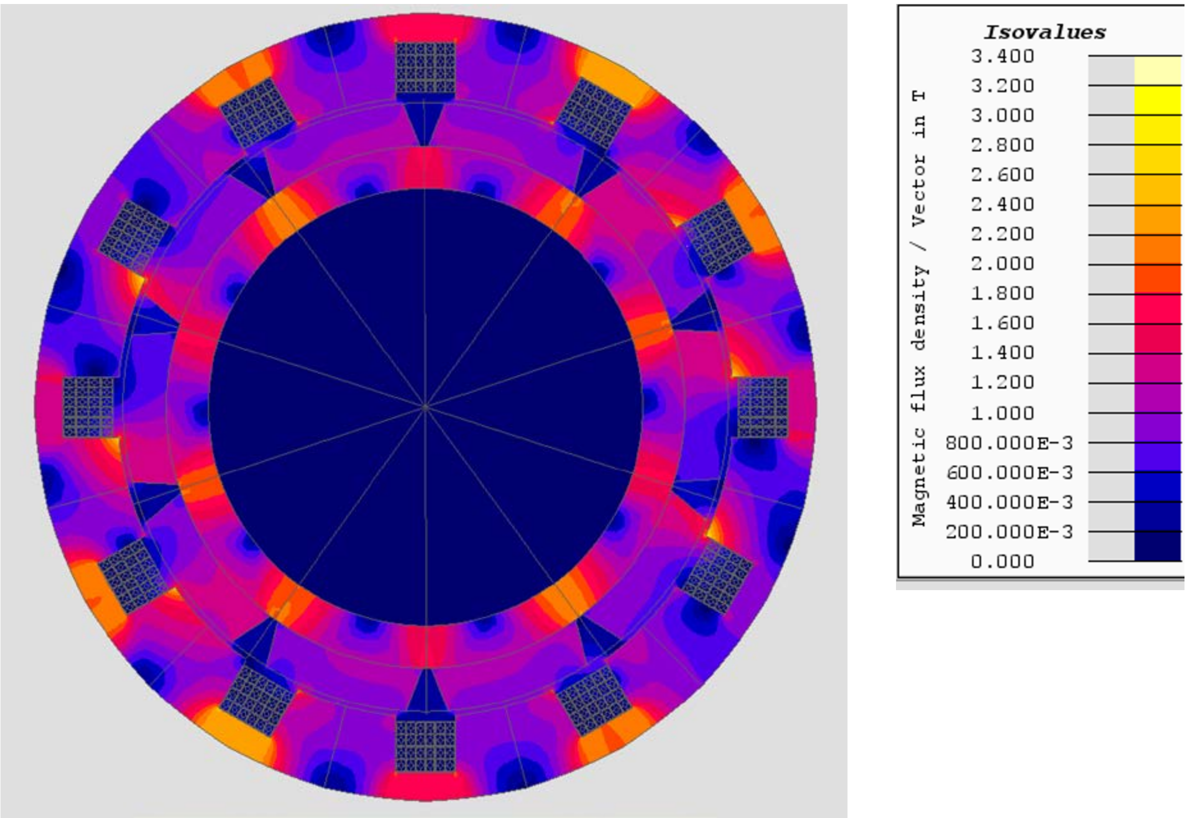

(a) 12-10, single-layer 6x4

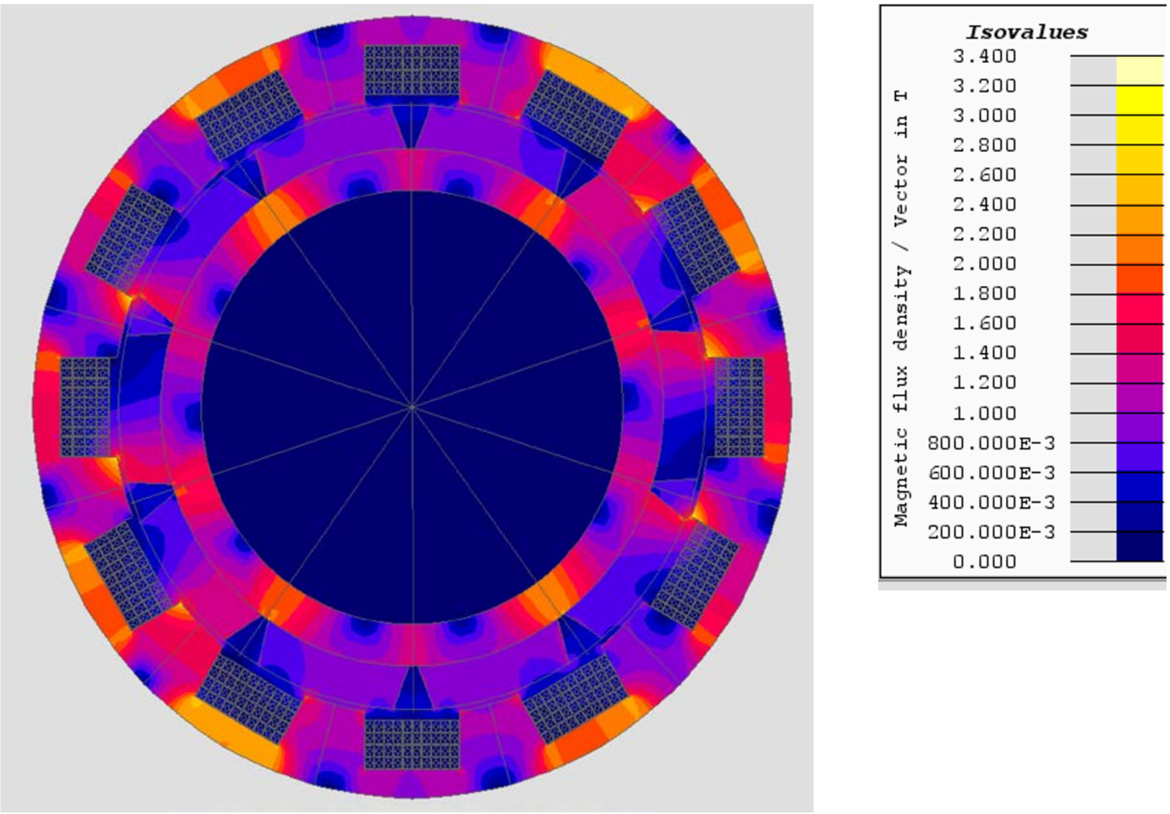

(b) 12-10, single-layer 10x4

Figure 3.8 Finite element predicted flux density distribution at rated torque

3.5.2 Detailed AC loss analysis of 12-10 machine with a single layer winding with 6x4 conductors per slot

As shown in Table 3.5, the highest AC losses were generated by the single-layer windings and so this was investigated further. Figure 3.9 shows a close up of one slot of phase A with a single layer coil with 6×4 conductors in each slot, i.e. design 4. These conductors are identified by a designation set by the slot number, row and number in that row in a counter-clockwise order.

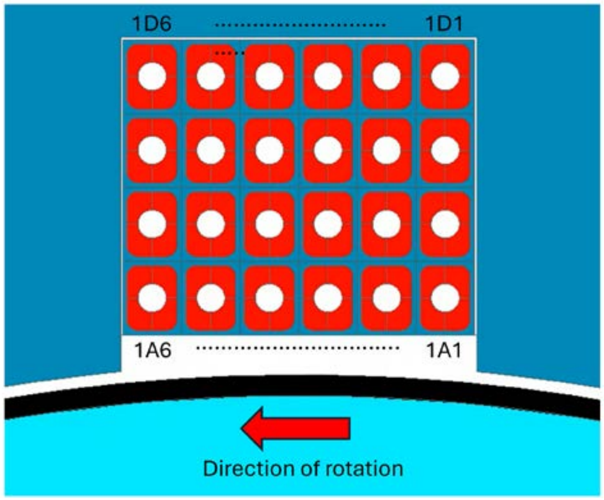

Figure 3.9 Close up of one slot of phase A of a 12 slot - 10 pole with a single layer winding

The current waveform for phase A referenced to the zero crossing at t=0 is shown in Figure 3.10 (a), while the corresponding variation in the total copper loss at 150°C in the four slots in phase A over one electrical cycle is shown in Figure 3.10(b). As noted previously in Table 3.5, the average loss for the machine is 13207W which corresponds to 4402W per phase. The significant role of induced eddy currents is shown by the loss waveform of Figure 3.11 in which the loss is still ~2500W when the current is zero and there is a phase shift between the peak of the current and the peak of the loss waveform.

The loss variation in the individual conductors in slot are shown in Figures 3.11 (a) (from the row nearest the airgap) and in Figure 3.11 (b) (at the back of the slot). As will be seen there is a significant variation in loss between the conductors located near the airgap, with conductor 1A6 having a much higher loss density than conductor 1A1. These two conductors are located at the ends of the front row of conductors, but the difference is related to the direction of rotation and the fact that the machine is operating in motoring mode. The behaviour in the back of the slot is very different, with all the conductors except 1D1 having very similar losses which are also much lower than the corresponding conductors in the front row. The loss in conductor 1D1is slightly higher which can be explained by the fact that the first conductors in each row have lower eddy currents and so there is less eddy screening of conductor 1D1from the airgap flux.

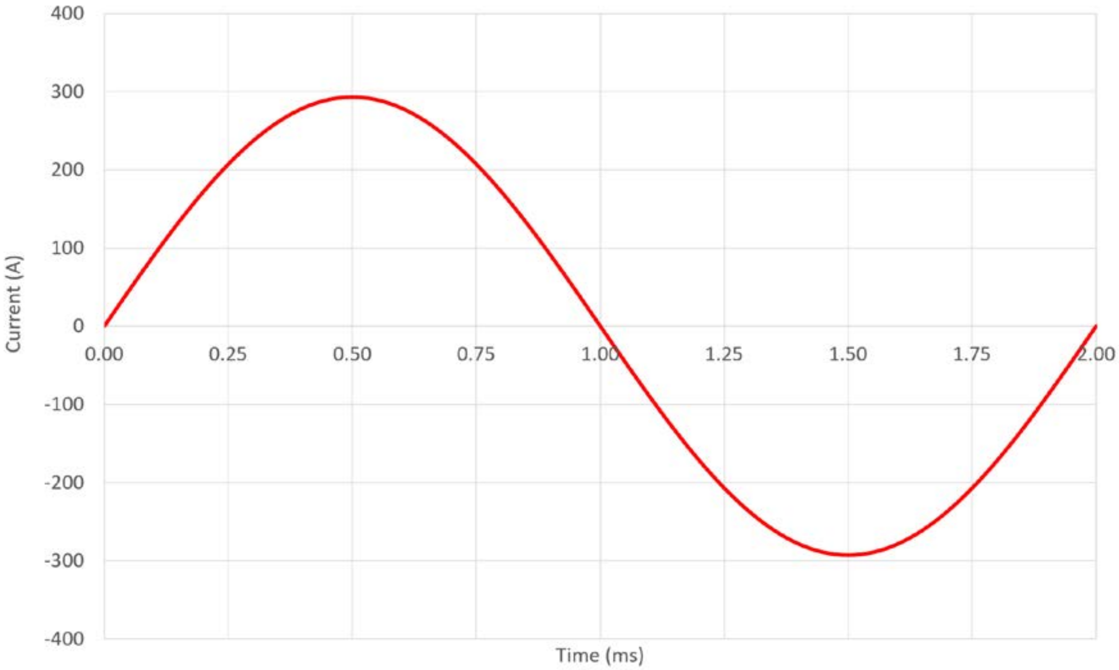

Figure 3.10 (a) Predicted current waveform for phase A at rated current and 6,000rpm operating with a coil temperature of 150°C

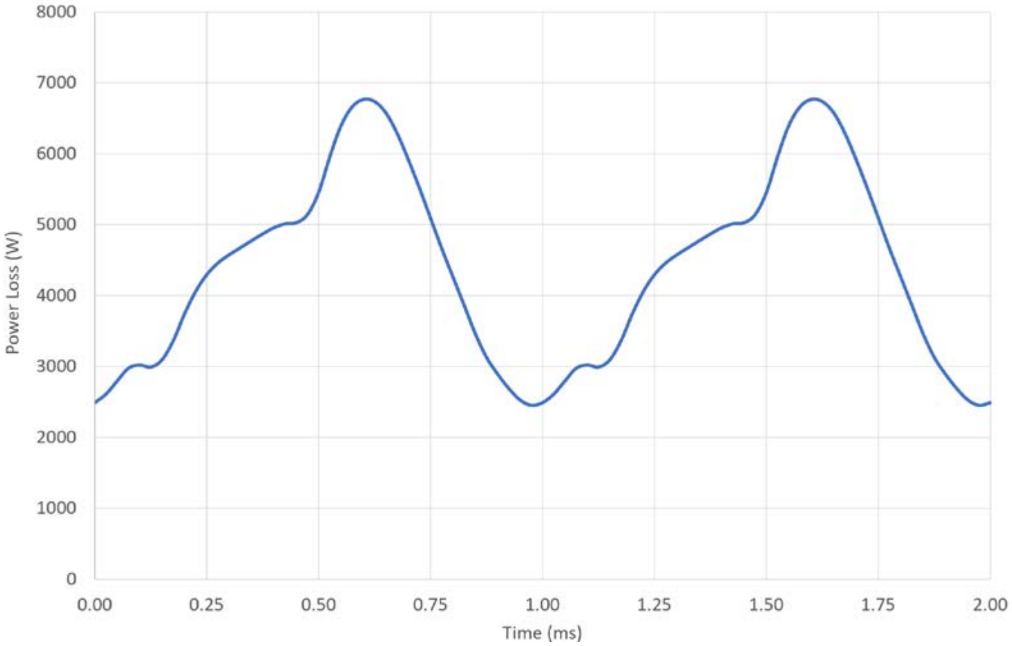

Figure 3.10 (b) Predicted conductor loss waveform for phase A at rated current and 6,000rpm operating with a coil temperature of 150°C

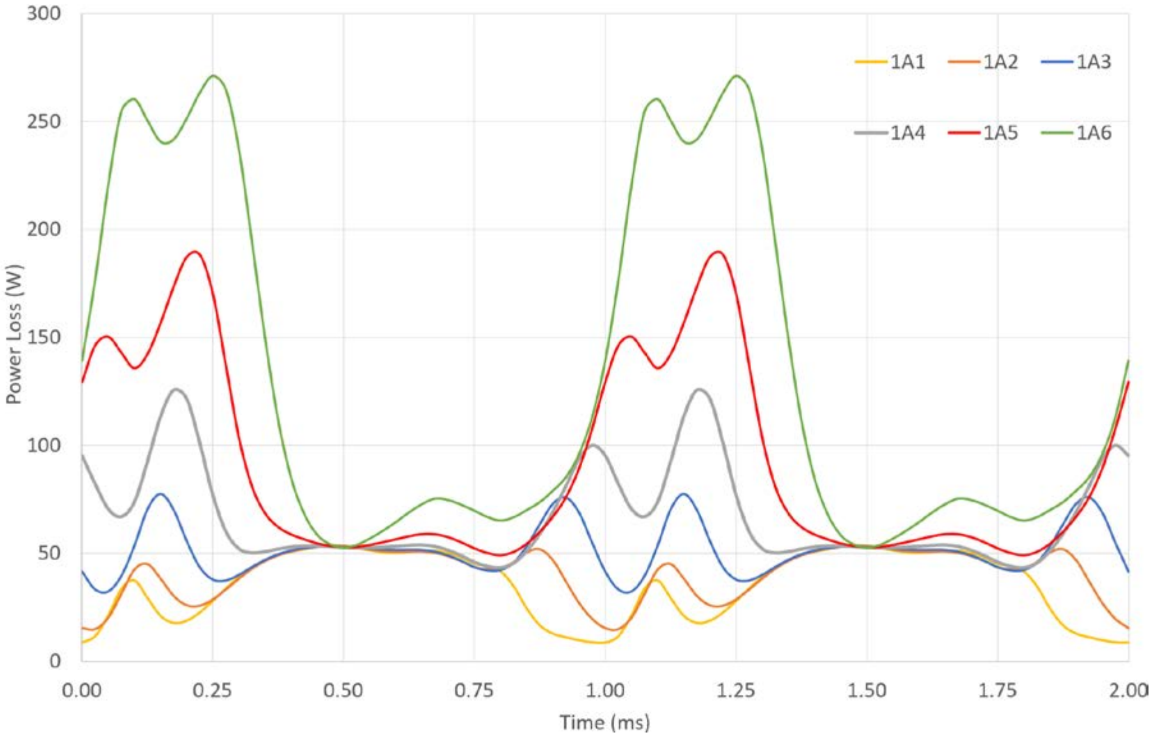

Figure 3.11 (a) Loss variation over one electrical cycle for 6 conductors adjacent to airgap in a 12-10 machine with 6x4 conductors operating in motoring mode

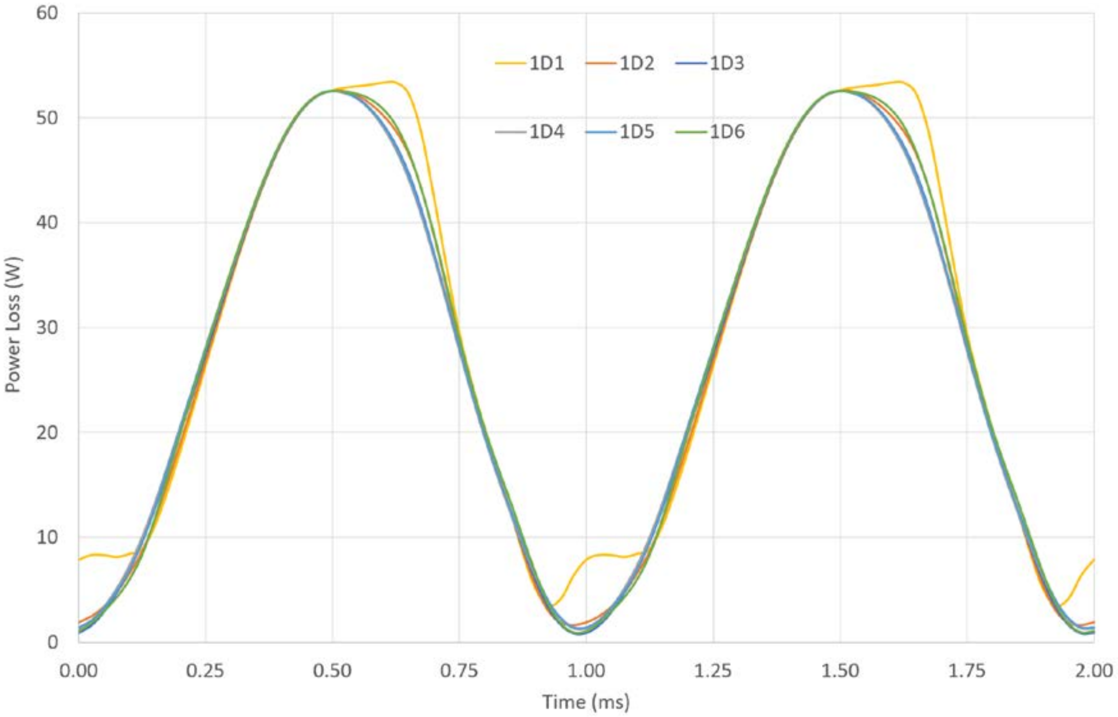

Figure 3.11 (b) Loss variation over one electrical cycle for 6 conductors at the back of the slot in a 12-10 machine with 6x4 conductors operating in motoring mode.

3.5.3 Influence of magnetic slot-wedges

One way of reducing conductor eddy current losses in permanent magnet machines is to use magnetic slot wedges. Magnetic slot wedges perform the same task of keeping the conductor in the slot but are made by mixing magnetic powder with a flexible plastic. Since magnetic slot wedges only contain 50-60% magnetic powder, the relative permeability is low and the saturation flux density is only 50-60% of that of the powder. The material used in this thesis is MW1 which was investigated in [SUN23]. Figure 3.12 shows the B-H curve for this slot material. The maximum relative permeability is only 6.5 and the material saturates at 0.98T [SUN23]. The aim of using magnetic slot wedges is to divert some of the flux in the slot opening away from the winding conductors.

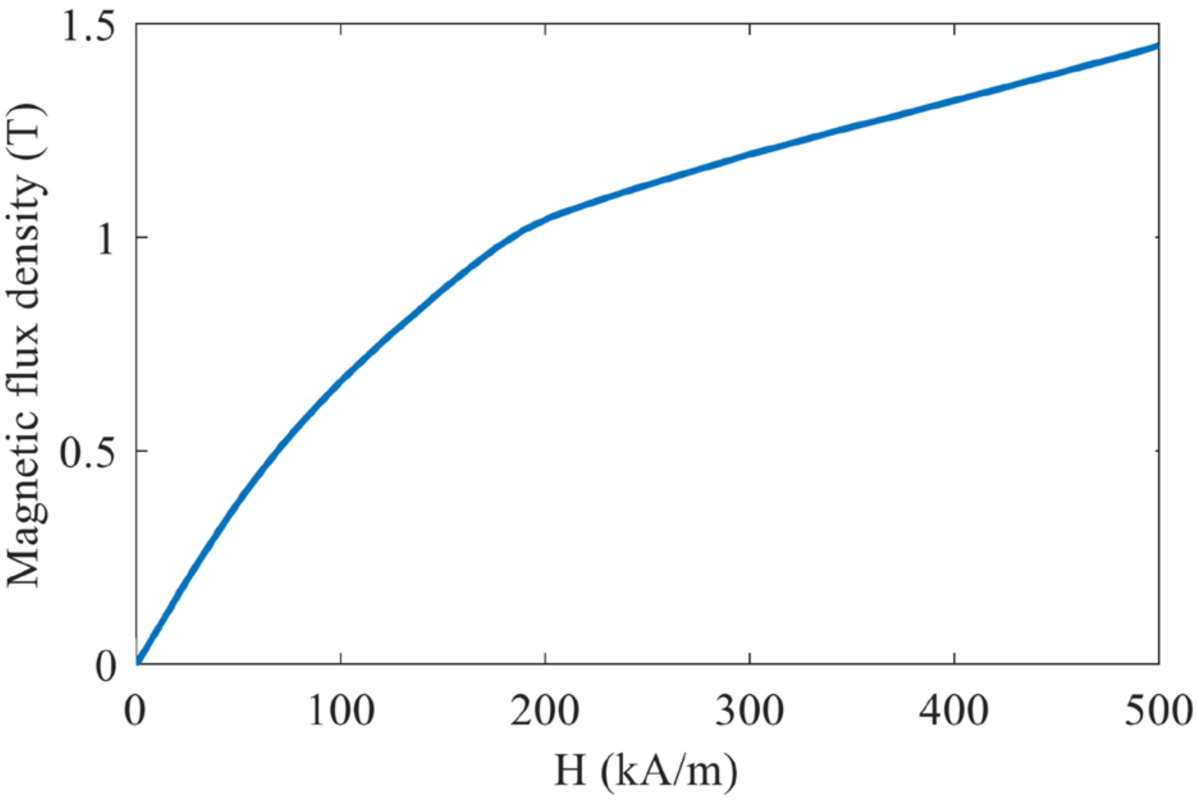

Figure 3.12 B-H curve for MW1 magnetic slot wedge material (Source: adapted from [SUN23])

The first simulation which was done was to repeat the full on-load operating conditions in the 12-slot 10 pole machine whose loss variation over one cycle was shown previously in Figure 3.10 but with the inclusion of a 1.7mm thick magnetic slot wedge in every slot. Figure 3.13 compares the variation in losses with and without a magnetic slot wedge over one electrical cycle. The average loss over one cycle with a magnetic slot wedge is 2570W compared to 2647W for no magnetic slot-wedge. As can be seen, there is only a small reduction in loss from the inclusion of magnetic slot wedges. The simulations were repeated for open-circuit rotation at 6,000rpm. Under open-circuit conditions, the only flux into the conductors is from the rotor permanent magnets and the slot wedges will be more effective in providing some screening of the conductors. The predicted variation in loss over one cycle under open-circuit conditions are shown in Figure 3.14 for machines with and without magnetic slot wedge in phase A. In this case there is a significant reduction in loss with magnetic slot wedges, with average loss over one cycle reducing from 484W to 376W.

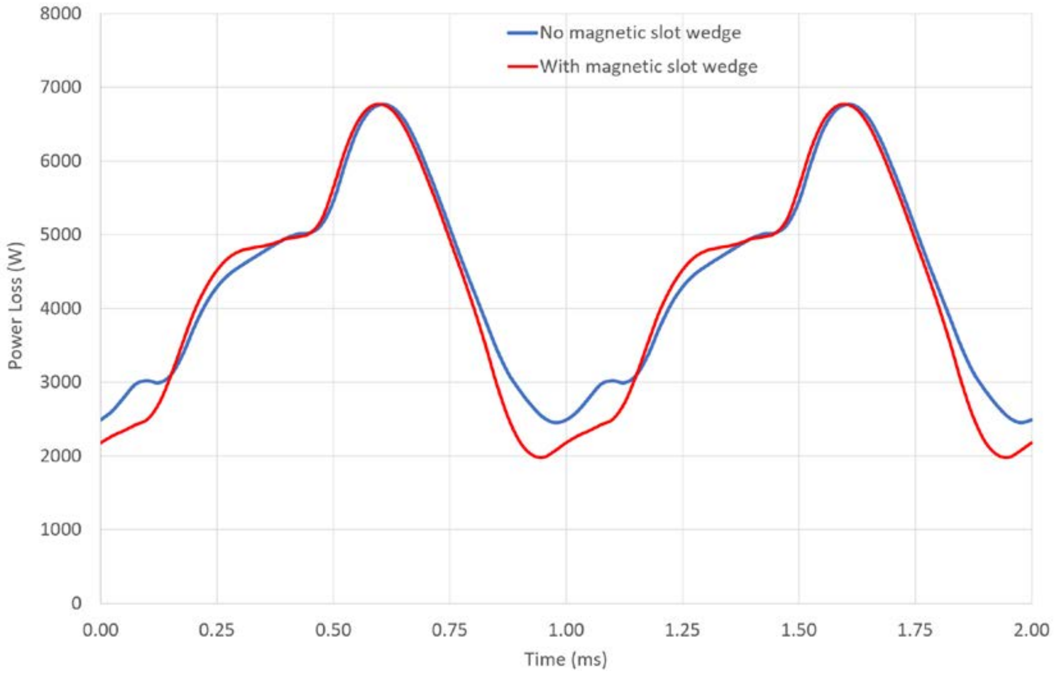

Figure 3.13 Comparison of losses with and without magnetic slot wedges

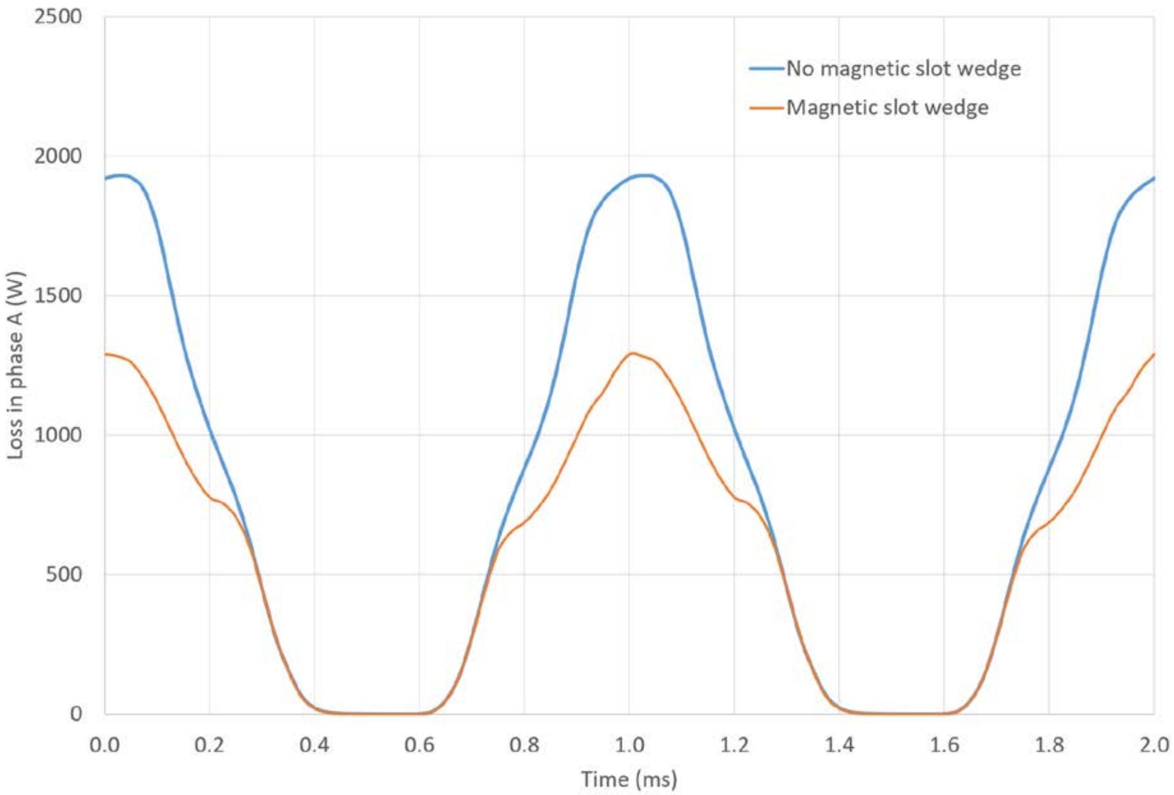

Figure 3.14 Variation in loss in phase A over one cycle under open-circuit conditions

Figure 3.15 shows a close up of field distributions in the vicinity of a slot containing phase A which demonstrates the screening effect of the magnetic slot wedge under open-circuit. However, since the relative permeability of the slot wedge is only 6.5 and the material will saturate at ~1T, this slot wedge can only provide some partial screening. The magnitude of the current density within the conductors is shown in Figure 3.16. The peak current density if there were no eddy currents present would be only 54.6A/mm^2 whereas the very localised peak current density in the front conductor at left of the slot is as high as 345A/mm^2 which shows the very high level of eddy current redistribution in the conductors near the airgap. The conductors at the back of the slot have a much more uniform current distribution.

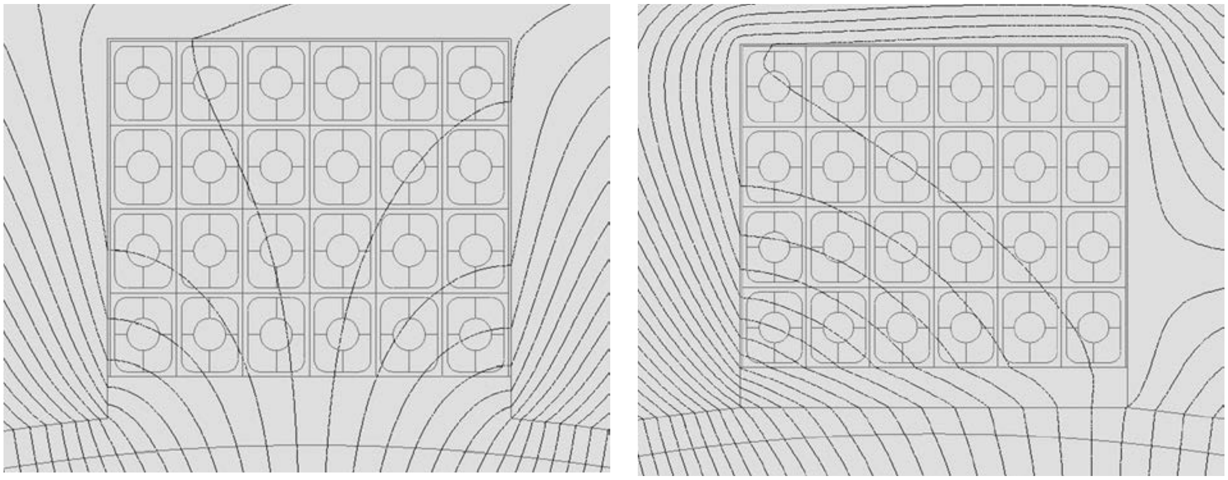

(a) Non-magnetic slot wedge (b) Magnetic slot wedge

Figure 3.15 Snapshot of field distribution near the slot opening at 1ms under open-circuit conditions

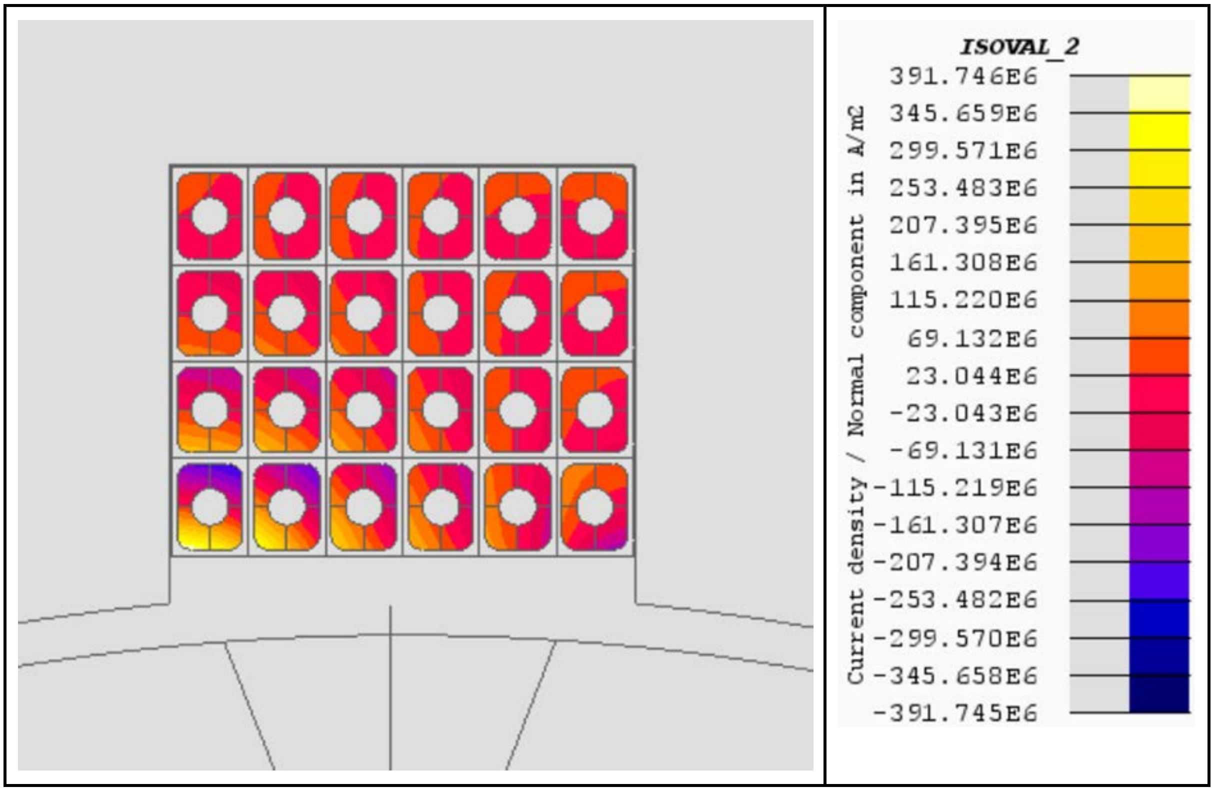

Figure 3.16 Close up of eddy current distribution in the slots of the 36 slot / 4 pole design at rated current and 6000rpm

3.6 Summary

This chapter has reported on the methods used for modelling a series of concentrated winding machine designs based on a 12 slot and 10 pole configuration. The analysis presented in this chapter has demonstrated that AC losses in the conductors is a major factor in the design and performance of hollow conductors even though the conductor cross-section only 3.0×2.3mm and the thickest region of the wall is only 0.85mm thick. A number of designs based on a 12 slot,10-pole design were modelled with the lowest level of AC loss achieved with a 3 layer winding in which the presence of different phases in the slot reduces the peak to peak change in the slot leakage field. However, even in this case the overall copper loss was still 11kW at 150°C with 36% of this coming from AC loss.

In all cases, the winding temperature did not have a major effect on the overall losses since the increased electrical resistivity although causing an increased DC loss results in a reduction in the AC loss. Although these changes do not necessarily cancel each other out, the effect of temperature is reduced compared to a winding without significant AC loss.

The benefits of magnetic slot wedges were assessed and a reduction of ~100W in ~2500W was achieved under full-load conditions for a 12-10 design with a 6×4 array of conductors. A much greater reduction in AC loss was achieved under open-circuit conditions.

A summary of the performance is shown in Figure 3.17 which shows the variation in copper loss at 150°C with power density (in all cases when meeting the rated torque of 398 Nm at 6000 rpm). As can be seen, there is reasonably consistent correlation between increasing power density and increased loss with the highest power density of 17.6 kW/kg of active mass being achieved with the single layer winding with a 10x4 conductor arrangement in each slot.

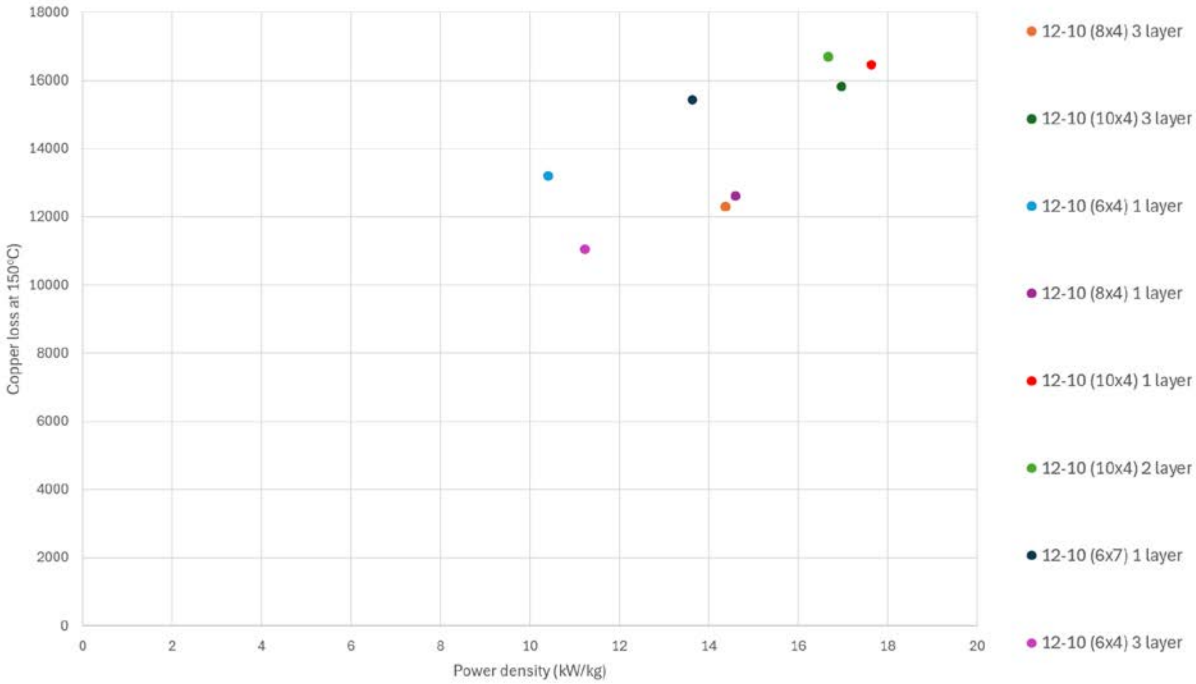

Figure 3.17 Summary of designs of concentrated designs from chapter 3

Chapter 4 - Distributed winding machines with hollow conductors

4.1 Introduction

The design studies presented in chapter 3 focused on concentrated design machines, specifically different variants of 12 slot 10 pole machines. This chapter describes a comprehensive analysis of several design variations of distributed winding machines with a view to improving on the power density of the 12-10 designs of chapter 3 and reducing the overall copper loss.

The methods used are the same as those described in chapter 3, i.e. MOTORCAD for initial sizing with analysis of performance done with a time-stepped, electrical circuit coupled finite element model which accounts for eddy current in the hollow conductors. There are several different design considerations between the distributed winding machines in this chapter and the concentrated winding machines in chapter 3. Firstly, a number of different pole numbers have been considered, and in each case, there is a need to select a back-iron thickness which is sufficient to carry the pole flux with too much saturation but does not add excessive mass. There are also a number of different winding arrangements that can be used, e.g. short-pitched coils. However, in this study, only straightforward single layer, fully-pitched coils were analysed. Another factor which would need to be taken into account in a full machine design would be the need to account for the extra end-windings of a distributed machine.

4.2 Design and analysis of a 30 slot, 10 pole machine

To provide a meaningful comparison with the 12-10 machines of chapter 3 in terms of electrical frequency, the first distributed winding machine that was modelled was a 30 slot, 10 pole machine which has the simple single-layer, fully-pitched winding shown in Figure 4.1 There is an alternative short-pitched 30 slot, 10 pole winding arrangement but this only has a winding factor of 0.866 and so was not considered further.

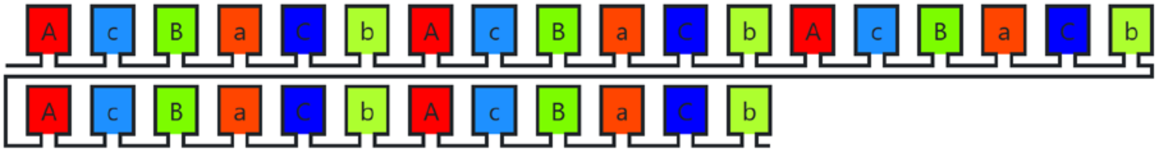

Figure 4.1 Winding layout for the 30 slot 10 pole, fully-pitched winding

Figure 4.2 shows a cross-section through the machine while Table 4.1 summarises the main dimensions and other design parameters. The machine has a 4x4 arrangement of the same hollow conductors in each slot giving a total of 480 conductors in the stator, which is the same as the 480 of the 10x4 arrangement in the 12 slot - 10 pole design modelled previously in chapter 3. As can be seen for this 30 slot machine, there is very limited scope to increase the number of conductors within each row beyond 4 in order to keep a useful width of stator tooth.

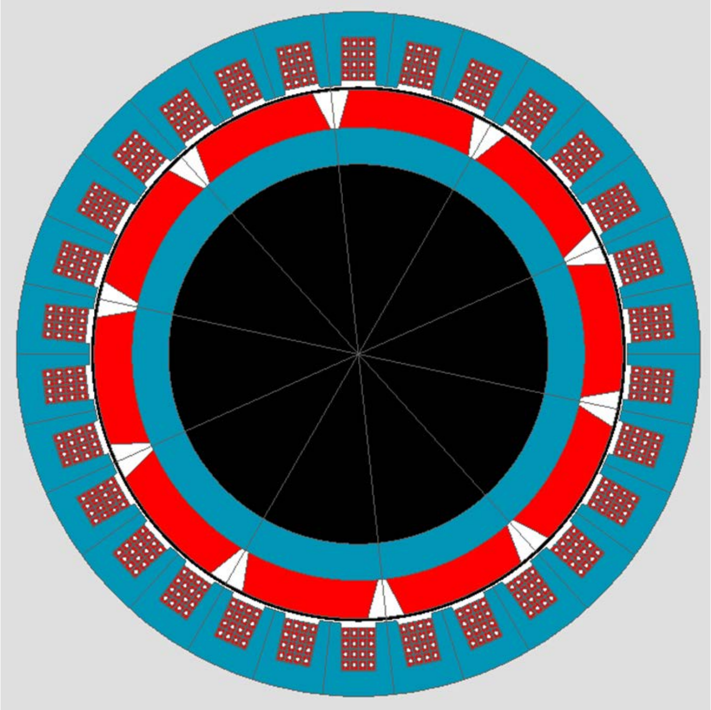

Figure 4.2 Cross-section through 30-10 design with the dimensions summarised in Table 4.1

Table 4.1 Design parameters for the 30 slot - 10 pole electrical machine.

Description	**Value**

Slot number	30
Pole number	10
Stator outer diameter	216 mm
Rotor outer diameter	169 mm (includes 2mm magnet containment)
Stator inner diameter	170 mm
Shaft diameter	120 mm
Magnet radial thickness	12 mm
Air gap length	0.5 mm
Stator slot depth	15.0mm
Slot width	11 mm
Number of conductors in in each slot	16 (4x4 array)
Total weight of active region (excl. winding)	12.05

The performance of this machine design at 6,000rpm when operating with an rms current density of 38.6A/mm^2 was predicted using the circuit coupled transient finite element simulation method discussed in chapter 2. The predicted performance of this machine is summarised in Table 4.3. It is interesting to compare the copper loss with the 12 slot 10 pole machine with a single-layer 10x4 array of conductors per slot (design 6 in Table 3.4 of Chapter 3) as both of these machines have 480 conductors and are both operating at 38.6A/mm^2. The 30-10 machine with the distributed winding needs an axial length of 73.2mm to produce the rated torque of 398 Nm while the 12-10 (design number 6) needs an axial length of 86.8mm. The total copper loss in the 30-10 machine is 11,459W at 20°C and 12,010W at 150°C. This compares with 16,920 W at 20°C and 16,464 at 150°C for the 12-10 machines. The losses for the 12-10 design are 148% and 137% of the losses for the 30-10 at 20°C and 150°C respectively. Part of this difference is due to the longer length of the active region in 12-10 which would alone result in an increase of 119%. It is also important to stress that these losses are for the active region only and the concentrated winding of the 12-10 design would have a lower end-winding length and hence loss compared to the 30-10 distributed end-winding.

Table 4.2 Predicted performance of the 30-10 design at 6000rpm when operating with an rms current density of 38.6A/mm^2

	Value for 30-10 design
Axial length to produce rated torque of 398Nm	73.2 mm

Finite element predicted copper loss at 20°C (W)	11,459
Calculated DC copper loss at 20°C (W)	4,989
Inferred AC copper loss at 20°C* (W)	6,470
Finite element predicted copper loss at 150°C (W)	12,010
Calculated DC copper loss at 150°C	7,538
Inferred AC copper loss at 150°C* (W)	4,472
Total active mass (kg) - excluding end-winding	12.05
Torque density (Nm/kg)	33.0
Power density (kW/kg)	20.8

*Inferred AC copper loss - Calculated by subtracting analytically calculated DC loss from the finite element predicted conductor loss

This 30-10 design achieves a higher power density than the 12-10 designs. In order to establish the torque capability of the 30-10, the performance of the 30-10 design was evaluated over an extended current density range up to 60A/mm^2 in motoring mode and at a stator winding temperature of 20°C. Figure 4.3 (a) and (b) shows the predicted variation in the torque and total copper loss for the 30-10 machine as a function of current density.

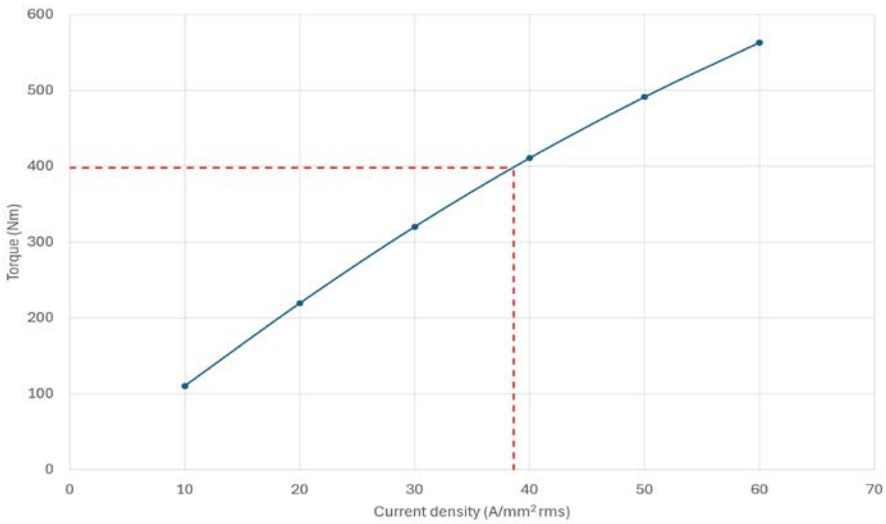

Figure 4.3 (a) Variation in average torque with current density for the 30 slot - 10 pole design (rated operating point of 398Nm shown as dashed red lines)

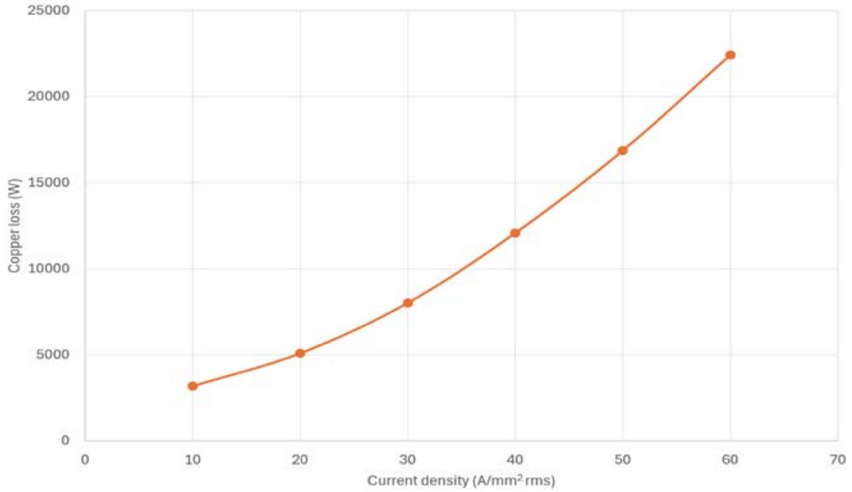

Figure 4.3 (b) Variation in copper loss with current density for the 30 slot - 10 pole design

It is notable that the torque versus current density characteristic remains reasonably linear over this range with only a small reduction in the torque per amp constant even at 60A/mm^2. It is interesting to note that for the same 16,920W loss at 20°C predicted for design 6 of the 12-10 machines, the 30-10 machine design could achieve a torque of ~490Nm. Figure 4.4 shows the flux density in this machine at the same rotor position for a series of different current densities.

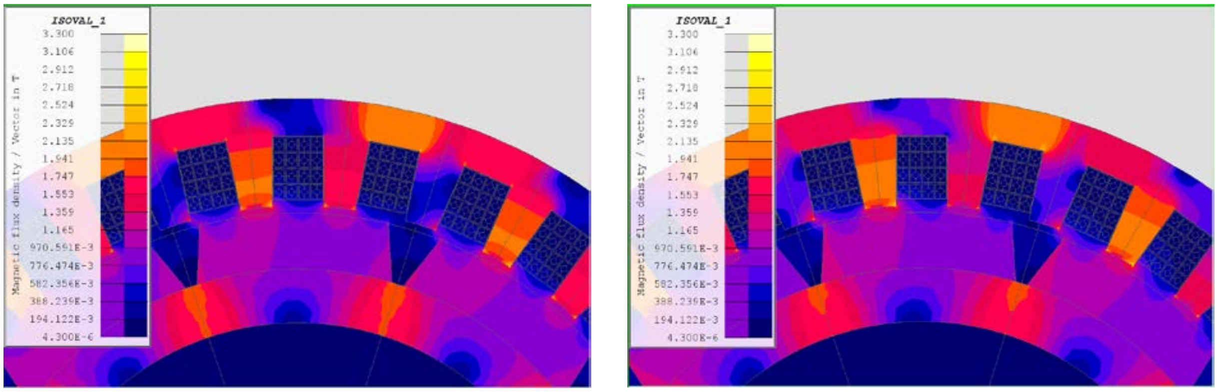

(a) 10 A/mm^2 rms

(b) 20 A/mm^2 rms

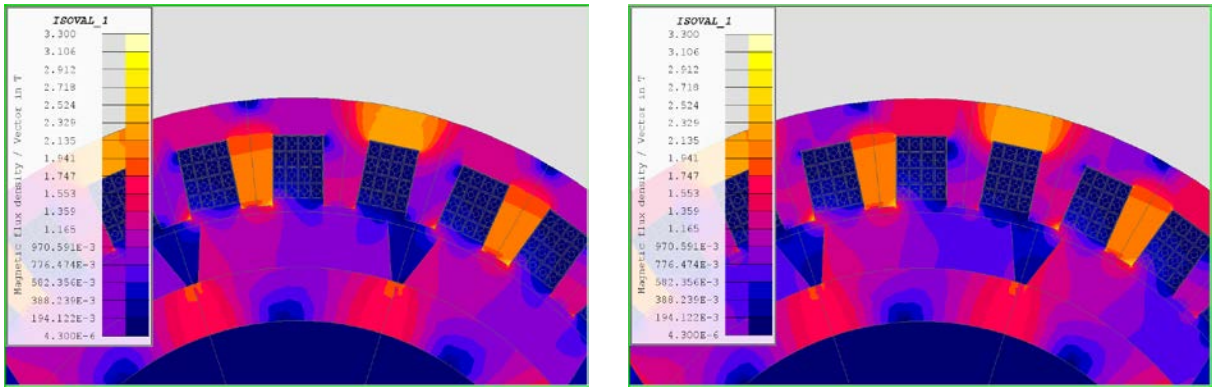

(c) 30 A/mm^2 rms (d) 40 A/mm^2 rms

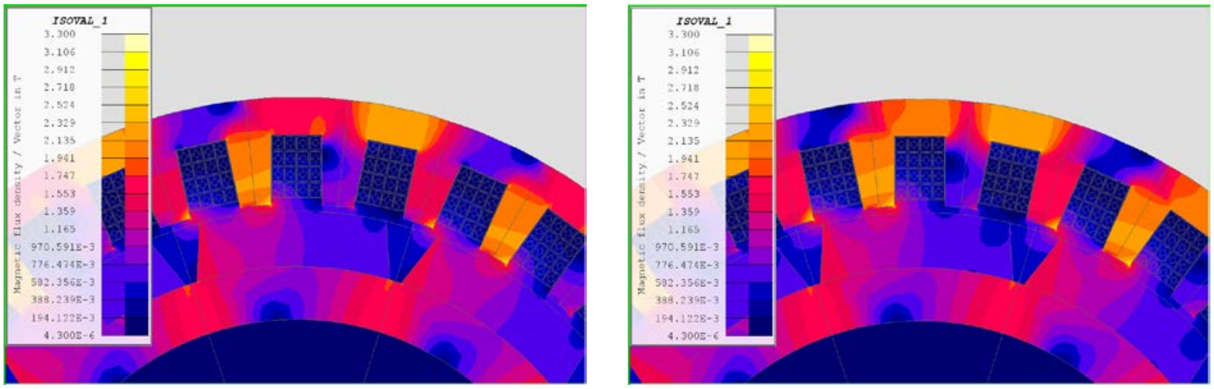

(e) 50 A/mm^2 rms (f) 60 A/mm^2 rms

Figure 4.4 Flux density distributions at a time instant that corresponds to the the peak of the current in phase A (all colour shading is on the same scale with a maximum corresponding to 3.30T)

As can be seen there is a degree of magnetic saturation in the back-iron even under open-circuit conditions. Despite the high power density of the 30-10 design, it can be seen from Table 4.2, that at 150°C, the AC component of the copper loss is still ~35% of the overall copper loss and since this is frequency dependent the benefits of reducing the rotor pole number was investigated. A lower pole number option is a 36 slot machine with a 6 pole rotor which also has a slightly higher winding factor than the 30 slot, 10 pole design.

4.3 Design and analysis of a 36 slot, 6 pole machine

A cross-section through the first 36 slot, 6 pole design considered is shown in Figure 4.5 with the main dimensions summarised in Table 4.3. This machine has a 2x4 arrangement of conductors in each slot which results in a total number of conductors in the stator core of 288.

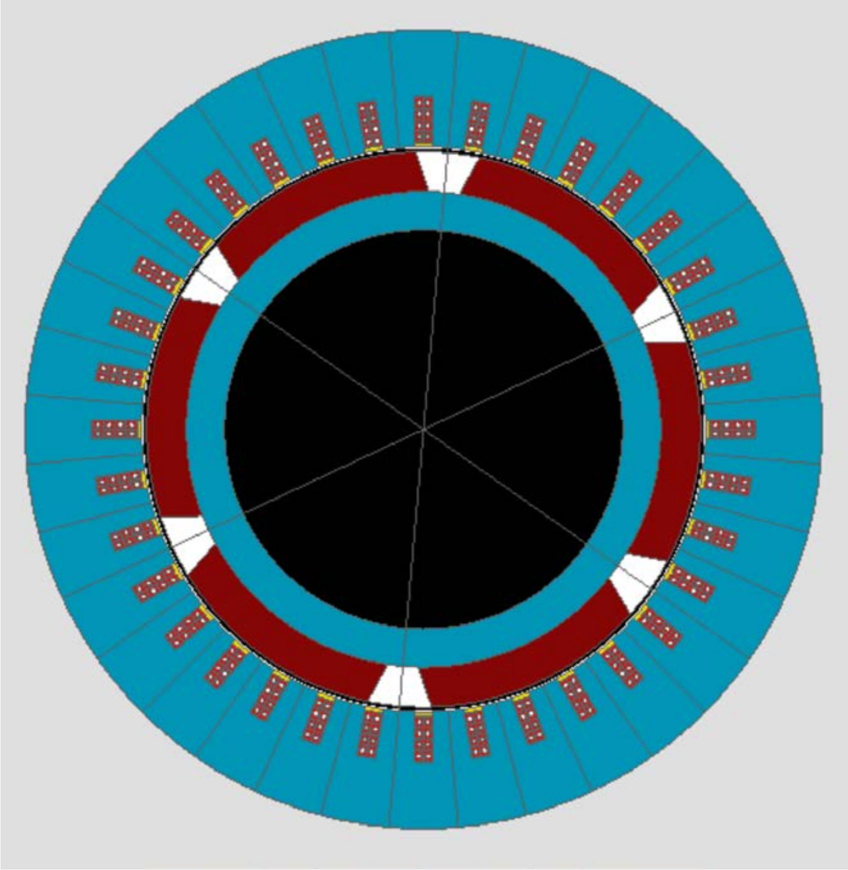

Figure 4.5 Cross-section through 36 slot - 6 pole design with 2x4 conductor arrangement in each slot

Table 4.3 Design parameters for the 36 slot - 6 pole electrical machine.

Description	**Value**
Slot number	36
Pole number	6
Stator outer diameter	240 mm
Rotor outer diameter	169 mm (includes 2mm containment)
Stator inner diameter	170 mm
Shaft diameter	120 mm
Magnet radial thickness	12 mm
Air gap length	0.5 mm
Stator slot depth	15.0 mm
Stator slot width	5.6 mm
Number of conductors in in each slot	8 (2x4 array)
Weight of active region (excl. winding)	17.42 kg

This machine was simulated using the same time-stepped, circuit-coupled finite element simulations as the other designs in this chapter. The predicted performance for this 36-6 design is summarised in Table 4.4 while Figure 4.6 shows the flux density distribution in the machine. The axial length required to produce 398Nm is 111.6mm. This is significantly higher than the 30-10 design and is due largely to the fact that the 36-6 design only has a total of 288 conductors in the stator, i.e. 36 slots with 8 conductors per slot, while the 30-10 design has 480 conductors.

Table 4.4 Predicted performance of the 36-6 design with 2x4 conductors per slot at 6,000rpm when operating with an rms current density of 38.6A/mm^2

Description	**Value for 36-6 design**
Axial length to produce rated torque of 398Nm (mm)	111.6
Finite element predicted copper loss at 20°C (W)	6054
Calculated DC copper loss at 20°C (W)	4567
Inferred AC copper loss at 20°C* (W)	1487
Finite element predicted copper loss at 150°C (W)	8173
Calculated DC copper loss at 150°C	6903
Inferred AC copper loss at 150°C* (W)	1270
Total active mass (kg) - excluding end-winding	26.36
Torque density (Nm/kg)	15.1
Power density (kW/kg)	9.49

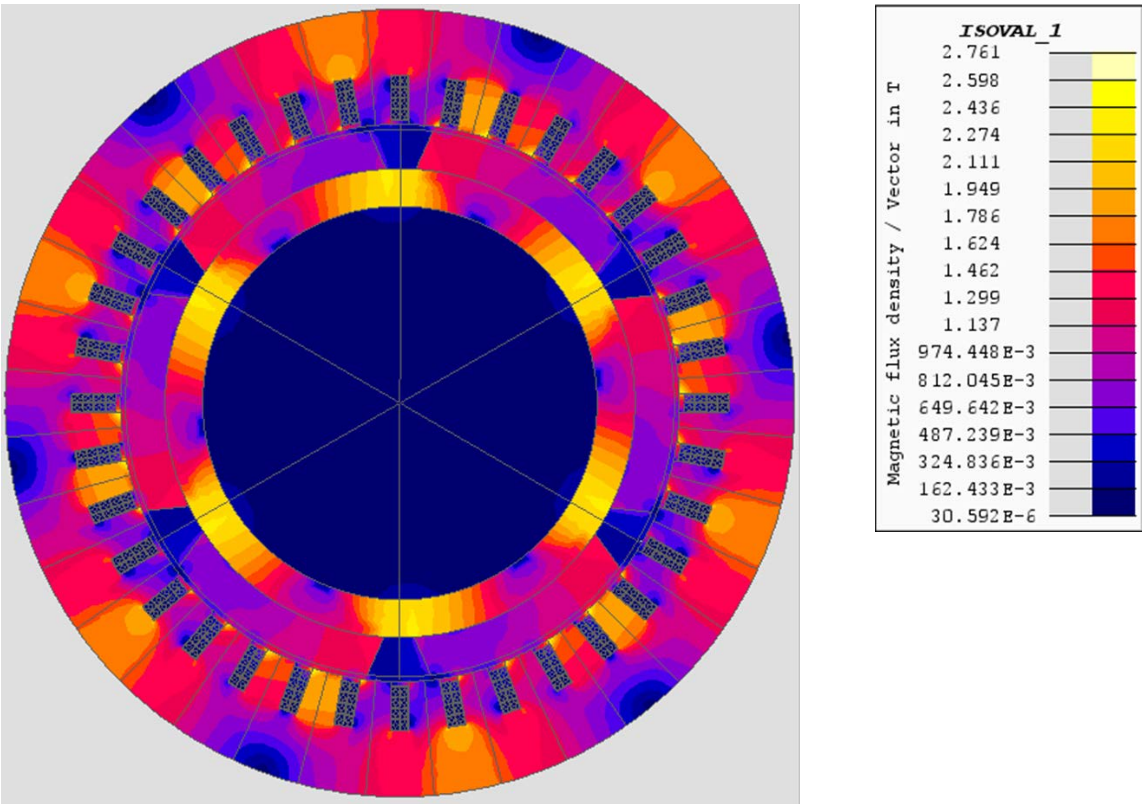

Figure 4.6 Flux density distribution for the 36 slot 6 pole design operating in motoring mode and rated torque of 398Nm (stator outer diameter of 240mm)

In order to increase the number of conductors in the 36 slot, 6 pole design the slot depth was increased to 25.4mm in order to increase the number of turns per slot to 14 (arranged as 2x7). This brings the 36-6 design up to a total of 504 conductors which is slightly higher than the 480 of the 30-10 design but is the nearest that can be achieved with 36 slots and an even number of conductors per slot. The back-iron was kept at the same thickness as the 2x4 conductor design and so the increase in the slot depth to 25.4mm leads to a new stator outer diameter of 262mm. Figure 4.7 shows a cross-section through this machine with 14 conductors per slot.

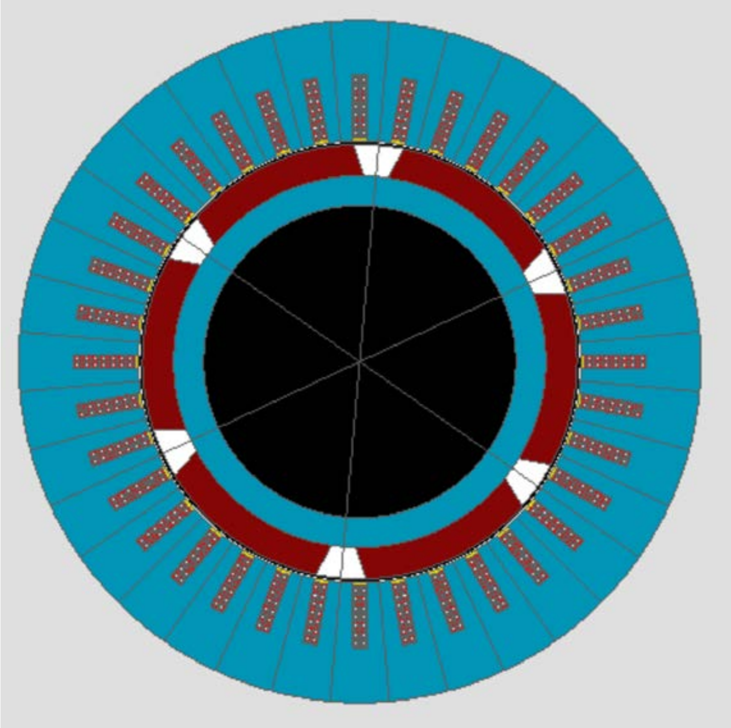

Figure 4.7 Cross-section through the 36 slot, 6 pole design with 2x7 conductors in each slot

The performance of this machine in motoring mode when operating at the same rms current density of 38.6 A/mm^2 rms is summarised in Table 4.5. The torque capability of this machine is high resulting in an axial length of only 68.3mm to produce the rated torque of 398mm. The overall mass of this machine is 20.25kg compared to the 26.36kg for the 36-6 machine with 2x4 conductors.

As would be expected, with 175% of the number of conductors in the machine operating at the same rms current density the copper losses in the 2x7 design are much higher than the 2x4 design of the same pole number

Overall, this means that the incorporation of more conductors into the 36-6 design by increasing the slot depth does not result in any significant improvement in the power density but does lead to a very significant increase in the overall copper loss.

Table 4.5 Predicted performance of the 36-6 design with 2x7 conductors per slot at 6000rpm when operating with a rms current density of 38.6A/mm^2

Description	**Value for 36-6 design (2x7)**
Axial length to produce rated torque of 398Nm	68.3
Finite element predicted copper loss at 20°C (W)	8910
Calculated DC copper loss at 20°C (W)	4983
Inferred AC copper loss at 20°C* (W)	4017
Finite element predicted copper loss at 150°C (W)	9435
Calculated DC copper loss at 150°C	7529
Inferred AC copper loss at 150°C* (W)	1906
Total active mass (kg) - excluding end-winding	20.25
Torque density (Nm/kg)	19.7
Power density (kW/kg)	12.35

A large part of the mass penalty for the 2x7 conductors is the decision to maintain the same back-iron thickness as the 2x4 design. This is an entirely reasonable assumption since the flux per pole is likely to be at least as high as the 2x4 design and probably higher given the greater slot mmf. However, in order to explore whether there is some potential to decrease the back-iron thickness without affecting the torque capability disproportionality and so improve the torque density, one further model was considered with a 250mm stator outer diameter. This design required an axial length of 68.3mm to produce 398Nm and had an active region mass of 20.25kg resulting in torque density of 19.7Nm/kg and hence a power density of 12.35kW/kg. There was a slight change in copper loss due to the effect of magnetic saturation on the AC losses.

The 36 slot machine with 6 poles resulted in an overall copper loss which was 179% of the quasi-static loss at 20°C which reduced to 125% at 150°C. The most straightforward method to reduce the AC loss is to decrease the number of poles to 4 which would result in a fundamental electrical frequency of 200Hz. In general, reducing the pole number of a machine has the positive benefits of reducing the electrical frequency and hence the stator core loss, induced eddy current magnet loss and AC conductor losses. However, it does have the drawback of increasing the stator and rotor back-iron thicknesses needed to deal with the higher flux per pole.

4.4 Design and analysis of a 36 slot, 4 pole machine

The first case considered maintained the same stator outer diameter at 240mm as the 6 pole design but increased the rotor back iron thickness by modifying the shaft diameter. This does result in a small increase in the mass of the active region although whether this results in an overall increase in total machine mass depends on the material used for the rotor mechanical hub. The stator core cross-section and arrangement of conductors in each individual slot was maintained as a 2×4 array but the coils from the different slots were connected to produce a 4 pole winding. Figure 4.8 shows the winding diagram for the 36 slot and 4 pole winding. This winding has a fundamental winding factor of 0.96.

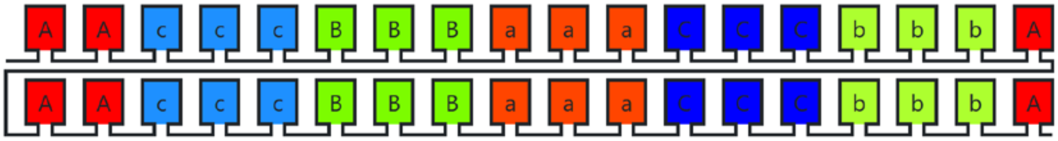

Figure 4.8 Winding diagram for 36 slot, 4 pole winding

This machine requires a stator core axial length of 124.0 mm to achieve the rated torque of 398Nm compared to 111.6mm for the 36-6 design. Table 4.6 summarises the finite element predicted performance of this 4 pole machine alongside the 6 pole baseline when operating at the same current density of 38.6A/mm^2 rms. In both cases, the results are shown for motoring mode.

Table 4.6 Finite element predicted performance for a 36-4 design (stator outer diameter of 240mm and 2x4 conductors per slot)

Description	**Value for 36-4 design**
Axial length required to produce rated motoring torque of 398Nm (mm)	124.0
Finite element predicted copper loss at 20°C (W)	6927
Calculated DC copper loss at 20°C (W)	5077
Inferred AC copper loss at 20°C* (W)	1849
Finite element predicted copper loss at 150°C (W)	8923
Calculated DC sopper loss at 150°C	7671
Inferred AC copper loss at 150°C* (W)	1252
Total active mass (kg) - excluding end-winding	34.15
Torque density (Nm/kg)	11.65
Power density (kW/kg)	7.32

*Inferred AC copper loss - Calculated by subtracting analytically calculated DC loss from the finite element predicted conductor loss

However, the torque density of this 4 pole design is lower than the corresponding 36-6 machine with the same stator core. Some of this is a consequence of the lower winding factor (~4%) but retaining the same back-iron thickness while dropping the pole number from 6 to 4 increases the flux density in the back-iron which could cause excessive saturation and hence a reduction in torque per amp capability. Figure 4.9 shows the finite element predicted flux density distribution in the 36-4 machine with the same 240mm diameter as the 36-6 in which it can be seen that the regions of the back iron is heavily saturated at this particular rotor position with flux densities of ~2T in this NO20 Silicon iron.

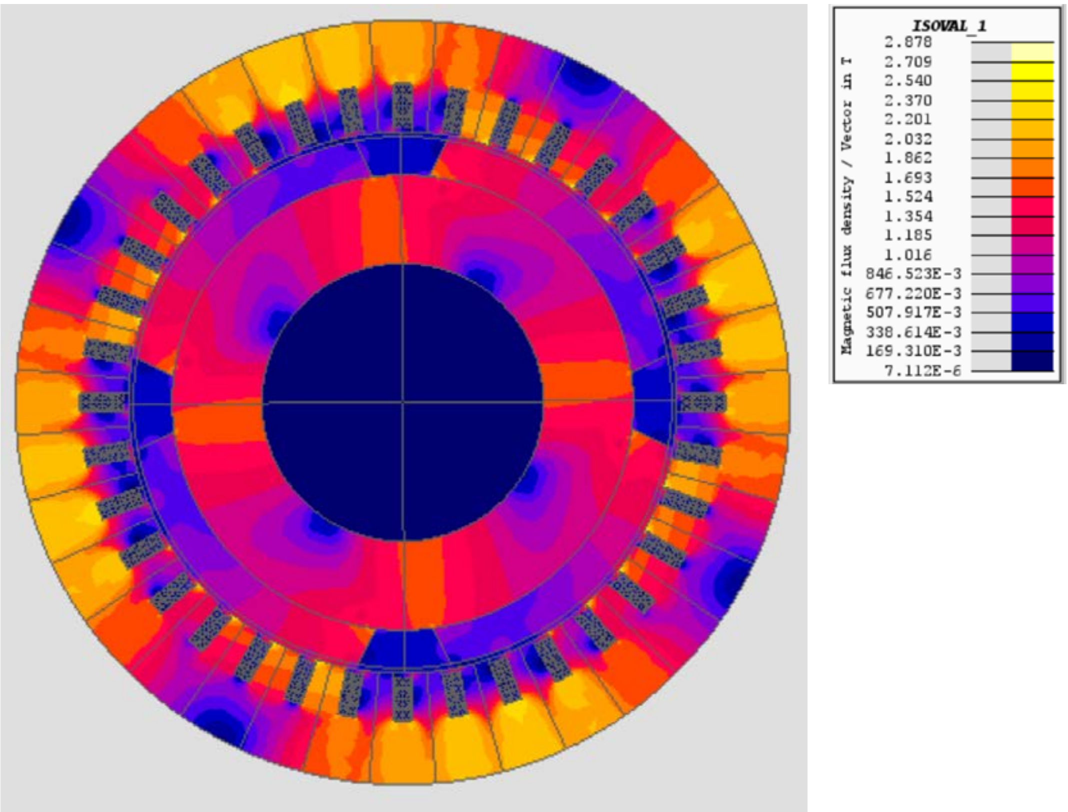

Figure 4.9 Flux density distribution for the 36 slot 4 pole design operating in motoring mode and rated torque of 398Nm (stator outer diameter of 240mm)

In order to reduce the level of saturation and improve the torque capability, the stator outer diameter was increased from 240mm to 250mm. As expected, reducing the levels of saturation resulted in a reduced stator core axial length required to achieve the rated torque of 398Nm from 124.0mm to 110.3mm. The flux density distribution for this design with a larger 250mm stator outer diameter is shown in Figure 4.10. As can be seen, although there is some reduction in the flux density in the back-iron the machine is still very saturated.

To try to improve the torque capability of this 36-4 machine, the stator outer diameter was further increased to 260mm. Again, this resulted in a reduction in the axial length need to produce 398Nm to 104.4m. A summary of the performance of a 36 slot 4 pole design which are the same except for the stator core outer diameters is shown in Table 4.7.

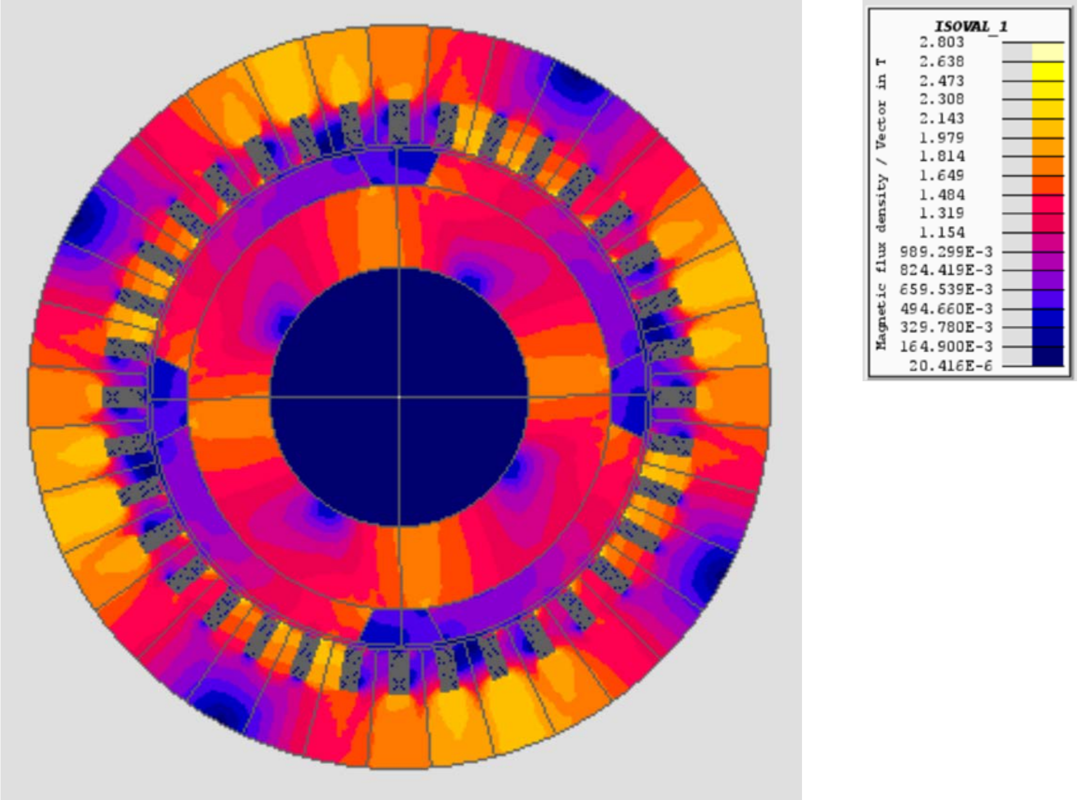

Figure 4.10 Flux density distribution for the 36 slot 4 pole design operating in motoring mode and rated torque of 398Nm (stator outer diameter of 250mm)

Table 4.7 Summary of the performance of a 36-4 design with 2x4 arrangement of conductors per slot for a range of different stator outer diameters

Description	**240mm**	**250mm**	**260mm**
Axial length to produce rated motoring torque of 398Nm	124.0	110.3	104.4
Finite element predicted copper loss at 20°C (W)	6927	5495	5002
Calculated DC copper loss at 20°C (W)	5077	4515	4274
Inferred AC copper loss at 20°C* (W)	1849	980	728
Finite element predicted copper loss at 150°C (W)	8923	7485	6946
Calculated DC copper loss at 150°C	7671	6823	6458
Inferred AC copper loss at 150°C* (W)	1252	662	448
Total active mass (kg) - excluding end-winding	34.15	33.63	35.03
Torque density (Nm/kg)	11.65	11.83	11.36
Power density (kW/kg)	7.32	7.44	7.14

4.5 Increasing the number of conductors per slot in 36 slot-4 pole design

The highest torque densities achieved up to this point for both concentrated and distributed windings were obtained with a total of 480 conductors in the stator, i.e. 10x4 in 12 slots and 4x4 in 30 slots. However, this also resulted in a significant increase in overall loss at the rated current density. In order to get a 36 slot, 4 pole design with an increased number of conductors, the conductor arrangement in each slot was changed to a 3×4 array as shown in Figure 4.11. This particular design has a total of 432 conductors and the same outer diameter of 240mm. As can be seen from the small size of the remaining tooth with this 3×4 arrangement, the next step of a 4×4 arrangement could not be fitted into a 36 slot stator core with a practical tooth.

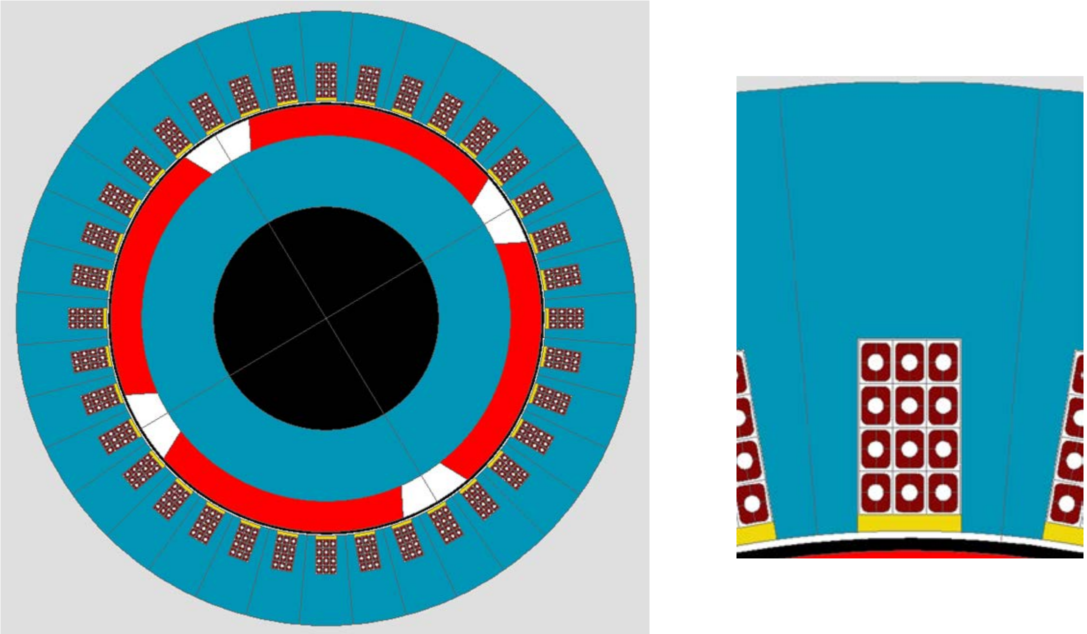

Figure 4.11 36 slot, 4 pole machine with a 3×4 array of conductors in each slot

The predicted performance for a 36-4 machine with 12 conductors per slot in a 3×4 and a stator outer diameter of 240mm was simulated using a time-stepped, transient finite element model. Increasing the number of conductors per slot from 8 to 12 with the same stator outer diameter of 240mm results in an increase in torque per unit axial length from 3210 Nm/m to 4285 Nm/m respectively. This means that the axial length required to meet the 398Nm torque specification reduces from 124.0mm to 92.9mm. The 33% increase in torque per unit axial length is lower than the 50% increase in the number of conductors. Some of this is due to the narrower teeth which means that the torque will not scale simply with the number of conductors because less flux is captured by the narrower teeth. However, magnetic saturation, which was already a problem in the 240mm design with 8 conductors, is having a significant limiting effect on the torque capability. This is demonstrated in the finite element predicted flux density distribution in Figure 4.12 which shows a high level of magnetic saturation in this NO20 Silicon iron core for the design with a stator outer diameter of 240mm.

To improve the torque capability, the stator outer diameter was increased, first to 250mm and then to 260mm. A summary of the performance for the 240, 250 and 260mm outer diameter designs is shown in Table 4.8, while Figure 13 shows the flux density distribution in the 260mm stator outer diameter design which as expected, has a lower level of flux density and hence magnetic saturation.

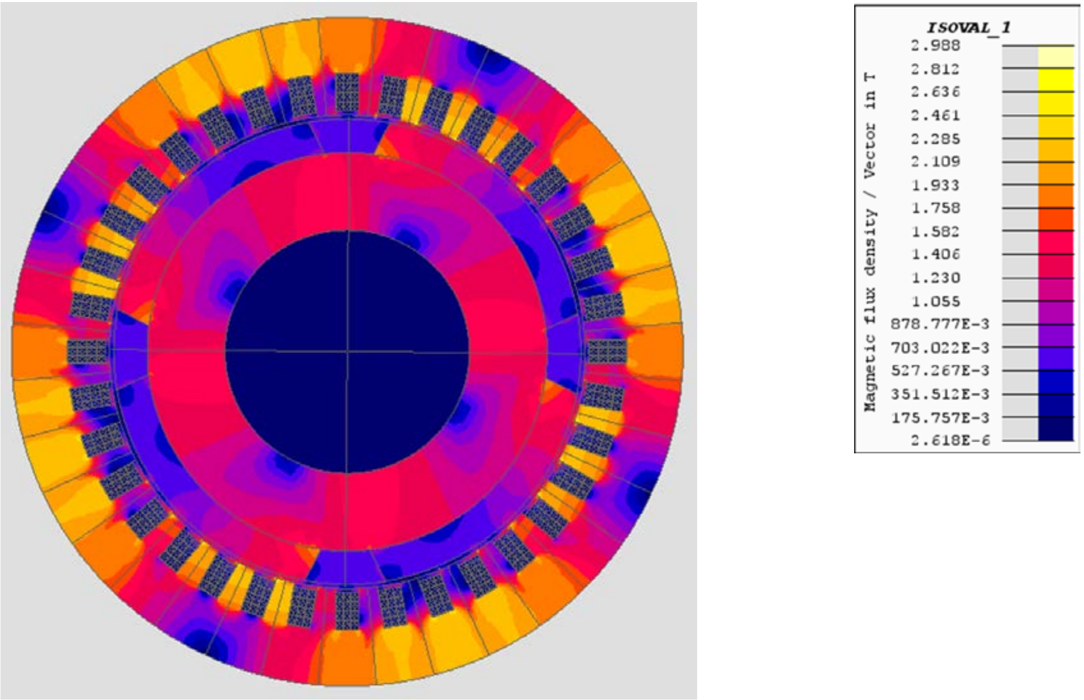

Figure 4.12 Flux density distribution for the 36 slot 4 pole design with 12 conductor per slot (3×4) operating in motoring mode and rated torque of 398Nm (stator outer diameter of 240mm)

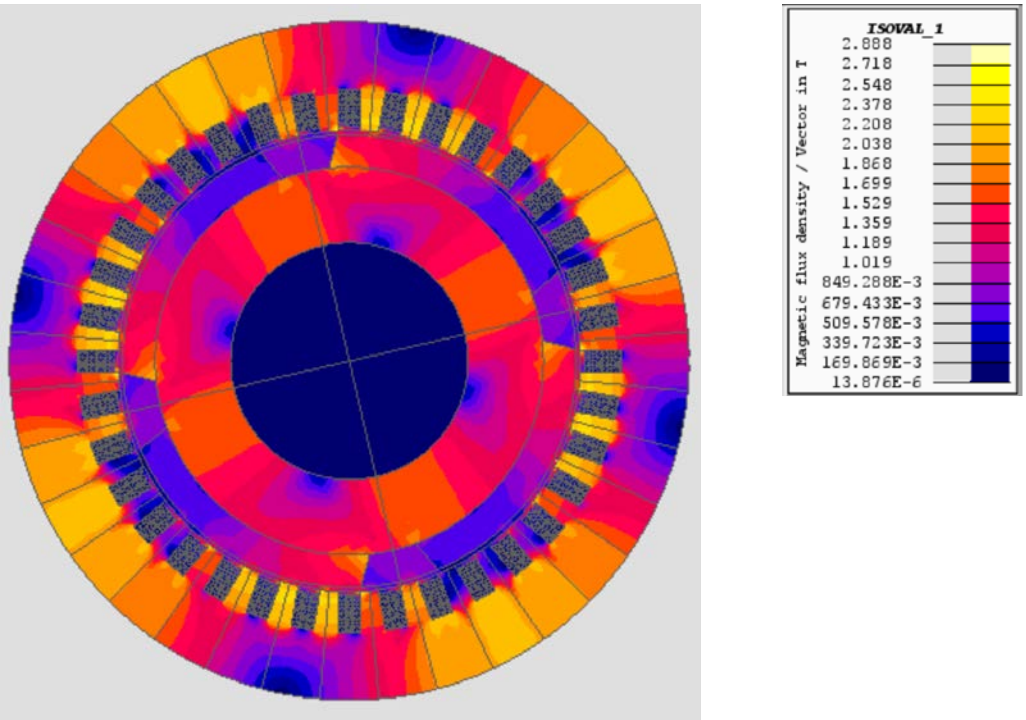

Figure 4.13 Flux density distribution for the 36 slot 4 pole design with 12 conductor per slot (3×4) operating in motoring mode and rated torque of 398Nm (stator outer diameter of 250mm)

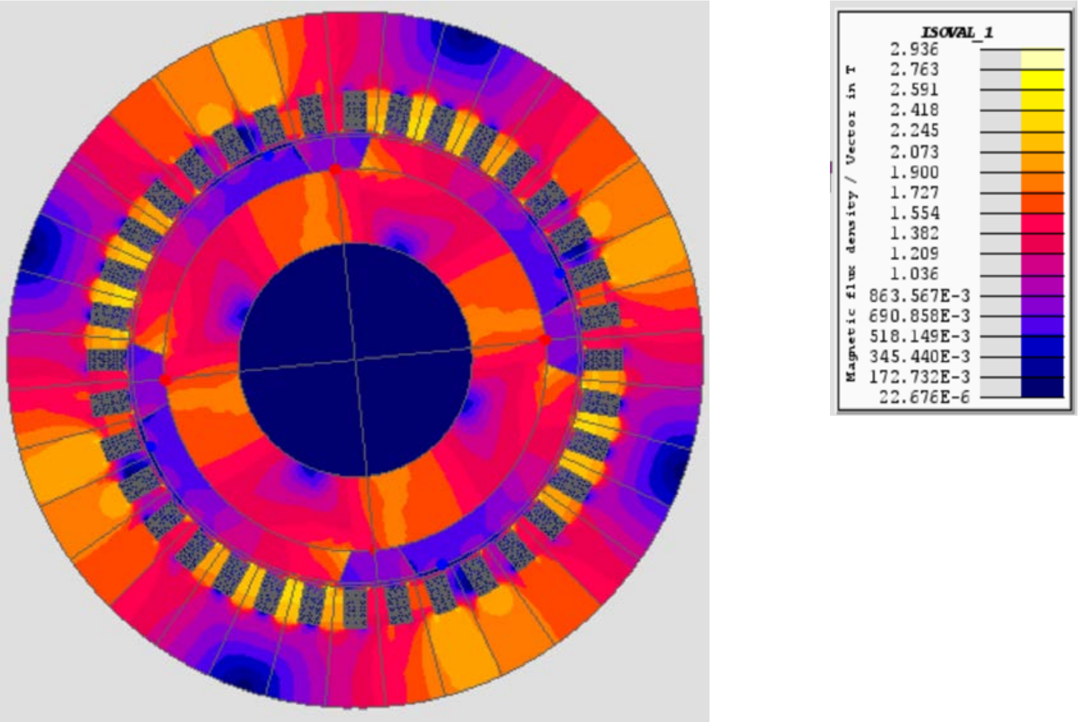

Figure 4.14 Flux density distribution for the 36 slot 4 pole design with 12 conductor per slot (3×4) operating in motoring mode and rated torque of 398Nm (stator outer diameter of 260mm)

Table 4.8 Performance summary in motoring mode for a series of 36 slot, 4 pole machines with different stator outer diameters and a 3×4 array of conductors in slot

Description	**240mm**	**250mm**	**260mm**
Axial length to produce 398Nm	92.9	81.8	76.9
Predicted copper loss at 20°C (W)	8014	6668	6191
Calculated DC copper loss at 20°C (W)	5703	5021	4721
Inferred AC copper loss at 20°C* (W)	2311	1647	1470
Predicted copper loss at 150°C (W)	10,203	8416	8134
Calculated DC copper loss at 150°C	8618	7588	7113
Inferred AC copper loss at 150°C* (W)	1585	828	1021
Total active mass (kg) - excl.end-winding	25.18	25.48	25.47
Torque density (Nm/kg)	15.8	15.6	15.6
Power density (kW/kg)	9.93	9.82	9.82

As can be seen, the increase in the stator outer diameter which only increases the back-iron thickness and does not affect the slot or the rotor leads to an increase in torque capability and so a reduction in the axial length required to meet the torque specification of 398Nm. The net effect on the mass of a machine which is capable of meeting the torque specification and hence the torque and power density is small, as the reduction in length almost balances the extra weight of the thicker back-iron. However, the active region copper loss of the larger outer diameter designs is lower due to the reduced axial length and so is on balance a better design because of the very small differences in power density. However, the power density is still only ~10 kW/kg and this does not include end-windings.

One interesting issue in the results in Table 4.8 is the significant reduction in AC losses as the stator outer diameter. Some of this is a consequence of the shorter axial length of the designs with shorter axial lengths. However, the AC losses per unit axial length at 20°C (worst case AC loss) for the 240mm and 260mm designs are 24.88kW/m and 19.11kW/m. Hence, a simple increase in the back-iron, with no change to the slot or the geometry of the core near the slot, reduces the AC loss density in the conductors by 23.2%. There link between magnetic saturation in the stator core and AC loss was also observed in [SUN23] although this was in the tooth body and the back-iron. This was explained in [SUN23] as being caused by more flux crossing the slot and interacting with the conductors because of saturation in the core.

4.6 Comparison of 36-4 and 30-10 designs

The 30-10 design achieved a power density of 20.8 kW/kg (active region mass only excluding end-windings) at 6000rpm, but with a 150°C copper loss in the active region of 12.01kW, including 4.47kW of AC loss. As shown in Table 4.9, the best 36-4 design (260mm stator outer diameter) is only able to achieve just under half of this power density but with a much reduced copper loss of 8.13kW at 150°C. Figure 4.15 shows a comparison between the cross-sections of these machines to a common scale which shows the very influence of stator and rotor back-iron thickness on the overall size of the machine and hence the benefits in torque density terms of the higher pole number.

A mass breakdown for these two machine-design is shown in Table 4.9 from which it is clear that the stator core and the rotor core are the main reason for the large difference in power density. Table 4.9 summarises a comparison between some key dimensions and performance measures for these two designs.

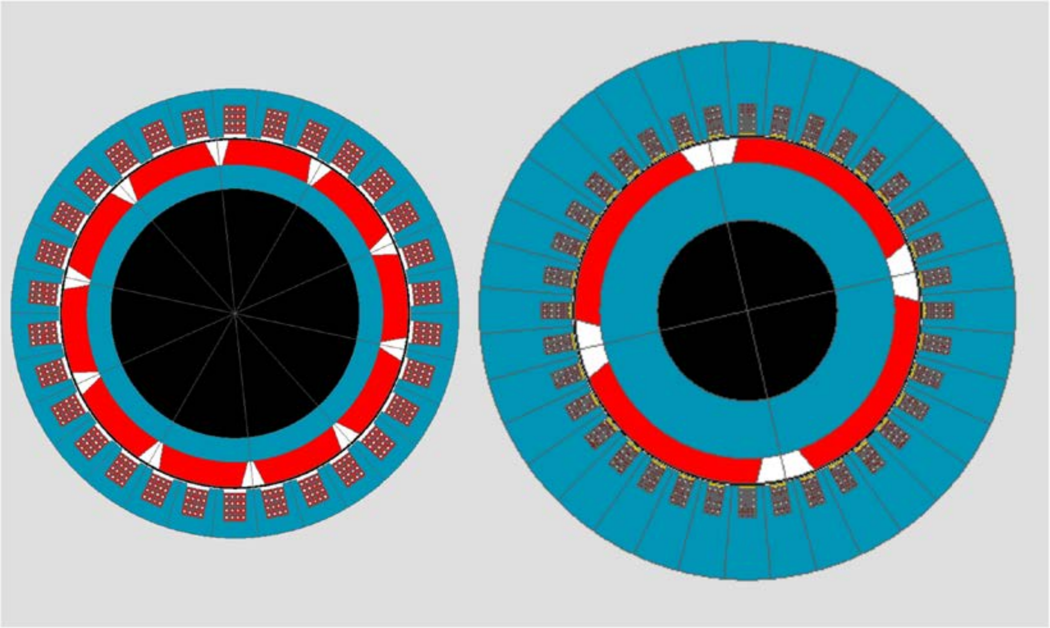

Figure 4.15 Cross-sections through 30-10 (216mm stator outer diameter) and 36-4 (260mm outer

diameter) - shown to a common scale

Table 4.9 Mass breakdown of 30-10 design and the 260mm outer diameter version of 36-4 design

Description	**30-10**	**36-4**
Stator core	5.05	15.28
Rotor core	2.66	5.91
Stator winding (excl. end-winding)	1.68	1.58
Rotor magnets	2.70	2.70
Total	12.05	24.57

Table 4.10 Comparison of dimensions and key performance measures

Description	**30-10**	**36-4**
Stator outer diameter	216mm	260mm
Total number of conductors in the stator	480	432
Axial length of core required for 398Nm	73.2mm	76.9mm
Active region mass	12.05kg	25.57kg
Power density	20.8kW/kg	9.82kW/kg
Torque density	33.0Nm/kg	15.6 Nm/kg
Copper loss at 20°C	11,459W	6191W
Copper loss at 150°C	12,010W	8134W

One further design was modelled based on a 36 slot-4 pole stator with 3x4 conductors per slot but with the stator outer diameter and the shaft diameter (which sets the rotor core inner diameter) set to the same 216mm and 120mm respectively as the 30-10 design. This will inevitably result in very high levels of magnetic saturation but provides a useful comparison in terms of cross-section. This final design option was modelled using the finite element model and required an axial length of 180.5mm to produce the rated torque of 398Nm which is ~246% of the length of the 30-10 with a very similar cross-section. As shown in the predicted flux density distribution in Figure 4.16, this machine has an extreme level of magnetic saturation with flux density approaching 2.5T in most of the back-iron. The active region mass of this new 36-4 combination with a 216mm stator diameter and a 120mm shaft diameter is 29.71kg which is ~5kg heavier than the other 36-4 designs with 3x4 conductors per slot up to an outer diameter of 260mm. The very significant reduction in torque capability shows that this design has pushed the back-iron below a practical limit.

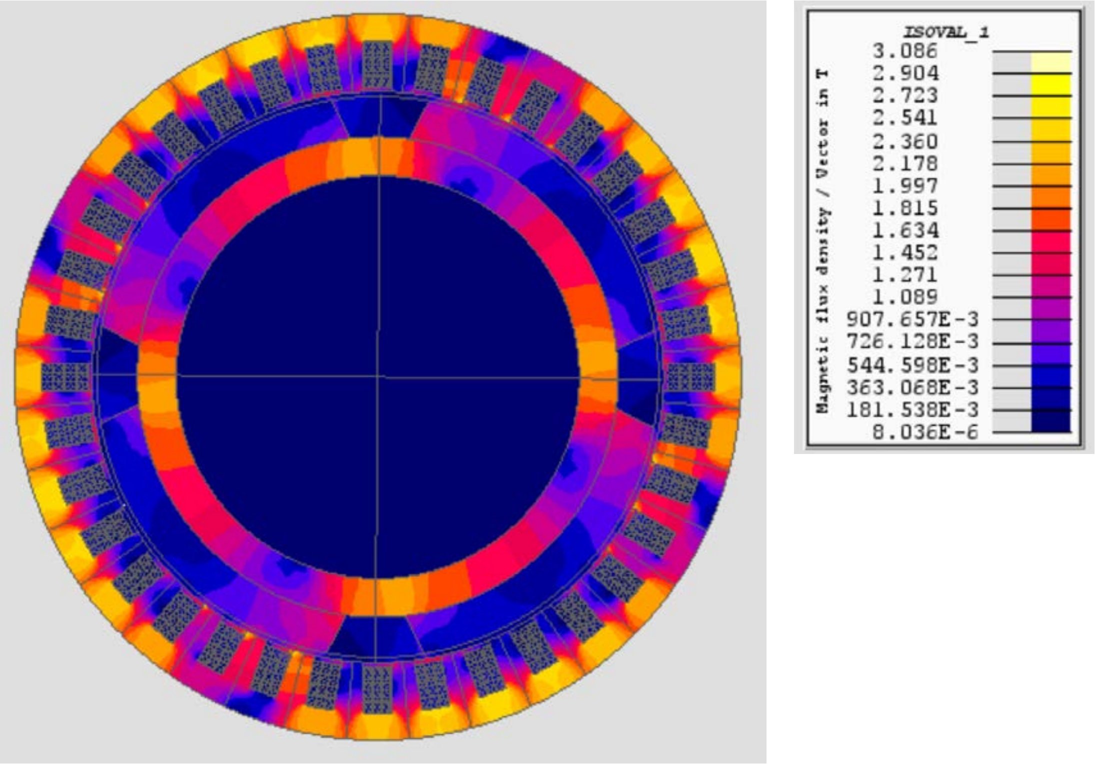

Figure 4.16 Flux density distribution for the 36 slot 4 pole design with 12 conductor per slot (3×4) operating in motoring mode and rated torque of 398Nm (stator outer diameter of 216 mm)

4.7 Checks on irreversible demagnetisation

As noted in chapter 2, the use of a very high current density can cause problems with irreversible demagnetisation if the local magnet operating point is driven past the knee of the demagnetisation characteristic. Demagnetisation checks were performed on the 30-10 design with the 216mm outer diameter in motoring mode at rated current. This was done by scanning the flux density in every element of the magnet region across the full duration of the simulation to establish the flux density in each element that corresponds to the furthers excursion down the demagnetisation characteristic. The flux density of interest is the component in the direction of magnetisation which is radial in the case of the magnets in these designs. It is interesting first to consider the typical instantaneous flux density magnitude distributions in the magnets under open circuit and on-load conditions shown in Figure 4.17.

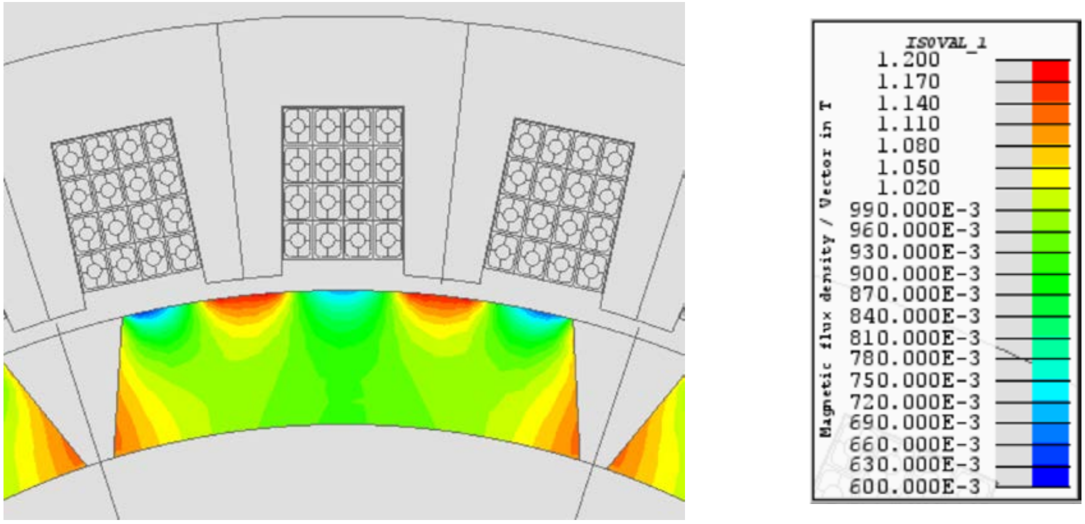

(a) Open-circuit

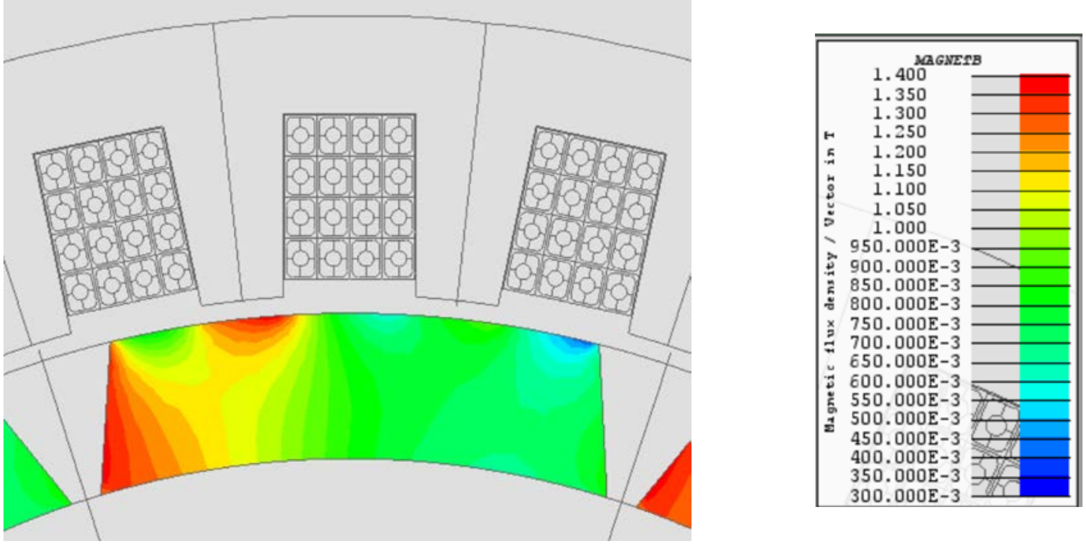

(b) Rated load

Figure 4.17 Instantaneous flux density distribution in the magnet poles at 0.825ms in 30-10 design with 4x4 conductors per slot

As can be seen in Figure 4.17(a) under open-circuit conditions there are areas with higher flux density than the bulk of the magnet (indicated in red) underneath the teeth and area of lower flux density than the bulk of the magnet (indicated in blue) under the slot openings. Hence, even with no current in the stator windings the magnet operating point in element in the rotor magnet model move up and down from the mean operating point. With rated current in the stator windings, there is a degree of asymmetry in the flux density in Figure 4.17 (b) even in this geometrically symmetrical position. This is due to the angle between the field produced by the stator winding and the field produce by the magnet which is essential to produce torque. For the case shown, the machine is operating in motoring mode and rotating in an anti-clockwise direction. It can be seen that since the contours displayed are magnitude and not a signed component that the magnet is pro-magnetised on the leading edge and de-magnetised (though not necessarily irreversibly) on the trailing edge of the magnet. Figure 4.18 shows the distribution of the worst demagnetisation case in each element as measured by the radial component of flux density over one cycle at rated motoring torque. Also shown are radial component of flux density waveforms in the middle of the magnet and in the corners. It is important to note that the flux density components that determine the shading of that element do not necessarily occur at the same instant of time. It is also important to note that because of the orientation of the magnet polarity, that the normal operating under open-circuit conditions result in the radial component of flux density being negative in the magnet, i.e. a radially inward field. Hence, reversible and ultimately irreversible demagnetisation corresponds to this radial component of flux density becoming less negative, i.e. heading towards zero or indeed a positive flux density. In terms of the demagnetisation curve, a zero measure on this scale would correspond to the coercivity and a positive component would indicate 3rd quadrant operation.

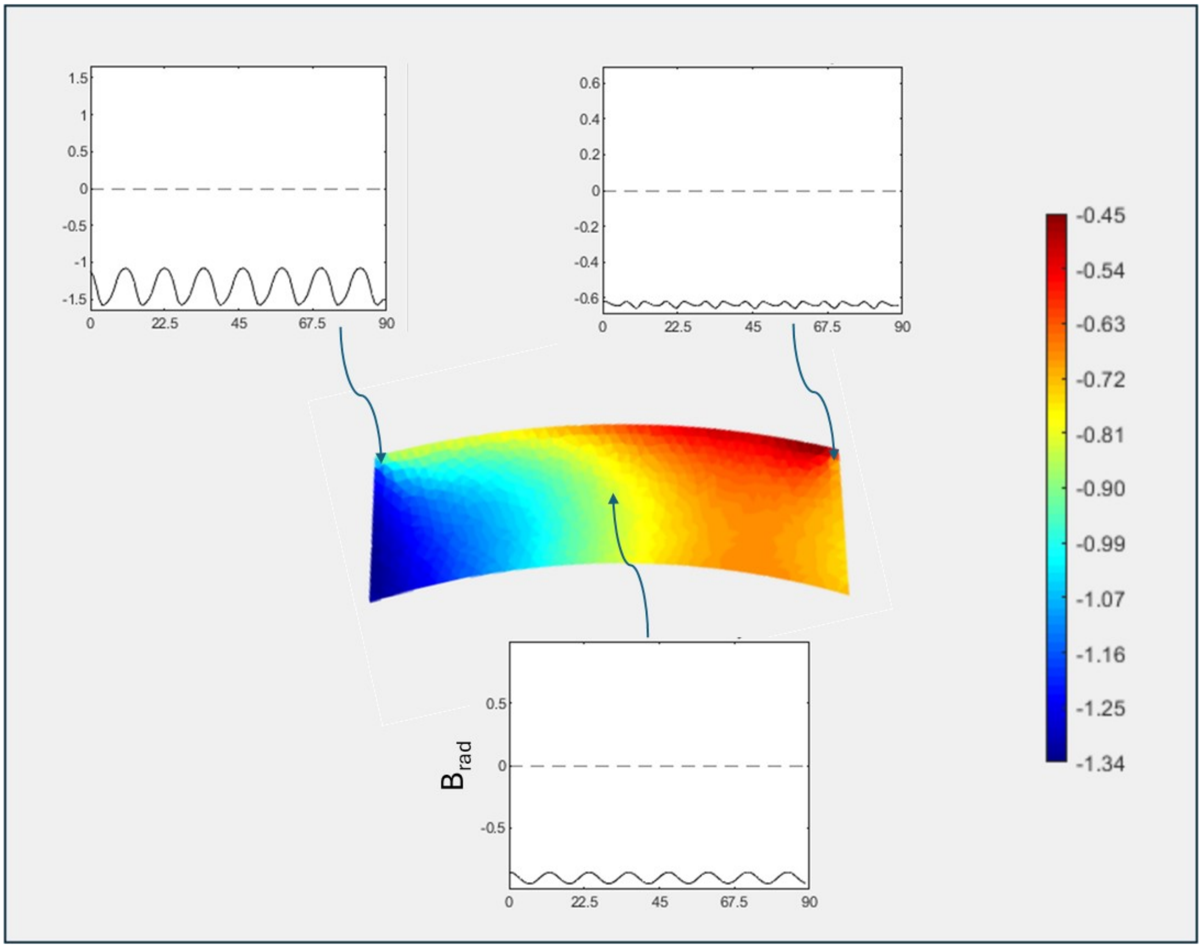

Figure 4.18 Worst case demagnetisiation condition (represented by radial component of flux density in direction of magnetisation) for operation at rated torque in the 30-10 machine (216mm stator outer diameter)

It can be seen from Figure 4.18 that the most positive flux density (which corresponds to the most significant demagnetisation only results in the localised operating point dropping to 0.45T on the trailing tip of the magnet. Hence, there is unlikely to be any chance of irreversible demagnetisation providing a ‘motor’ grade of NdFeB magnet is used or the temperature of the magnet is very high. For example, in the demagnetisation characteristic shown previously in Figure 2.23 for Vacodym 688TP this operating is still above the knee at 240°C. It is interesting to note that some of the flux density excursions are not just due to the stator current but are caused by permeance variations. Figure 4.19 shows the corresponding worst-case demagnetisation case for open-circuit conditions.

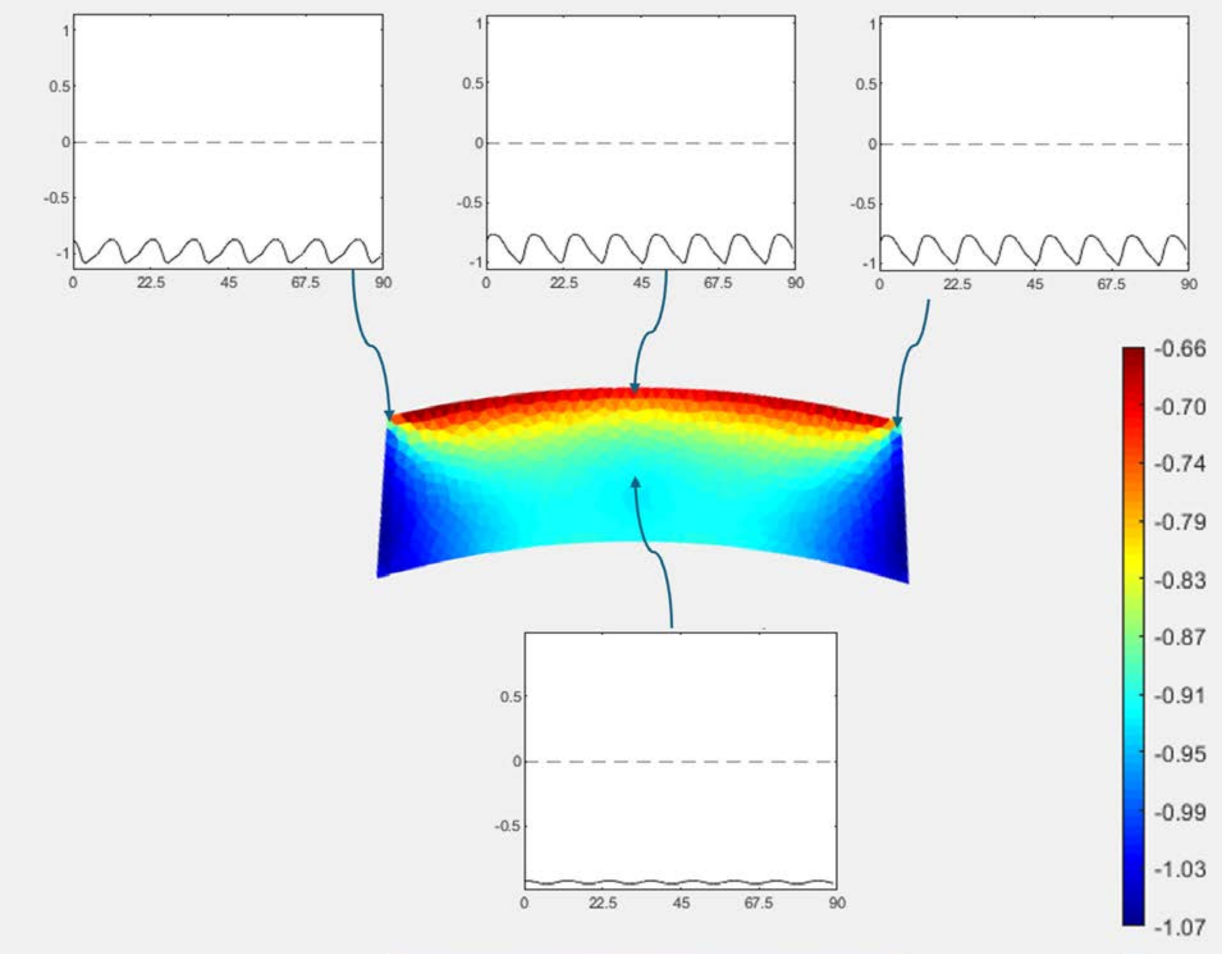

Figure 4.19 Worst case demagnetisiation condition (represented by radial component of flux density in direction of magnetisation) for operation under open circuit conditions in the 30-10 machine (216mm stator outer diameter)

In this open-circuit case, the surface region across the magnet arc is the region with the greatest level of reversible demagnetisation will flux densities up to -0.66T.

This detailed analysis of the demagnetisation performance of the 30-10 design in motoring mode has shown that despite the very current density in the stator. there is a reasonable demagnetisation margin at full rated current providing a suitable grade of magnet material is selected and rotor magnet temperature is managed. Clearly, operation in a faulted mode could produce a current which is multiples of the rated current and in which case, the machine could suffer irreversible demagnetisation.

4.8 Sensitivity study on the 30-10 design

As shown in Figure 4.3(a), the 30-10 design was able to produce an almost linear increase in torque when the current density was extended beyond 38.6 A/mm^2 rms. It has also been shown in this chapter that the back-iron thickness has a significant impact on the power density. Hence, it was decided to investigate whether reducing the back-iron of the 30-10 design would results in an increase in the torque density. The case considered was a small 6mm reduction in the stator outer diameter from 216mm to 210mm. As shown by Figure 4.20 when operating in motoring mode at 38.6 A/mm^2 rms there is an extreme level of bulk saturation in the stator back-iron. The axial length of the machine required to produce 398 Nm is 94.2mm which in turn leads to an overall mass of 14.10 kg, i.e. 2.05kg heavier than the existing design with a 216mm diameter machine. This in turn corresponds to a power density of 17.7kW/kg compared to the 20.8kW/kg for the 216mm stator design.

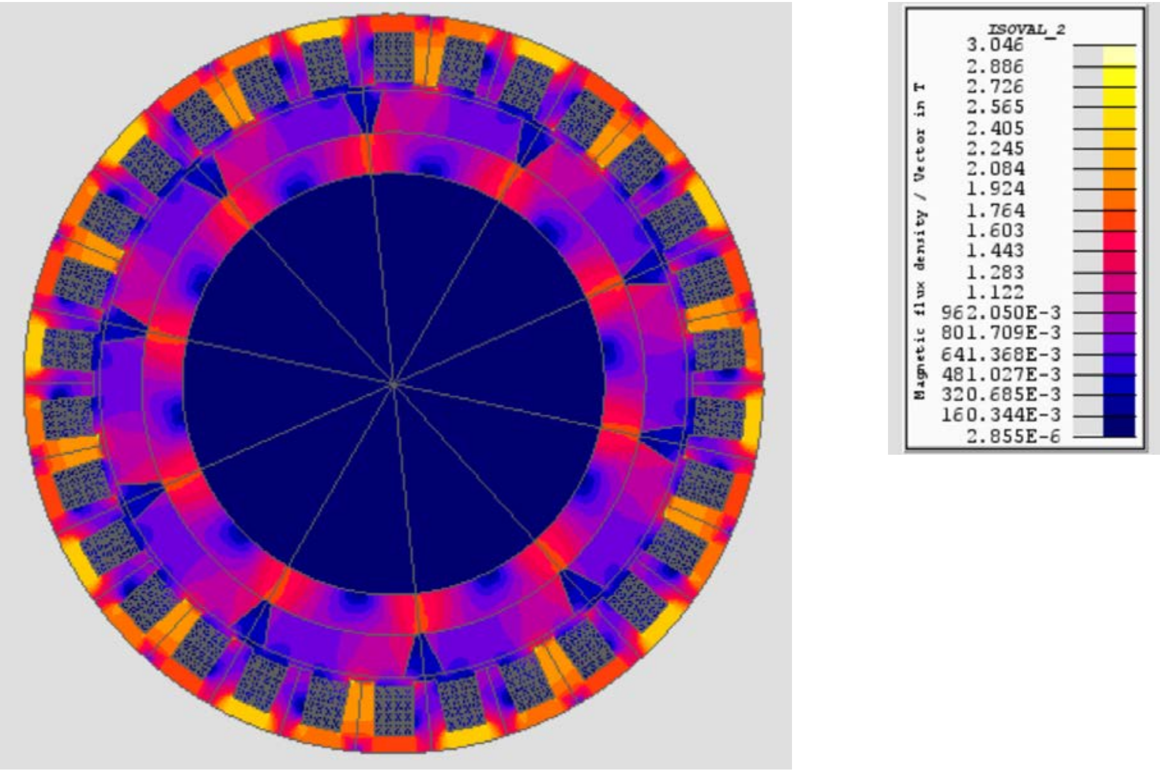

Figure 4.20 Finite element predicted flux density in a 30-10 machine with an outer diameter of 210mm when operating at rated current

Inspection of the flux density distribution in Figure 4.4 for the original 216mm diameter stator suggests the rotor core is only fluxed to a level of 1.6-1.7T. Hence. A further simulation was performed with the shaft diameter increased from 120mm to 126mm but returning the stator outer diameter to 216mm. Figure 4.21 shows the resulting flux density distribution in this revised machine design from which the higher flux density in the rotor core is apparent. The axial length of the machine required to produce 398Nm is 73.8mm which is only 0.6mm longer than the design with a shaft diameter of 120mm. The overall mass saving will depend on what material is used in the larger shaft but adopting this larger shaft leads to an active region mass of 11.54kg, a saving of 0.51kg in active mass. This in turn improves the power density to 21.7 kW/kg. Clearly this machine will need a proportionally large shaft and although this is likely to be a lighter material it will need to be factored in.

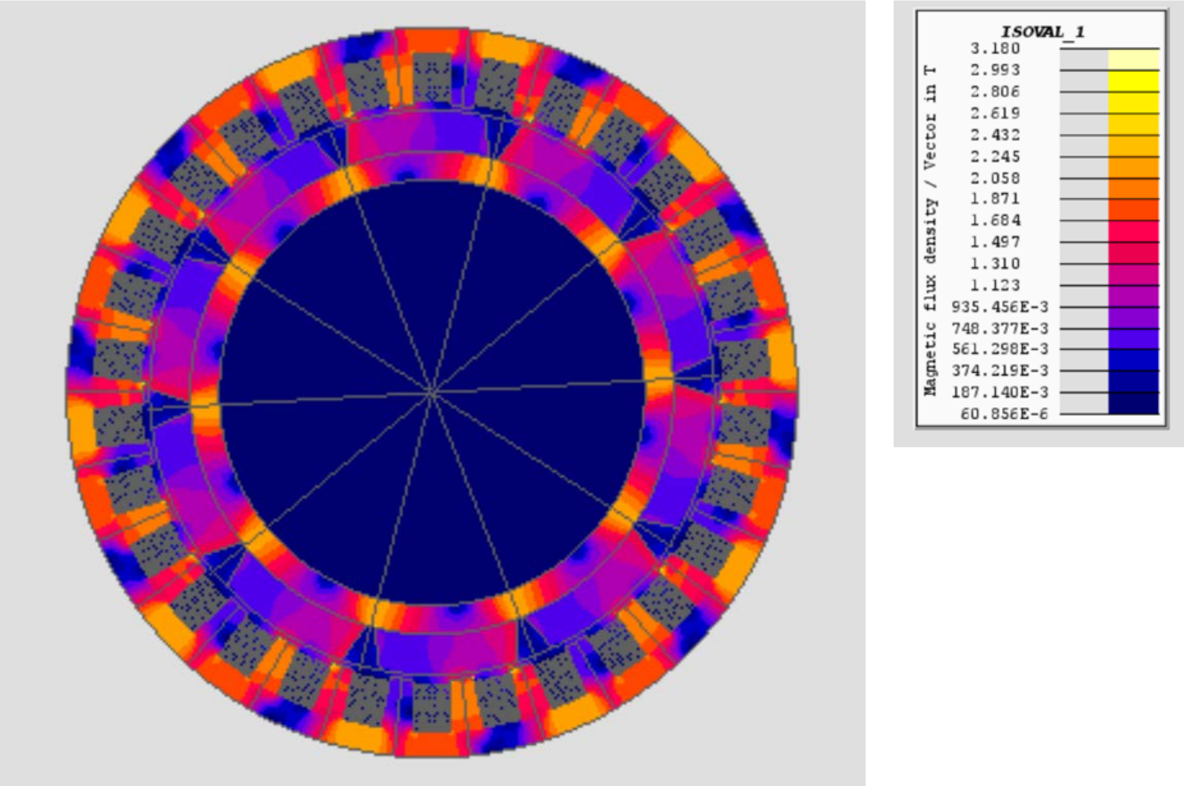

Figure 4.21 Finite element predicted flux density in a 30-10 machine with an outer diameter of 216mm and an increased shaft diameter of 126mm when operating at rated current

4.9 Summary

This chapter has considered several designs of distributed winding machines and has demonstrated that power densities of 21.7kW/kg (active region only) can be achieved but at very high levels of overall loss. Following on from the 10pole concentrated machines studied in chapter 3, a range of pole numbers were considered to understand the trade-off between electrical frequency and hence AC losses versus the large stator core back thickness required to accommodate the pole flux. The most direct comparator with a concentrated winding machine of chapter 3 was the 10-pole distributed winding machine with 30 slots and a simple single layer winding. After some optimisation this achieved a power density of >20kW/kg (based on active region mass only) but at a very high copper loss of 11.46kW at 20°C (12.01kW at 150°C) with almost 50% of the copper loss being AC loss. The lower pole numbers considered, i.e. 4 and 6, reduced the AC losses significantly but as expected required a thicker stator core back-iron and so incurred significant penalties in core mass and hence power density.

A summary of the designs considered in this chapter is shown in Figure 4.22. As can be seen, as was the case with the 12-10 concentrated designs in chapter 3, there is a reasonable correlation between the torque density and the copper loss. Some of the other higher loss designs have a higher loss because of the increased number of conductors operating at the rated current density, but the higher-pole numbers generated more additional AC loss with very high levels of localised loss density in the conductors near the airgap.

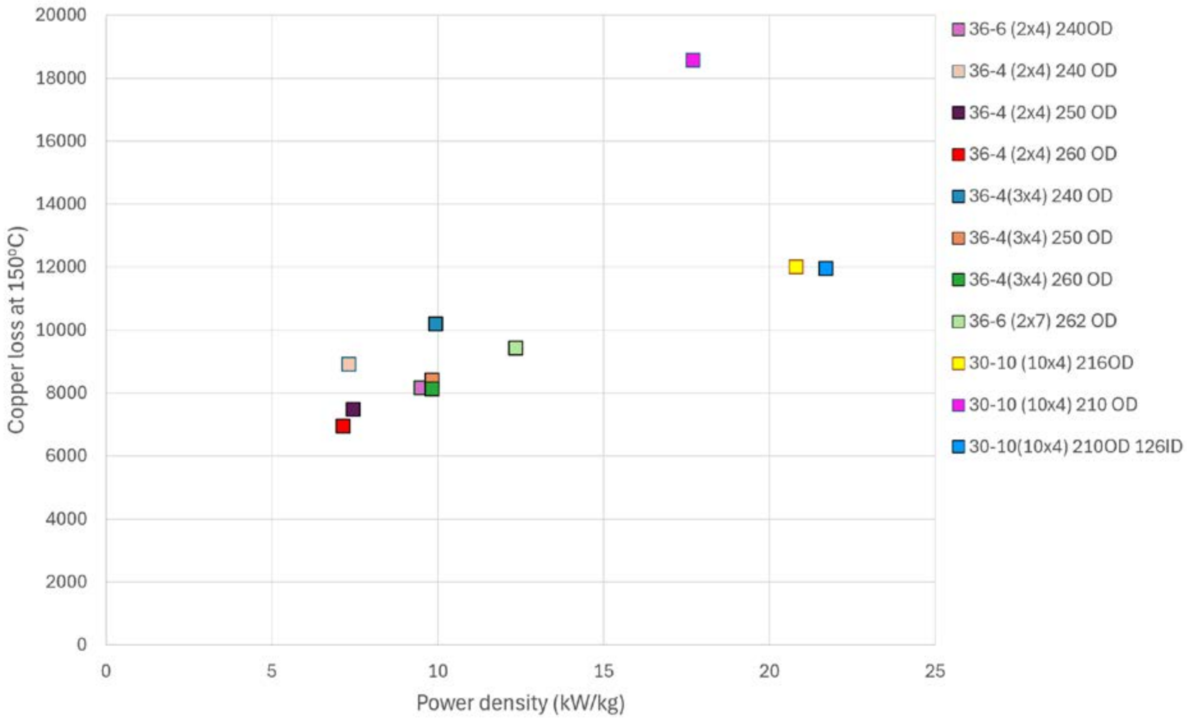

Figure 4.19 Summary of designs of distributed designs from chapter 4

Chapter 4 also considered the issue of irreversible demagnetisation since the slot Ampere.turns are much higher than would be expected in a machine of the same size with conventional conductors. It was shown that at rated current, there was a significant safety margin. It would be necessary in a full machine design to consider fault currents, but fault current levels are not directly related to the use of hollow conductors and high rated currents.

Chapter 5 Experimental testing of a hollow conductor

5.1 Introduction

This chapter describes a series of experimental measurements on the 2.3 x 3mm conductor adopted in the design studies of chapter 3 and 4. The design and analysis presented in chapters 3 and 4 was based on an assumed current density of ~40A/mm^2. There are indications from testing on larger hollow 4x4mm hollow conductors on another project that this is a reasonable assumption as described in Chapter 2. However, to demonstrate that 40A/mm^2 is a reasonable operating current density for the very small 2.3 x 3mm conductor used in the design studies in this thesis when operating with a typical oil coolant and at realistic flow rates, a sample of the conductor was purchased for testing. This testing was done on a test-rig that has been previously designed and built on another project with a larger conductor and used the same method of testing a short length of wire rather than a full coil. Eventually, the feasibility and benefits of oil-cooled, hollow conductors would need to be proved with realistic coils on a full machine, but the testing in this chapter can provide some confidence about the heat-transfer capability of hollow-conductors and starts to quantify their performance advantages compared to conventional conductors.

5.2 Conductor and coolant details

5.2.1 Hollow Conductor

The rectangular hollow conductor considered in this chapter was shown previously in Figure 2.9 and 3.1. It has an overall cross-section of 3mm x 2.3mm with a 1.3mm diameter circular duct at its center and four 0.5mm radiused corners which results in a net copper cross-section of 5.36mm^2. The radiused corners and the circular duct already reduce the conducting cross-section to ~78% of an equivalent 3mm x 2.3mm rectangular conductor. Of the 22% loss in conducting cross-sectional area, 19% is lost by incorporating the central duct and only 3% from the radiused corners. Hence, there is already a significant reduction in the eventual slot-fill factor that can be achieved compared to a solid strip conductor. The conductor is insulated with a PEEK coating which is a high-performance polymer with a continuous operating temperature limit of 260°C with short term excursions to 300°C [ZEU2025].

This conductor was manufactured by Luvata and is the smallest conductor they offer and was developed to target the electric vehicle traction market.

5.2.2 Coolant oil

The oil used in this set of experiments was Midel 7131 which is a bio-degradable synthetic ester dielectric oil which is widely used in electrical equipment. It has been used previously for flood cooling machine because of its good high temperature properties and excellent electrical properties. Its key physical and thermal properties are summarised in Table 5.1.

Table 5.1 Midel 7131 key thermal properties

Thermal conductivity	0.148 W/mk at 0°C 0.145 W/mk at 50°C 0.138 W/mk at 100°C 0.127 W/mk at 150°C
Specific heat capacity	1180 J/kg/K at 0°C 1969 J/kg/K at 50°C 2106 J/kg/K at 100°C 2240 J/kg/K at 150°C
Density	982 kg/m3 at 0°C 946 kg/m3 at 50°C 910 kg/m3 at 100°C 874 kg/m3 at 150°C

As will be apparent in Table 5.1, many of the properties vary significantly over the temperature range of interest in electrical machine. One feature of the oil which is important in this application is the variation of oil viscosity with the temperature. The viscosity versus temperature characteristics of Midel 7131 supplied by the manufacturer is shown in Figure 5.2. As can be seen, there is a factor of 100 change between 0°C and 150°C. This is particularly important in terms of the pressure drop within the duct and as will be shown, is a major factor in the suitability of a particular oil.

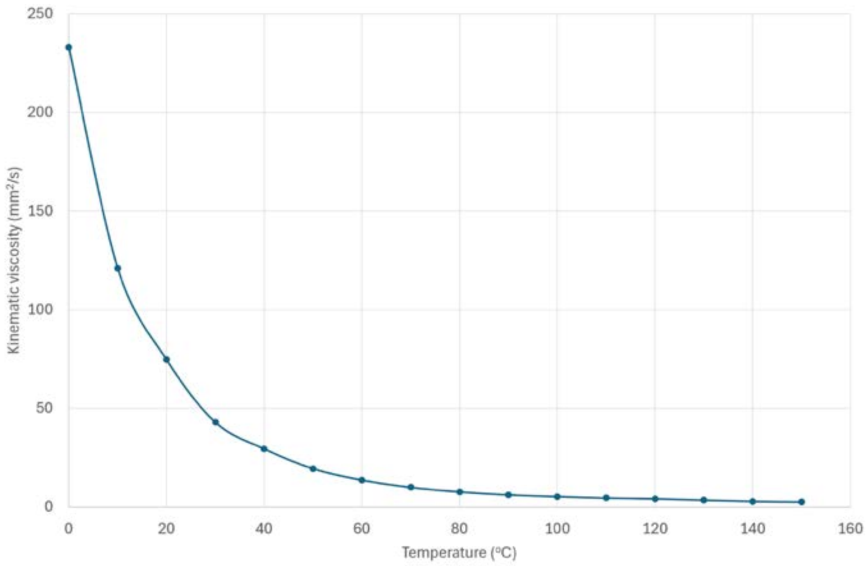

Figure 5.2 Variation of Midel 7131 kinematic viscosity with temperature (Manufacturer data)

5.3 Test-rig

In order to experimentally characterise the conductor thermal and electrical behaviour a custom test-rig was used. This was originally designed to characterise a 1m long piece of 4x4mm conductor with a 2mm duct as part of a separate research project. A schematic of the test-rig is shown in Figure 5.3. The test-rig system consists of five sections: an oil temperature control unit (which includes a pump), control and manual valves, a 1200A DC power supply, a thermal test chamber and the data acquisition systems and associated sensors. Together, these components provide an experimental setup that allows for a thorough and reliable analysis of the hollow conductor performance under varying conditions.

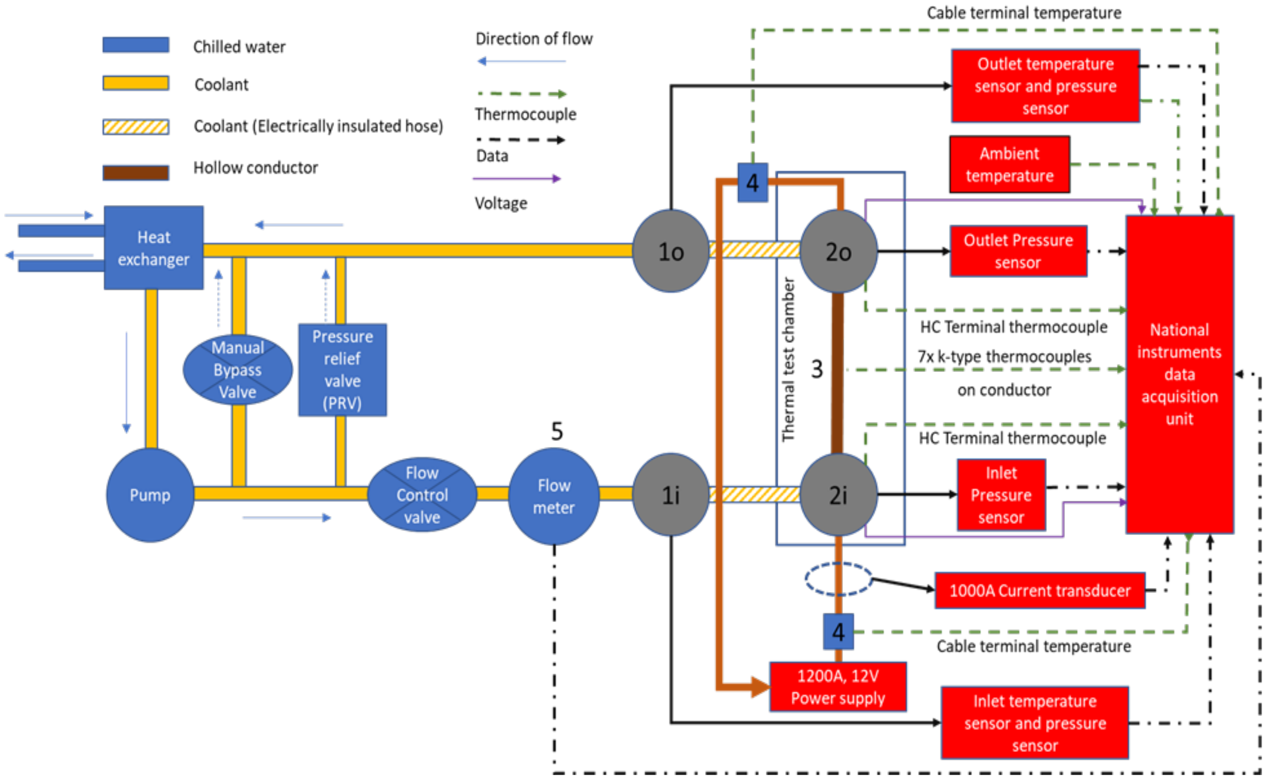

Figure 5.3 Schematic of test-rig

5.3.1 Power supply

The current to the conductor is supplied by a Xantrex XDC10-1200 (10V, 1200A, 12kW) DC regulated power supply which operates in constant current mode and so is able to maintain a pre-set current density in the conductor as it heats up and its resistance changes.

5.3.2 Thermal test chamber

The hollow conductor is enclosed in a thermally insulated test chamber that is designed to minimise heat leakage from the conductor to the external ambient. A close up of the test conductor in the thermal chamber is shown in Figure 5.4. As noted previously, the test chamber was designed for 1m long piece of a larger hollow conductor with a 2mm diameter duct and the initial plan was to also use a 1m length of the 2.3x3mm conductor. However, the reduced duct diameter meant that the pressure drop for a 1m length at the top end of the flow rate range was greater than the pump pressure capability and so a shorter 220mm length was used. The sample in the chamber is shown in Figure 5.5. The hollow conductor was connected to the electrical supply and the cooling oil inlet and outlet pipes with the custom made connectors.

Figure 5.4 Thermal test chamber

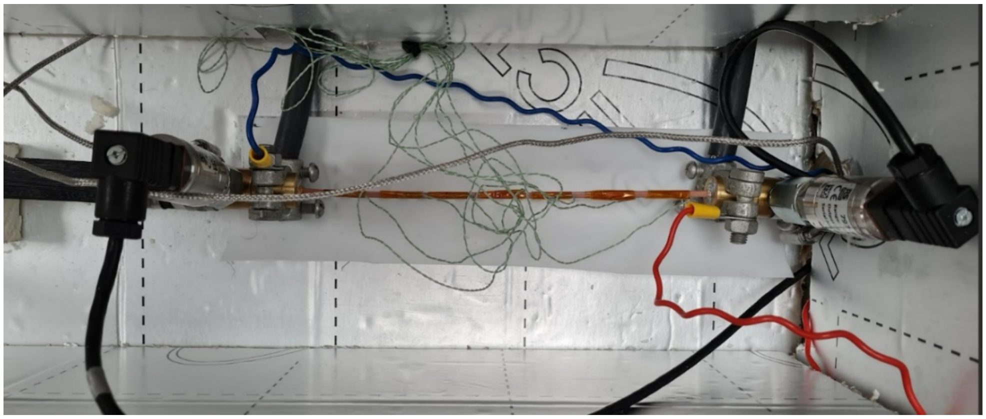

Figure 5.5 The 220mm long sample sin the thermal chamber with the various connectors and sensors attached

5.3.3 Oil supply system

The oil supply system consists of a number of subsystems and valves. Key elements of the system shown are shown in Figure 5.6

- **Tool-Temp** - This is a programmable heater and heat-exchanger is responsible for maintaining a stable and defined oil temperature throughout a testing sequence. This unit is a commercial system designed for controlling the temperature of injection moulding tools but is well suited to providing controlled temperature oil circulation for experimental test-rigs. The unit circulates the cooling oil in the test-rig through a chilled-water heat exchanger which in combination with an electric heating stage is able to regulate the inlet temperature of the oil to within ∓1°C but with some hysteresis.

- **By-pass valve** - The pump inside the Tool-Temp unit has a minimum operating flow-rate to avoid overheating and so in order to ensure that this minimum is met, the system includes a manually adjustable by-pass valve.
- **Flow-control valve** - This in-line valve is a manually adjustable valve which is used to separately control the flow-rate in the conductor and is adjusted during testing as the oil temperature and hence viscosity change. However, because of the very low flow-rate which results from the combination of the small duct and 4.2 bar pressure limit, it was not necessary to use this flow-control valve and the system was run with no flow restriction
- **Pressure-relief valve** - This is a safety device which activates if the pressure in the system exceeds a pre-set limit of 6 bar.

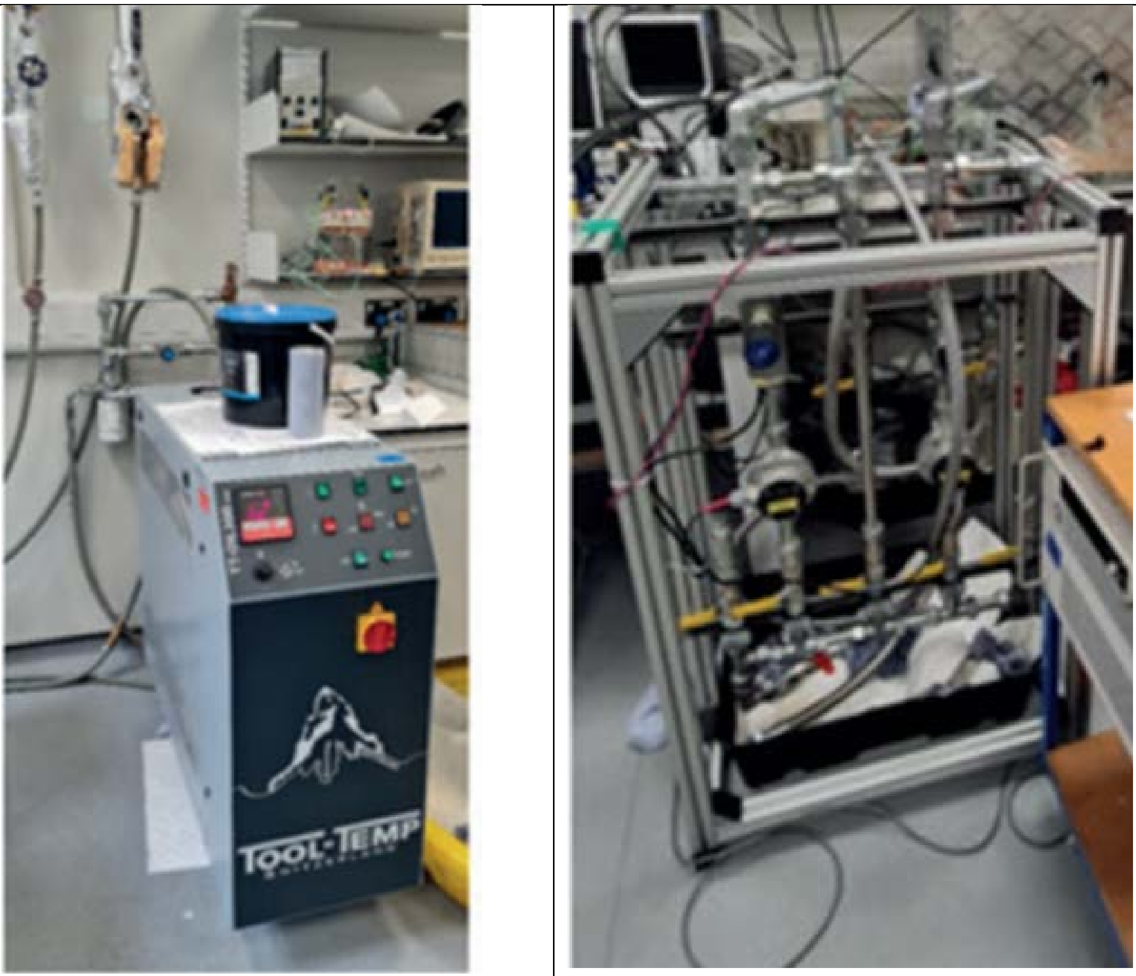

(a) Tool-Temp temperature control unit (external chilled water connections in background)

(b) Pipework, values and flow meters

Figure 5.6 Key components of oil supply system

5.3.4 Instrumentation and data acquisition system

The test-rig is fitted with many measurement sensors and systems and these are all integrated into a National Instruments data acquisition system. The sensors are listed in Table 5.2.

Table 5.2 Sensors in the test-rig

Measurement quantity	**Location**	**Device description**	**Range**	**Location in fig3.3**
Coolant inlet pressure	Hollow conductor terminals and thermal chamber external liquid connections	RS PRO Pressure Sensor, Max, Voltage Output	0-25 bar	1i, 2i
Coolant outlet pressure	Hollow conductor terminals and thermal chamber external liquid connections	RS PRO Pressure Sensor, Max, Voltage Output	0-25 bar	1o, 2o
Temperature of coolant (Midel7131) at inlet and outlet of thermal chamber	Thermal chamber external liquid connections	3.0mm mineral insulated thermocouple probe, Grade 310 Stainless Steel	to +1050°C	1i, 1o
Temperature of coolant (Midel7131) at inlet and outlet of hollow conductor	Hollow conductor liquid connection terminals	3.0mm mineral insulated thermocouple probe, Grade 310 Stainless Steel	to +1050°C	2i, 2o
Temperature of hollow conductor sample	At defined positions along hollow conductor sample	Type K - Welded Tip Thermocouple	-75°C to +250°C	3
Temperature of Hollow Conductor terminal	Hollow conductor terminal	Adjustable Ring type Thermocouple Type K, 13-20mm	0 to +1100°C	2i, 2o
Coolant flow rate	Inline with fluid inlet	Low Flow Oval Gear Flowmeter, , Hall effect pulsed output	2-100 L/Hr	5

The data is all captured and logged by the data acquisition system and displayed in real-time using Labview.

5.4 Experimental methodology

There are several challenges in obtaining reliable measured data from this test-rig. The significant change in viscosity with temperature of the cooling oil means that achieving a particular level of flow rate involves a lot of manual adjustment of the flow-control valve and a very long run time to allow steady conditions to be achieved. This is particularly challenging because the pump is operating near its maximum outlet pressure for this very small duct. Despite significant efforts to achieve an exact flow-rate, ultimately some known variation was accepted and fully captured in the reported data, i.e. the problem is not accuracy of the data but that it is not at specific and identical set-points. The various thermal time-constants of the test-rig mean that reaching steady-state (defined as a change of <1°C change in temperature in 5mins) can take several hours for each set-point even when they are done sequentially and not from a cold start.

The hollow conductor under test was electrically connected to the DC power supply with high current cables with current densities of 50A/mm^2 corresponding to currents of 268A. This requires high current connecting cables from the power supply and since these are not cooled by the oil, they need to have a large cross-sectional area to prevent them overheating. This means that they act as a heat-sink for the heat generated in the hollow conductors and so before any testing with a coolant was performed a dry run with no oil was performed to calibrate for the heat-sinking effect of the cables, which assumes that negligible heat flows through the thermal chamber structure.

After a dry run has been completed, oil was pumped around the system and the current set on the power supply in constant current mode. The various valves were then carefully adjusted to get various test points over the temperature and flow-rate range.

5.5 Experimental results

5.5.1 Dry conductor testing

The first test performed on the conductor sample was a dry test with no Midel 7131 in the system. The main purpose of this test is to quantify the other heat transfer from the conductor, the most significant being heat conduction into the connecting cables. The power supply was set to a particular current set-point and the temperature measurements from each thermocouple were allowed to come to steady state (<1% change in 10 mins). Figure 5.7 shows the measured steady-state temperature at a series of 7 equally spaced locations along the conductor at 3 different current density levels. Location 1 corresponds to the far end of the conductor which will become the outlet end when oil flows.

In these measurements, the ambient temperature of the laboratory was 22°C and cable surface temperature measured on the go and return cables were 25.9°C and 25.6°C. As can be seen from Figure 5.7, the temperatures measured along the conductor with no coolant are a maximum towards the centre of the conductor. This is because the main heat sinking path for the losses in the conductor are along the conductors and into the large connecting cables at each end. This heat-sinking effect into the external cabling is significant and allows this conductor to operate at the reasonably high current density of 14A/mm^2 with no coolant. However, the very short conductor length means that the heat-sinking effect of the cable is both effective but not representative of a practical multi-turn coil.

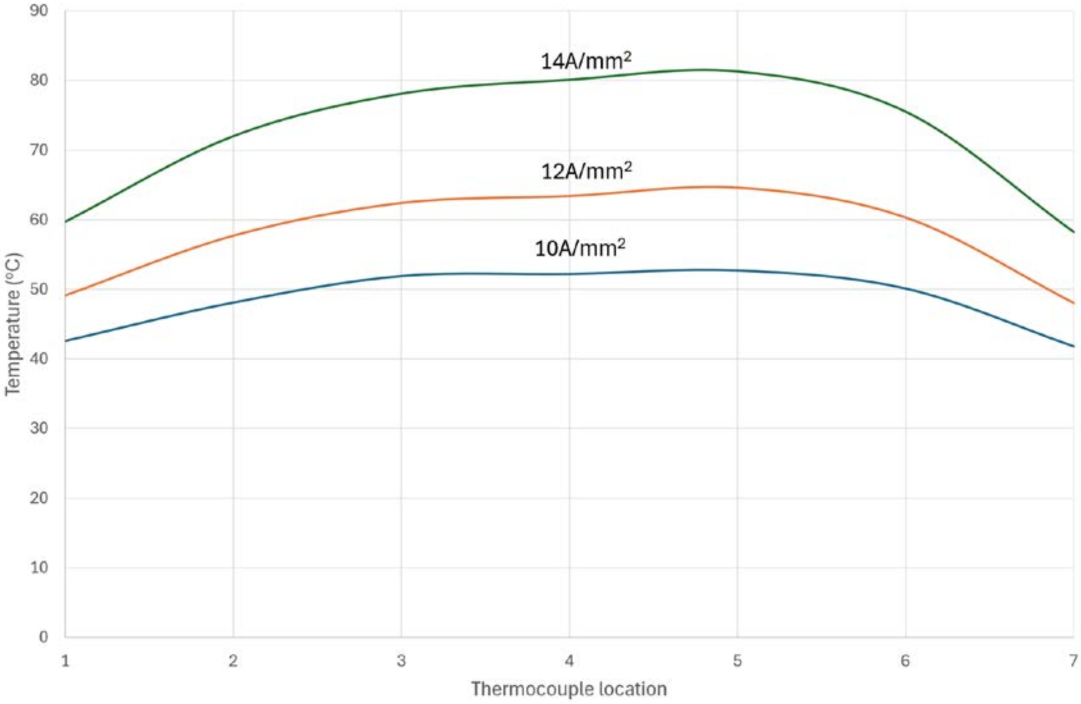

Figure 5.7 Measured temperatures at locations along the conductor during a dry run test with no coolant at 3 different DC current densities

5.5.2 Testing with oil flow

A series of tests were run at current densities from DC current densities between 16.5A/mm^2 and 50A/mm^2 with Midel 7131 as the cooling oil. Although the intention was to vary the flow rate, the pressure drop in the 1.3mm duct with the Midel 7131 only allowed a 0.5 litre/min flow rate over the temperature range in the tests at the pump output pressure rating of 4-5 bar. In addition, fine control of the flow rate was not possible and so some variation in flow rate with current density and hence oil temperature was obtained as shown in Figure 5.8. This increase in flow rate with current density occurred because of the additional heating of the oil and the steep variation in viscosity in this temperature range. Hence, as the oil heated up at higher current densities the pump was able to drive more flow at its pressure limit. A high-pressure pump with some margin in pressure would allow a higher flow-rate. In the longer term, there is a plan to add a high pressure pump to go up to 30 bar (which is the hydraulic pressure limit of the conductor with a recommended safety factor).

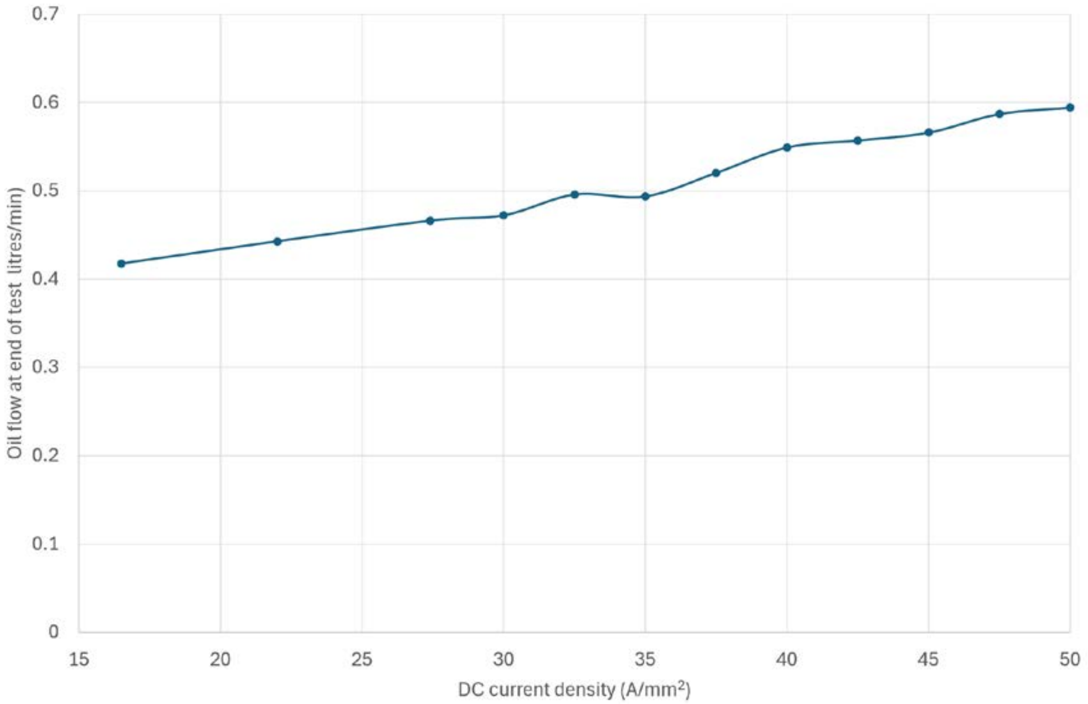

Figure 5.8 Variation in oil flow around the nominal 0.5l/min test point as function of current density

During each test, which typically took 5-6 hours to reach steady-state, the temperature at 7 equi-space locations along the conductor surface was measured with thermocouples which are designated TC1(outlet) to TC7 (inlet). Figure 5.9 shows the variation in temperatures during the test at 50A/mm^2 of these thermocouples and some other temperature sensors in this system. As would be expected, the highest temperature is near the outlet with the lowest near the inlet. With the exception of TC4 and TC5, these follow the expected increase in temperature along the flow path although the differences were greater than the variation in oil temperature between the inlet and the outlet Also shown are the oil inlet and outlet temperatures, which show that in steady-state at the end of the test, the temperatures are 46.6°C and 49.2°C respectively, i.e. less than a 3°C temperature rise.

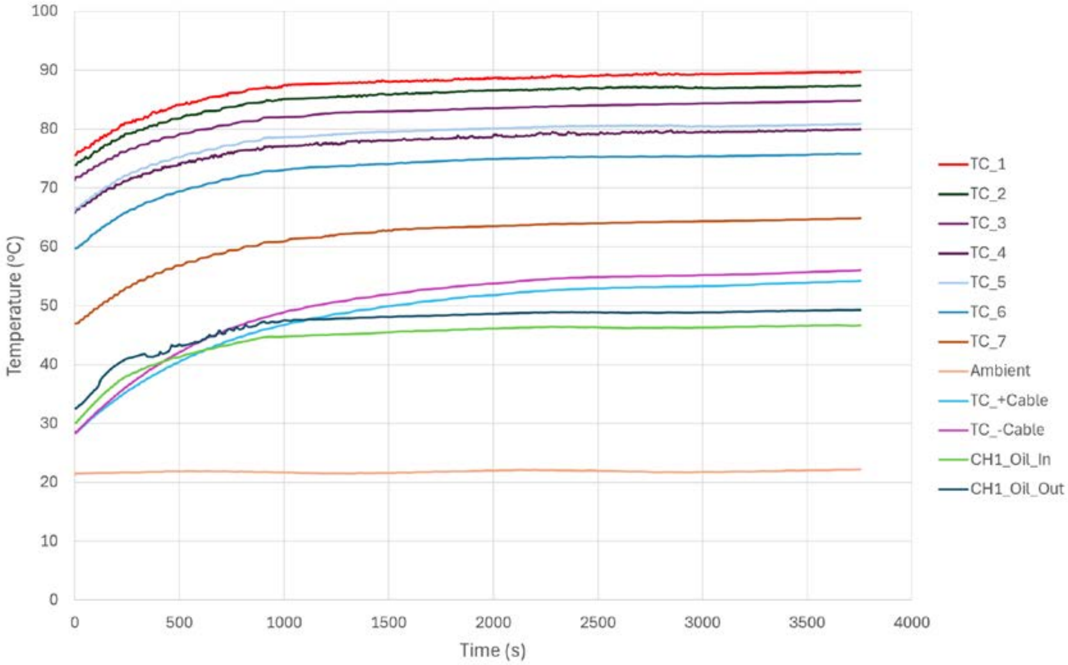

Figure 5.9 Measured temperatures in the thermocouples attached to the conductor and connection cable and oil inlet and outlet sensors

Figure 5.10 shows the corresponding variation in the pressure drop. The various adjustments made in the valves to control flow as the oil heats up are evident in the various small steps. The corresponding variation in flow rate during the 50A/mm^2 test are shown in Figure 5.11.

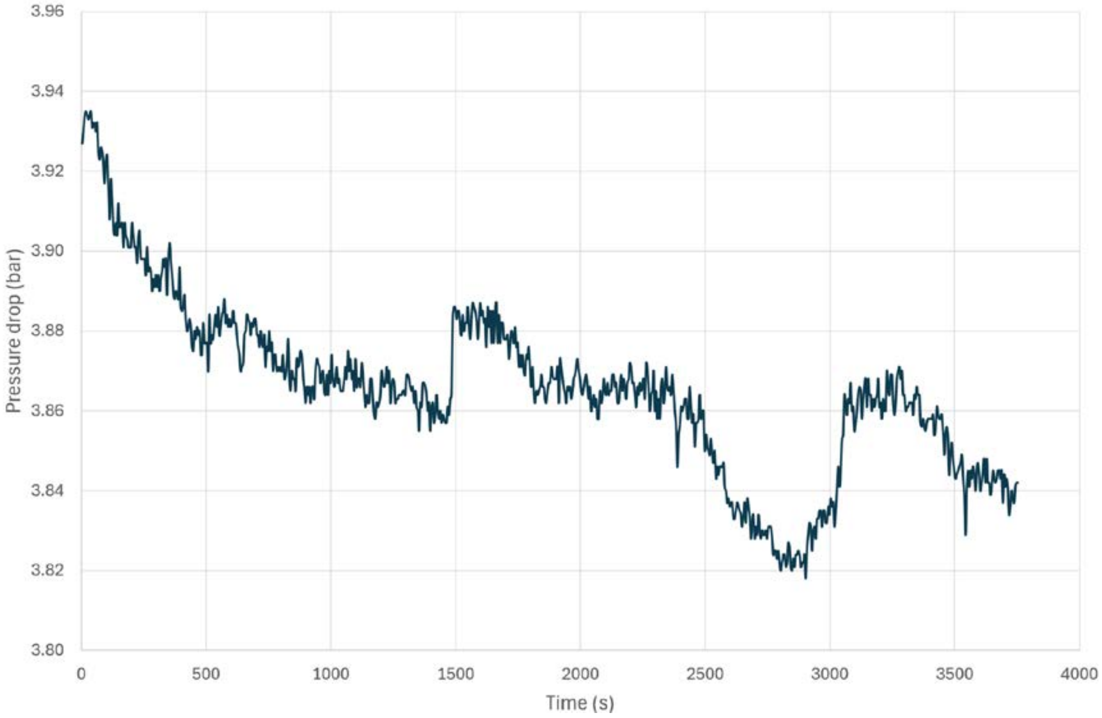

Figure 5.10 Variation in pressure drop across the conductor during the test

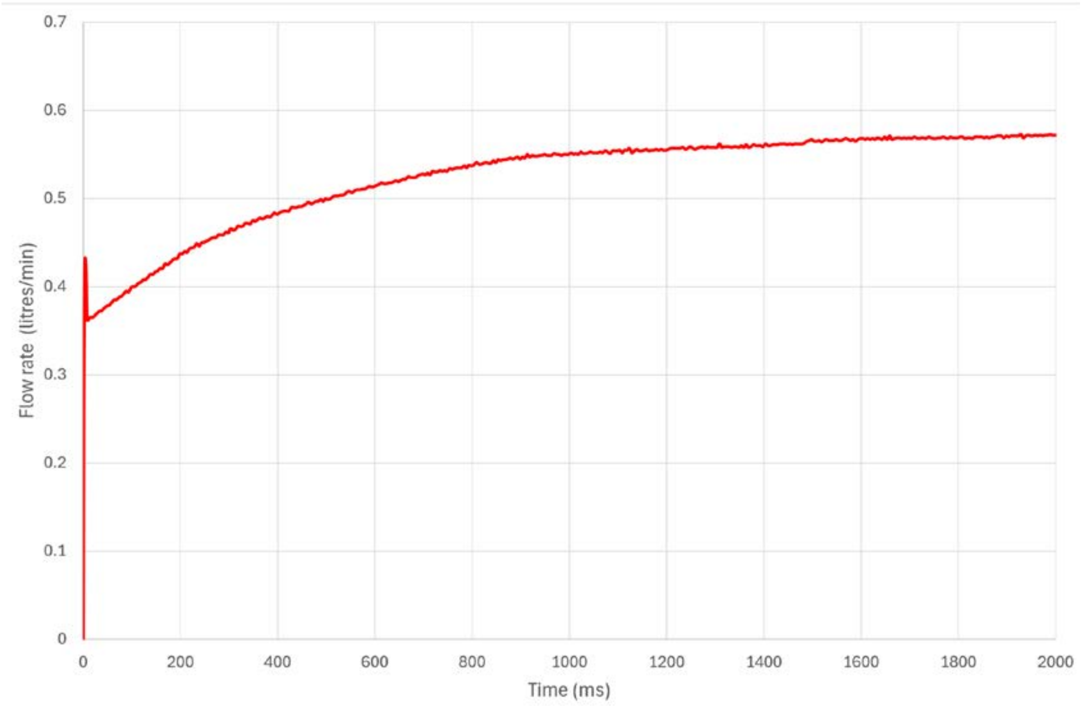

Figure 5.11 Variation in flow rate during the first 2000s of the 50A/mm^2 test

Very similar sets of data were collected for the 12 different current densities considered. Figure 12 shows a summary of steady-state temperatures for the 12 current densities considered. As would be expected the temperature difference along the conductor starts to increase as the current density is increased. However, even with this highest current density and a relatively low flow rate of 0.5 litres/min, the temperature rise in the oil is only 3°C. It should be noted however that the sample is only 220mm long and hence at this flow rate the temperature rise per m of length in an actual coil would be ~14°C at this flow rate.

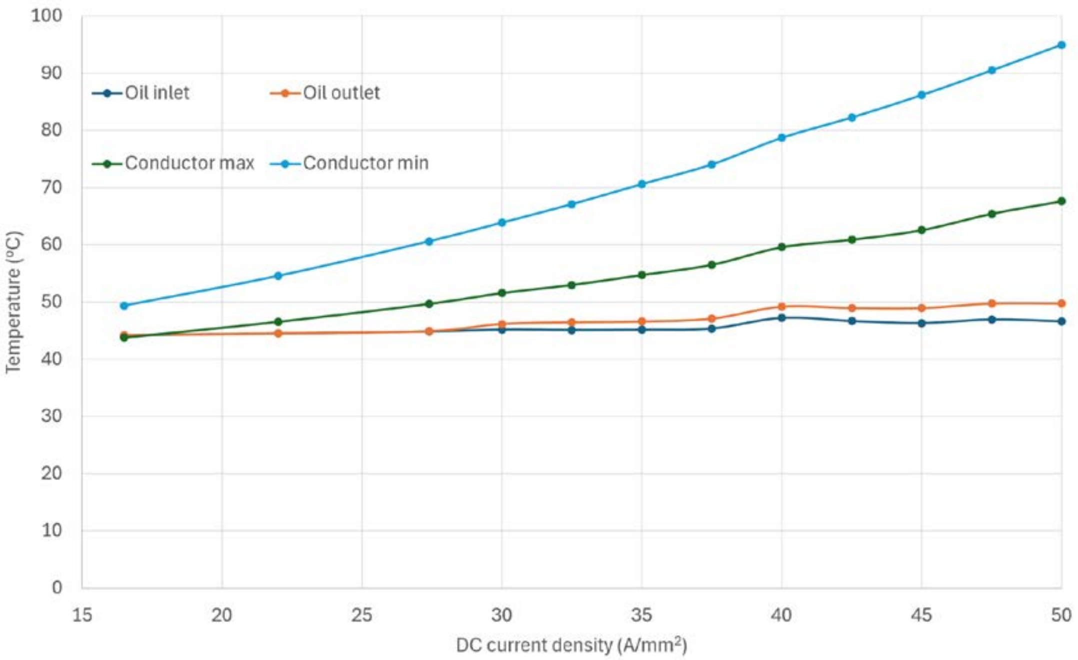

Figure 5.12 Variation in steady-state (end of test) key temperatures for different current densities

5.6 Discussion of results

The experiment reported in this chapter was challenging in part because the rig was designed for a larger hollow conductor with a reduced pressure drop and the pump pressure was not suited to the very small duct and reasonably high viscosity oil. On the basis of the results taken, the performance of this conductor can be summarised by noting that it is capable of operating at 50 A/mm^2 with the wire remaining below 100°C despite a modest flow rate of 0.5 l/min. This demonstrates the effectiveness of hollow-conductor cooling in allowing machines to be design with current densities of 50A/mm^2 even with low flow rates.

However, at this flow rate and in the temperature range 60-100°C the pressure drop would be an excessive ~16.6 bar for every m of coil length based on linear extrapolation. The key factor in determining the viability of operation with the MIDEL oil chosen in this study will be the maximum allowable oil pressure that can be used while remaining within safety guidelines. Some more recent work on a separate project in Sheffield has shown that pressures of 100 bar may be achievable within safety margins for hollow copper conductor which would allow up to 6m of conductors to be used to form a coil. The test-rig described in this chapter is being upgraded with a high-pressure pump that would allow this to be investigated in the future, but high pressure operation could not be tested within the timeframe of this current project.

Another issue which needed to be taken into account is the effect on the flow and pressure drop of curved sections such as the end-windings.

Another method for increasing the viability of achieving 0.5l/min in this conductor is to change to a coolant with a much lower viscosity, even if this involves some compromises in other properties. There is a further discussion of this point in Chapter 6.

Chapter 6 – Conclusions

6.1 Key findings

This thesis has reported on an investigation into hollow conductors as a technology for improving the power density of permanent magnet machines. The developments and issues around hollow conductors, particularly AC losses, were reviewed in chapter 2. This included a study which demonstrated that relying on a classical skin-depth calculation to assess whether eddy currents and AC resistance will be problematic is very oversimplified. It was shown that multiple solid conductors in a slot in a soft magnetic core will exhibit significant eddy current loss at frequencies well below those predicted by a classical skin-depth calculation.

Chapter 3 presented a design study on a series of concentrated winding permanent magnet machines to meet a representative 250kW specification for distributed propulsion drives. A 12 slot, 10 pole geometry was chosen as it offers a slightly higher winding factor than a more conventional 12-8 arrangement and the increased pole number allows some saving to be made in the back iron thickness. Various 1,2 and 3 layer windings were considered including an unusual arrangement with multiple concentrated coils sharing a slot. Overall, these designs which were based on very similar stator core geometries were quite clustered in terms of power loss and power density. As noted in chapter 3, the use of a 12-10 machine does raise the issue of magnet eddy current loss as this is a slot-pole combination that produces a very harmonic rich airgap field.

Chapter 4 presented a design study on a series of concentrated winding permanent magnet machines. This demonstrated the advantages of adopting a high pole number from the perspective of power density but this is at the expense of increased AC losses in the hollow conductors. One interesting result is that magnetic saturation in the core can have a very significant impact on the AC loss and that once the stator core is pushed too hard in terms of magnetic saturation there is both a mass increase from the increase in axial length. The research included consideration of the irreversible demagnetisation and demonstrated that a combination of a thick magnet and a high coercivity material such as a ‘motor# grade of NdFeB provided a good safety margin at rated current.

Figure 6.1. shows a summary of the losses and power density achieved for the 18 designs which are analysed in detail in chapters 3 and 4. The highest power density, noting that end-winding were not included in this assessment, is the 30-slot, 10 pole distributed winding machine. This is due to a combination of high pole number allowing a thin back iron and a large number of conductors per slot. It was shown in the analysis of several designs that incorporated many turns into a wide slot tends to provide benefits in terms of torque density when the current density is fixed. However, this combination of high pole number and a large number of conductors does result in a high loss density, including significant AC component to the loss. The highest power density achieved was 21.7kW/kg. It is important to reiterate that this is based on the active mass only and allowance for the end-windings and casing would need to be added in.

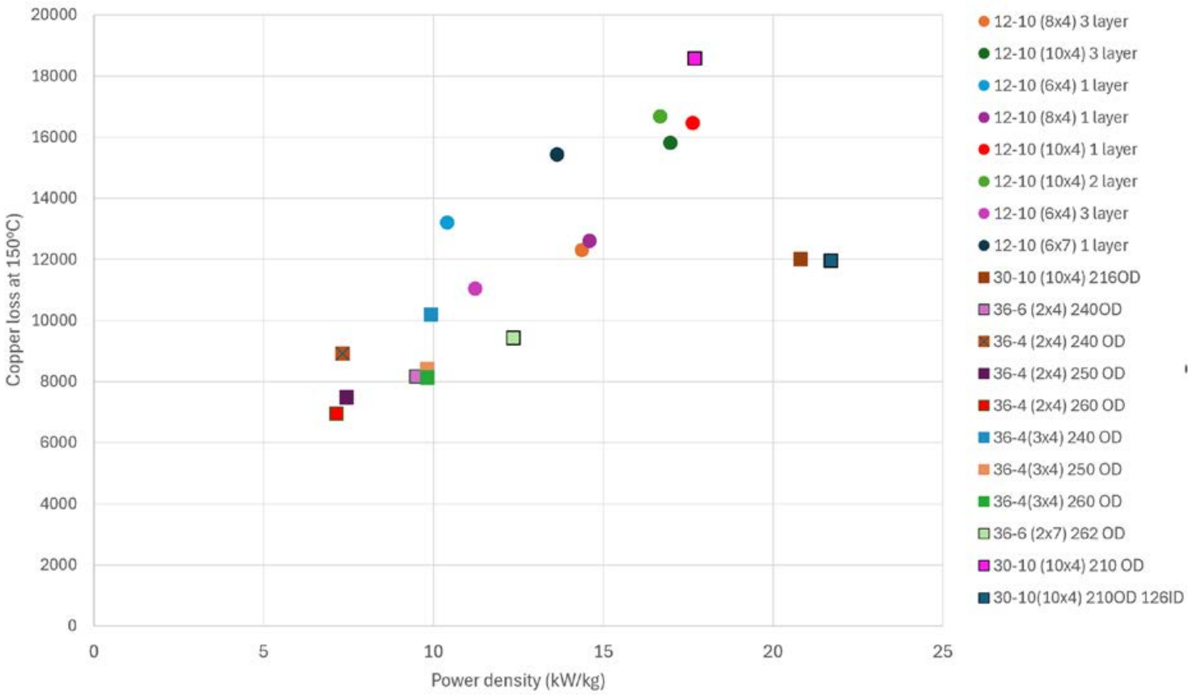

Figure 6.1 Summary of all design study performance outcomes

The experimental results in chapter 5 have shown that although such small hollow conductors may appear to be a good fit to EV traction machines and other applications with power ratings in the 10-100kW range, in practice the small diameter duct and hence the high flow resistance means that unless a much lower viscosity fluid than an oil such as Midel7131 is used, they do not offer a practical solution for coil containing many turns or a chains of series connected flow paths. The results in chapter 5 also showed that from a cooling perspective direct liquid cooling is very effective and that even with Midel 7131 which is not well suited to such small ducts, then current densities of 50A/mm^2 and possibly higher could be sustained on a continuous basis with the correct hydraulic arrangement.

6.2 Key novelties

- This thesis has reported one of the very few research projects on the use of the new generation of small hollow conductors intended for small and medium machines.
- This is the first report in literature of the AC losses in hollow at machine level with a great deal of detail on the influence of electrical frequency and magnetic saturation in the core on AC losses.
- The investigations in chapter 4 of the influence of pole number on AC loss demonstrated the interaction between AC loss and magnetic saturation in the core and the fact that exploiting the very high current densities which can be achieved with hollow conductors requires careful optimisation of the core geometry.

6.3 Future Work

The research reported in this thesis has identified several issues which could not be investigated further in the time available and would form topics for a future research programme:

- Establish the best configuration of coils to manage pressure in conductors with small ducts, e.g. coils in electrical series but in parallel from a fluid flow point of view.
- Build and test a prototype with a high-pressure pump to validate the findings.
- The research in this thesis has focussed almost entirely on copper loss since the current density levels involved will make this the dominant loss mechanism. However, prior to any prototyping of the preferred design, it would be necessary to also calculate the iron loss and the rotor magnet loss to manage the machine thermally.
- The analysis has focussed on the active region and the masses and losses quoted have not included end-windings. Including consideration of end-windings into the modelling with

a reliable method for estimating end-windings which takes into account of the practical difficulties of forming compact windings would be a useful addition.

- Finally, there is some on-going at the University of Sheffield on the use of compressed air as the cooling medium for hollow conductors in order to overcome the pressure drop difficulties with an oil coolant. This has not been published yet but the electromagnetic aspects of this thesis in chapters 3 and 4 are not specific to any cooling fluid except that the findings are specific to current densities of ~40A/mm^2.

References

[ADU22] Adu-Gyamfi B.A., Good C., “Electric aviation: A review of concepts and enabling technologies”, Transportation Engineering, Vol 9, 2022. Ref: 100134.

[BAL19] A. Balachandran, M. Boden, Z. Sun, S. J. Forrest, J. D. Ede and G. W. Jewell, "Design, construction, and testing of an aero-engine starter-generator for the more-electric aircraft," in The Journal of Engineering, vol. 2019, no. 17, pp. 3474-3478, 6 2019, doi: 10.1049/joe.2018.8235.

[BAR22] Bardalai, A.; Gerada, D.; Zou, T.; Degano, M.; Zhang, C.; Gerada, C. Comparison of AC Losses in the Winding of Electrical Machines with Fixed Strands Positions, Fixed Conductor Shapes and Random Winding. *Energies* **2022**, *15*, 5701. https://doi.org/10.3390/en15155701.

[BOG09] A. Boglietti, A. Cavagnino, A. Tenconi, and S. Vaschetto, “The safety critical electric machines and drives in the more electric aircraft: A survey,” in Proc. 35th IEEE IECON,2009, pp.2587–2594.

[BOW18] C. L. Bowman, Marien V., Felder J.L. ‘Turbo- and Hybrid-Electrified Aircraft Propulsion for Commercial Transport’, 2018 AIAA/IEEE Electric Aircraft Technologies Symposium, July 9-11, 2018, Cincinnati, Ohio. https://doi.org/10.2514/6.2018-4984.

[CAM16] R. Camilleri, D. A. Howey, and M. D. McCulloch, "Predicting the Temperature and Flow Distribution in a Direct Oil-Cooled Electrical Machine With Segmented Stator," IEEE Transactions on Industrial Electronics, vol. 63, pp. 82-91, 2016.

[CAO12] Cao, W., Mecrow, B. C., Atkinson, G. J., Bennett, J. W., & Atkinson, D. J. (2012). Overview of electric motor technologies used for more electric aircraft (MEA). *IEEE Transactions on Industrial Electronics*, *59*(9), 3523–3531. https://doi.org/10.1109/TIE.2011.2165453.

[CHEN17] X. Chen and J. Wang, "Magnetomotive force harmonic reduction techniques for fractional-slot non-overlapping winding configurations in permanent-magnet synchronous machines," in Chinese Journal of Electrical Engineering, vol. 3, no. 2, pp. 102-113, September 2017, doi: 10.23919/CJEE.2017.8048416.

[CHE20] X. Chen, J. Wang, A. Griffo and A. Spagnolo, "Thermal Modeling of Hollow Conductors for Direct Cooling of Electrical Machines," in IEEE Transactions on Industrial Electronics, vol. 67, no. 2, pp. 895-905, Feb. 2020, doi: 10.1109/TIE.2019.2899542.

[CIS10a] M. V. Cistelecan, F. J. T. E. Ferreira, and M. Popescu, "Three phase tooth-concentrated multiple-layer fractional windings with low space harmonic content," in IEEE Energy Conversion Congress and Exposition, pp. 1399-1405, 2010.

[CIS10b] M. V. Cistelecan, F. J. T. E. Ferreira, and M. Popescu, "Three phase tooth-concentrated interspersed windings with low space harmonic content," in The XIX International Conference on Electrical Machines - ICEM 2010, pp. 1-6, 2010.

[DEE23] Deepak, K.; Frikha, M.A.; Benômar, Y.; El Baghdadi, M.; Hegazy, O. In-Wheel Motor Drive Systems for Electric Vehicles: State of the Art, Challenges, and Future Trends. *Energies* **2023**, *16*, 3121. https://doi.org/10.3390/en16073121

[DIN12] B. M. Dinh and U. Schaefer, “Core losses measurement technique for high frequency and flux density of switched reluctance machines,” in Proc. Int. Conf. Electr. Mach. (ICEM), Marseille, France, Sep. 2012, pp. 1619–1624.

[FOR20] Forrest S.J, ‘GC2.2: Manufacturing High Performance Coils with Ultimate Control’, FEMM Hub 2020 Annual Report, The University of Sheffield, 2020.

[FOR23] Forrest S.J, ‘GC2.2: Manufacturing High Performance Coils with Ultimate Control’, FEMM Hub 2020 Annual Report, The University of Sheffield, 2020.

[GEE24] Geelen, S. G. J., Curti, M., & Lomonova, E. A. (2024), “Magnetic and Thermal Modelling of Hollow Conductors for Improved Cooling and Force Density of Coreless Linear Motors”. In 2024 IEEE International Magnetic Conference - Short papers (INTERMAG Short papers) (pp. 1-2). Article 10577070 Institute of Electrical andElectronics Engineers. https://doi.org/10.1109/INTERMAGShortPapers61879.2024.10577070

[GOL19] Golovanov, D., Gerada, D., Papini, L., Xu, Z., & Gerada, C. (2019). A Holistic Electrical Machine Design Tool for More-Electric and Hybrid-Electric Aircraft. 2018 IEEE International Conference on Electrical Systems for Aircraft, Railway, Ship Propulsion and Road Vehicles and International Transportation Electrification Conference, ESARS-ITEC 2018, February 2019. https://doi.org/10.1109/ESARS-ITEC.2018.8607715.

[IEC19] IEC 60034-1:2017 Rotating electrical machines - Part 1: Rating and performance, published 2019.

[JEW21] Jewell G.W, “Introduction to Electrical Machines”,FEMM Hub short course notes, The University of Sheffield, 2021.

[JEW22] Jewell G.W, “AC losses in conductors”, FEMM Hub short course notes, The University of Sheffield, 2022.

[KRI91] R. Krishnan and A. S. Bharadwaj, “A comparative study of various motor drive systems for aircraft applications,” in Conf. Rec. IEEE IAS Annu. Meeting,1991,vol. 1, pp.252–258.

[LEV30] Levasseur A. Nouvelles formules, valables à toutes les fréquences, pour le calcul. Journal de Physique et le Radium, 1930.

[LIN13] P. M. Lindh, J. J. Pyrhonen, P. Ponomarev, and D. Vinnikov, “Influence of wedge material on losses of a traction motor with tooth-coil windings,” IECON Proc. (Industrial Electron. Conf., pp. 2941–2946, 2013, doi: 10.1109/IECON.2013.6699598.

[LIN16] P. M. Lindh et al., "Direct Liquid Cooling in Low-Power Electrical Machines: Proof-of-Concept," in IEEE Transactions on Energy Conversion, vol. 31, no. 4, pp. 1257-1266, Dec. 2016, doi: 10.1109/TEC.2016.2597059.

[LIN17] P. Lindh, I. Petrov, A. Jaatinen-Värri, A. Grönman, M. Martinez-Iturralde, M. Satrústegui, et al., "Direct Liquid Cooling Method Verified With an Axial-Flux Permanent-Magnet Traction Machine Prototype," IEEE Transactions on Industrial Electronics, vol. 64, pp. 6086-6095, 2017.

[MAD19] Madonna, V., Walker, A., Giangrande, P., Serra, G., Gerada, C., & Galea, M. (2019). Improved thermal management and analysis for stator end-windings of electrical machines. *IEEE Transactions on Industrial Electronics*, *66*(7), 5057–5069.

[MEL14] P. Mellor, R. Wrobel and N. Simpson, "AC losses in high frequency electrical machine windings formed from large section conductors," 2014 IEEE Energy Conversion Congress and Exposition (ECCE), Pittsburgh, PA, USA, 2014, pp. 5563-5570, doi: 10.1109/ECCE.2014.6954163.

[MOG14] R. R. Moghaddam, "High speed operation of electrical machines, a review on technology, benefits and challenges," *2014 IEEE Energy Conversion Congress and Exposition (ECCE)*, Pittsburgh, PA, 2014, pp. 5539-5546, doi: 10.1109/ECCE.2014.6954160.

[NAK90] K. Nakamura and Y. Hayashi, "Motor Cooling System," US Patent US4959570A, 1990.

[PAD22] D. K. K. Padinharu, G. J. Li, Z. Q. Zhu, R. Clark, A. Thomas and Z. Azar, "AC Losses in Form-Wound Coils of Surface Mounted Permanent Magnet Vernier Machines," in *IEEE Transactions on Magnetics*, vol. 58, no. 6, pp. 1-15, June 2022, Art no. 8105315, doi: 10.1109/TMAG.2022.3170658.

[PAT24] Paterson, L.; Miscandlon, J.; Butler, D. The Juxtaposition of Our Future Electrification Solutions: A View into the Unsustainable Life Cycle of the Permanent Magnet Electrical Machine. Sustainability 2024, 16, 2681. https://doi.org/10.3390/su16072681

[POP13] Popescu, M., & Dorrell, D. G. (2013). Proximity losses in the windings of high speed brushless permanent magnet AC motors with single tooth windings and parallel paths. IEEE Transactions on Magnetics, 49(7), 3913–3916. https://doi.org/10.1109/TMAG.2013.2247382.

[REF13a] A.M. El-Refaie, “Motors/Generators for traction/propulsion applications: A review,” IEEE Trans. Veh. Appl., vol. 8, no. 1, pp. 90–99, Jan. 2013.

[REF13b] A. M. El-Refaie, "Motors/generators for traction/propulsion applications: A review," in IEEE Vehicular Technology Magazine, vol. 8, no. 1, pp. 90-99, March 2013, doi: 10.1109/MVT.2012.2218438.

[SHA23] P. Shams Ghahfarokhi, A. Podgornovs, A. Kallaste, A. J. Marques Cardoso, A. Belahcen and T. Vaimann, "The Oil Spray Cooling System of Automotive Traction Motors: The State of the Art," in IEEE Transactions on Transportation Electrification, vol. 9, no. 1, pp. 428-451, March 2023, doi: 10.1109/TTE.2022.3189596.

[SIE16] SiemensAG, Munich,Germany, “World record electric motor for aircraft,” Jul 2016

[THO09] A. S. Thomas, Z. Q. Zhu and G. W. Jewell, "Proximity Loss Study In High Speed Flux-Switching Permanent Magnet Machine," in IEEE Transactions on Magnetics, vol. 45, no. 10, pp. 4748-4751, Oct. 2009, doi: 10.1109/TMAG.2009.2021666.

[USE17a] U.S. Energy Information Administration, U.S. Gulf Coast Kerosene-Type Jet Fuel Spot Price FOB (2017). URL https://www.eia.gov/petroleum/.

[USE17b] U.S. Energy Information Administration, Wholesale Electricity and Natural Gas Market Data (2017). URL https://www.eia.gov/electricity/wholesale/.

[VAC25] “RARE EARTH PERMANENT MAGNETS - VACOdym • VACOmax”, Vacuumschmelze Product Brochure.

[VEG21] Veg, L.; Kaska, J.; Skalický, M.; Pechánek, R. A Complex Study of Stator Tooth-Coil Winding Thermal Models for PM Synchronous Motors Used in Electric Vehicle Applications. Energies 2021, 14, 2395.

[WEN06] Z. Wen, L. Ruan and G. Gu, "Optimum Design of Hollow Conductor in Stator Winding for Large Evaporative Hydro-generator," 2006, CES/IEEE 5th International Power Electronics and Motion Control Conference, Shanghai, 2006, pp. 1-4, doi: 10.1109/IPEMC.2006.4777971.

[ZHA16] X. Zhang and K. S. Haran, "High-specific-power electric machines for electrified transportation applications-technology options," 2016 IEEE Energy Conversion Congress and Exposition (ECCE), Milwaukee, WI, 2016, pp. 1-8, doi: 10.1109/ECCE.2016.7855164.

[ZHA19] Y. Zhao, D. Li, T. Pei, and R. Qu, “Overview of the rectangular wire windings AC electrical machine,” CES Trans. Electr. Mach. Syst., vol. 3, no. 2, pp. 160–169, 2019, doi: 10.30941/cestems.2019.00022.

[ZUE25] ‘PEEK Insulated Wire’, Product datasheet, Zeus Inc. (https://www.zeusinc.com/)